Characterization of thermoregulatory mechanisms in kinases involved in splicing control

Inaugural-Dissertation

to obtain the academic degree

Doctor rerum naturalium (Dr. rer. nat.)

submitted to the Department of Biology, Chemistry, Pharmacy

of Freie Universität Berlin

by

Benjamin Dimos-Röhl

2024

This work was carried out in the period of April 2020 to June 2024 under the supervision of Prof. Dr. Florian Heyd at the Institute of Chemistry and Biochemistry, Freie Universität Berlin, Germany.

First Reviewer:	Prof. Dr. Florian Heyd RNA Biochemistry Institute of Chemistry and Biochemistry Freie Universität Berlin Takustraße 6 14195 Berlin, Germany
Second Reviewer:	Dr. Bernhard Loll Structural Biochemistry Institute of Chemistry and Biochemistry Freie Universität Berlin Takustraße 6 14195 Berlin, Germany
Date of defense:	08.10.2024

Acknowledgements

First, I want to thank Prof. Dr. Florian Heyd for giving me the opportunity to work on these interesting projects, for supervising and guiding my work, for supporting me and giving me the room to grow as a scientist.

I would also like to thank Dr. Bernhard Loll for being my second reviewer, but even more so for his supervision, support and teachings in structural biology and occasional after work beers coupled with fruitful conversations.

I want to thank our cooperation partners Dr. Daniel Maag, Dr. Rainer Merkl and Dr. Kristina Straub for great collaborations. Thank you to Dr. Benno Kuropka for the support with everything mass spectrometry related.

I would like to thank past and present AG Heyd members for their comradeship, stimulating and funny conversations, shared afterwork beers and in general creating a wonderful work atmosphere. I thank Dr. Tom Haltenhof, Dr. Stefan Meinke, Dr. Felix Ostwaldt and Carl Helmer for evening meetings that made Covid times a lot more bearable. Thank you Antje Grünwald and Bobby Viet Draegert for all the background work, without which this work wouldn't have been possible, and for supplying sugary treats in times of need. Special thanks go to Miriam Strauch, Paul Wulff, Alica Grindel, Dr. Ioana Weber and Frank Kuppler with whom I shared the joy of teaching future generations of scientists the basics of RNA biochemistry.

Thank you Fatali, Pancake and Pukipon for donating cat whiskers to science.

Many thanks and love go out to my parents who always supported and encouraged me to go my own way and reach as high as I can.

Last but not least I want to thank my wife Dr. Nicole Dimos for fruitful science talks on the way to work, for supporting and believing in me, for dealing with my scatter-brained self in stressful times and in general always being there for me. And my biggest thanks for giving us our son, who brings a smile to my face even after long work days.

Declaration of authorship

I, Benjamin Dimos-Röhl, hereby declare that I alone am responsible for the content of my doctoral dissertation and that I have only used the sources or references cited in the dissertation. I declare that I have not submitted my doctoral dissertation in a different doctorate procedure before.

Berlin, 14.06.2024 _____

Table of contents

Abstract

Alternative splicing of pre-mRNAs can regulate the expression and function of proteins. As such it is a major tool of eukaryotes to adapt their proteome – and thus the whole organism – to external and internal changes of circumstances. In mammals body temperature cycles result in oscillating alternative splicing driven by rhythmic phosphorylation of SR-proteins. Recently, it has been shown that this is facilitated by temperature dependent activity of Cdc2-like kinases (CLKs). Temperature sensitivity is conserved across evolution and the active temperature range of the kinases is adapted to the body temperature or growth temperature of the corresponding organism. While it has been shown that the temperature dependence of CLK activity is mediated by conformational changes in the activation segment, the mechanisms by which the active temperature range of the kinases is adapted to the organisms body temperature remained elusive. Here we show multiple structural features fine-tuning the active temperature range of CLK homologues. We characterized a CLK homologue, CmLIK, and its substrate phosphorylation from the ancient thermophilic red alga *C. merolae* and could show that kinase activity at high temperatures is mediated by activation segment stabilization via a salt bridge in the P+1 loop. In contrast to other CLK homologues auto phosphorylation of CmLIK shows markedly different patterns than substrate phosphorylation. Furthermore, we identified an H-bond network from a residue in the P+1 loop of a CLK homologue from *A. thaliana*, AtAFC3, that stabilizes the activation segment and also mediates kinase activity at higher temperatures. We could show that AFCs play a role in heat responsive hypocotyl elongation in *A. thaliana* upstream of PIF4, the major regulator of thermomorphogenesis. Our results demonstrate stabilization of the P+1 loop of the activation segment as a common mechanism mediating CLK homologue activity at high temperatures. With the characterization of CmLIK we found a model system to study an ancient CLK homologue with activity at high temperatures. Our findings lay the foundation for exploration of genetic engineering of crop plant AFCs to facilitate kinase activity at higher temperatures and adapting their thermomorphogenesis accordingly. This could lead to a partial solution of the problems crop plant growth faces due to global warming.

Zusammenfassung

Durch alternatives Spleißen von Prä-mRNAs kann die Expression und Funktion von Proteinen reguliert werden. Deshalb ist es ein wichtiges Werkzeug für Eukaryoten, um ihr Proteom – und damit den gesamten Organismus – an äußere und innere Veränderungen anzupassen. Bei Säugetieren führt der zyklische Verlauf der Körpertemperatur zu oszillierendem alternativem Spleißen, das durch die rhythmische Phosphorylierung von SR-Proteinen angetrieben wird. Kürzlich wurde gezeigt, dass dies durch die temperaturabhängige Aktivität von Cdc2-ähnlichen Kinasen (CLKs) kontrolliert wird. Die Temperaturempfindlichkeit der Kinasen ist evolutionär konserviert und der aktive Temperaturbereich ist an die Körpertemperatur bzw. Wachstumstemperatur des entsprechenden Organismus angepasst. Es konnte gezeigt werden, dass die Temperaturabhängigkeit der CLK-Aktivität durch Konformationsänderungen im Aktivierungssegment vermittelt wird, aber die Mechanismen, durch die der aktive Temperaturbereich der Kinasen an die Körpertemperatur des Organismus angepasst wird, blieben unklar. Hier zeigen wir mehrere Strukturmerkmale, die den aktiven Temperaturbereich von CLK-Homologen anpassen. Wir haben ein CLK-Homolog, CmLIK, aus der thermophilen Rotalge *C. merolae* und dessen Substratphosphorylierung charakterisiert. Dabei konnten wir zeigen, dass die Kinaseaktivität bei hohen Temperaturen durch die Stabilisierung des Aktivierungssegments über eine Salzbrücke im *P+1-loop* vermittelt wird. Im Gegensatz zu anderen CLK-Homologen folgt die Autophosphorylierung von CmLIK nicht demselben Muster wie die Substratphosphorylierung. Darüber hinaus haben wir ein Wasserstoffbrückennetzwerk um einen Rest im P+1-*loop* eines CLK-Homologs aus *A. thaliana*, AtAFC3, identifiziert. Dieses stabilisiert das Aktivierungssegment und vermittelt ebenfalls die Kinaseaktivität bei höheren Temperaturen. Wir konnten zeigen, dass AFCs über PIF4, dem Hauptregulator der Thermomorphogenese, eine Rolle bei der wärmeresponsiven Hypokotyl Verlängerung in *A. thaliana* spielen. Unsere Ergebnisse zeigen die Stabilisierung des *P+1-loops* des Aktivierungssegments als einen allgemeinen Mechanismus, der die Aktivität von CLK-Homologen bei hohen Temperaturen vermittelt. Mit der Charakterisierung von CmLIK haben wir ein Modellsystem gefunden, um ein CLK-

Homolog mit Aktivität bei hohen Temperaturen zu untersuchen. Unsere Ergebnisse legen den Grundstein für die Erforschung der genetischen Modifizierung von AFCs in Nutzpflanzen, um die Kinaseaktivität bei höheren Temperaturen zu ermöglichen und ihre Thermomorphogenese entsprechend anzupassen. Dies könnte zu einer teilweisen Lösung der Probleme beim Anbau von Nutzpflanzen aufgrund der globalen Erwärmung führen.

1 Introduction

1.1 Alternative splicing – a driver of complexity

According to the original dogma of life DNA is transcribed into messenger RNA (mRNA) which in turn gets translated into a protein. While this is true in general, reality is much more complex. Looking at this process in more detail, DNA is transcribed into precursor mRNA (pre-mRNA) which consists of exons – coding sequences – and introns – non-coding sequences. This pre-mRNA is processed co- and post-transcriptionally in various ways, such as 5' capping (Shatkin, 1976), polyadenylation (Colgan and Manley, 1997), A-to-I editing (Nishikura, 2016) and splicing, until it is mature mRNA which gets translated into a polypeptide sequence. These modifications influence the stability, localization and included information of the mRNA and thus serve as regulatory mechanisms.

Splicing describes the excision of introns from the pre-mRNA and joining of the remaining exons via two transesterification reactions (Figure 1-1 A) (Black, 2003). Sequence elements required for this are the 5' splice site, 3' splice site (Yeo and Burge, 2004), the intronic branch point adenosine (Gao et al., 2008) and the poly pyrimidine tract upstream of the 3' splice site (García-Blanco et al., 1989) (Figure 1-1 B). This process is catalyzed by the spliceosome, a highly dynamic complex comprising mainly five small nuclear ribonucleoprotein particles (snRNPs; U1, U2, U4, U5 and U6) and a plethora of auxiliary proteins which assembles anew for every splicing event at the 5' and 3' splice site in a stepwise manner (Wahl et al., 2009).

While human exons exhibit a median length of 120 nucleotides (nt) in a range of 50-250 nt (Movassat et al., 2019), the median size of introns is 3.4 kilobases (kb) (Lander et al., 2001). Considering the huge excess of non-coding sequence over coding sequence, this would appear as more junk than information if it was a static process. But splicing is not always constitutive. Alternative splicing describes the possibility to generate multiple different mature mRNAs from one pre-mRNA by inclusion of different exons, or also introns, in the mature transcript. As such it is a means for proteome diversification since multiple different proteins can originate from one gene (Graveley, 2001).

In general, there are five forms of alternative splicing (Figure 1-1 C) (Black, 2003). The most common in humans being the cassette exon (Wang et al., 2008), where an alternative exon that is either included or excluded is located between two constitutive exons, which are always included in the mature transcript. Similar are mutually exclusive exons, where two alternative exons are located next to each other but only one of both can be included in the mature transcript at a time. Alternative 5' and 3' splice sites enable the generation of shorter or longer exons. These splicing isoforms can give rise to longer or shorter protein isoforms with different functions or interactions, if the reading frame remains conserved. But, they can also serve as a regulatory mechanism via inclusion of a premature termination codon or causation of a frame shift and targeting the transcript for degradation, for example via nonsense-mediated mRNA decay (NMD). In addition, intron retention describes the inclusion of an intron in the mature transcript. These retained introns are much shorter than other introns and often serve a regulatory function, as described before. While intron retention is not common in humans, it's a very relevant form of alternative splicing in plants (Ner-Gaon et al., 2004).

Notably 95 % of all human genes are spliced alternatively (Pan et al., 2008), which explains a large proteome in relation to a rather small genome. The impact of proteome and protein-protein interaction diversification via alternative splicing (Buljan et al., 2012) on organism complexity is evident in the comparison of the amount of alternative splicing in simple organisms such as nematodes and more complex organisms as mice or humans, where more alternative splicing correlates with higher complexity (Barbosa-Morais et al., 2012). Moreover, throughout different species, it could be observed, that alternative splicing is also tissue specific. Consistently alternative splicing abundance was higher in cortex, cerebellum and testis than in liver, kidney and heart (Barbosa-Morais et al., 2012).

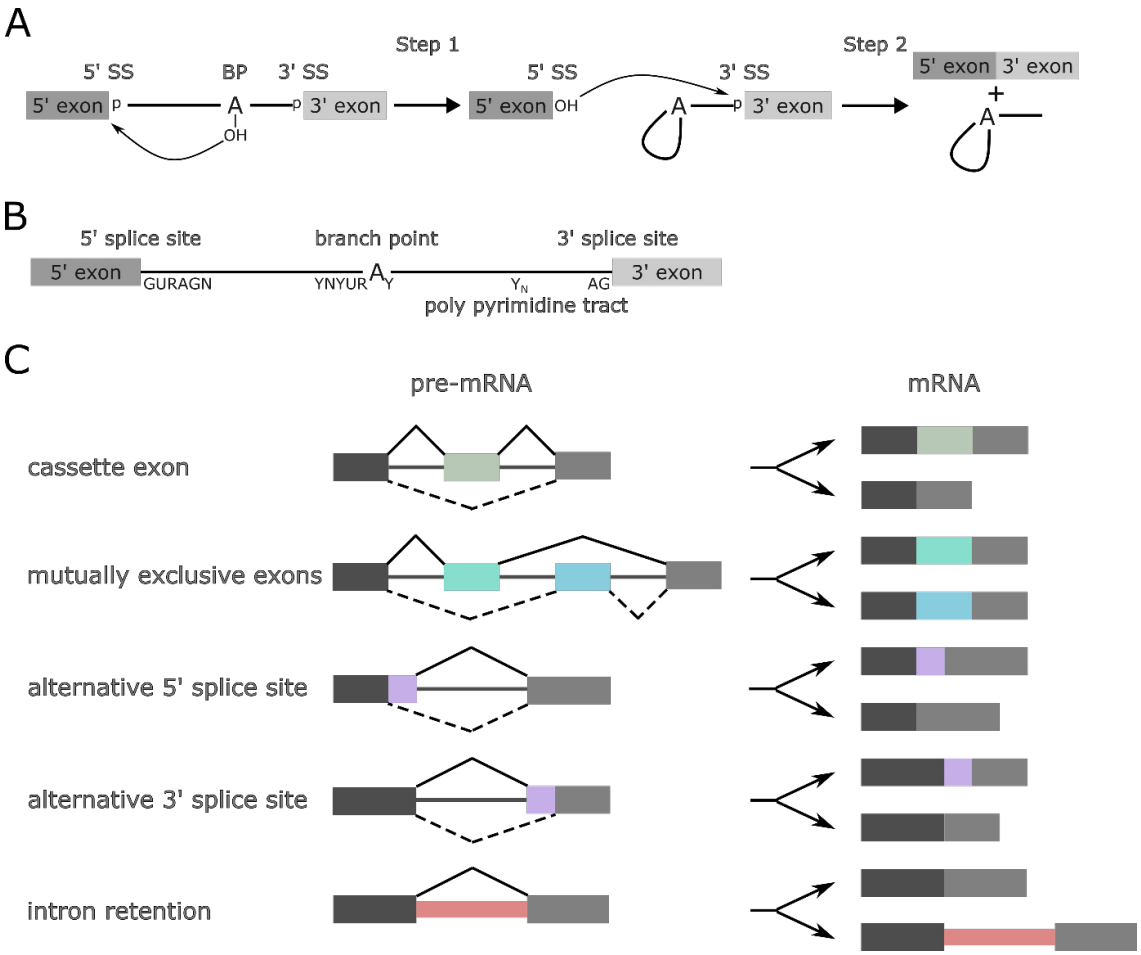

Figure 1-1 Schematics of alternative splicing. A Simplified scheme of the two transesterification reactions constituting a splicing event. In the first step the 3'OH group of the branchpoint (BP) adenine attacks the phosphodiester bond (p) of the 5' splice site (5' SS). In the second step the free 2'OH group of the 5' exon attacks the phosphodiester bond of the 3' splice site (3' SS). The exons are ligated and the intron is excised in a lariat form. Adapted from (Plaschka et al., 2019). **B** Conserved elements necessary for splicing are the 5' splice site, 3' splice site, branch point adenine and poly pyrimidine tract. Human consensus sequences are indicated below the line depicting the intron. Adapted from (Plaschka et al., 2019). **C** Scheme of the five major forms of alternative splicing. Exons are depicted as rectangles and introns as grey lines. Splice events are shown as solid or alternatively as dashed black lines. The alternatively included sequences are indicated by color. Each pre-mRNA can generate two mRNAs. Adapted from (Black, 2003).

1.2 Regulation of alternative splicing – a matter of context

A process as impactful as alternative splicing needs tight regulation to function properly and exert its full potential. The main players in alternative splicing regulation are cis-acting elements, sequences in the pre-mRNA, and trans-acting factors, proteins that recognize and bind these sequences (Fu and Ares, 2014). Cis-acting elements can be classified as intronic or exonic, dependent on their location and divided into splicing

silencers or enhancers. If a splicing silencer is bound by the corresponding trans-acting factor, a repressor protein, assembly of the splicing machinery is blocked and the transcript remains unspliced, meaning the introns and exons remain in the transcript. In contrast, if a splicing enhancer is bound by its trans-acting factor, an activator protein, it aids in assembly of the splicing machinery and the transcript gets spliced, the introns excised. The function of these regulatory sequences and proteins in general always needs to be considered in the context of their position in the transcript and the splice event that is investigated (Ule and Blencowe, 2019). A regulatory pair might function as enhancers for one splice site but at the same time as silencers for another site in the same transcript in the complex process of alternative splicing. While this means that the role of a trans-acting factor can't be predicted with certainty and is always context dependent, heterogeneous nuclear ribonucleoproteins (hnRNPs) are in general regarded as repressors and SR-proteins as activators (Mayeda and Krainer, 1992; Matlin et al., 2005). The position dependent effect also applies to trans-acting factors that belong to other families (Ule et al., 2006; Wang et al., 2010). Other factors that influence splice site selection are for example competition for splicing machinery subunits between different splice sites (Yang and Li, 2008), RNA secondary structure (Eperon et al., 1988; Hiller et al., 2007) and the velocity of RNA polymerase II (Pol II) (La Mata et al., 2003).

Via these regulatory mechanisms alternative splicing and thus the cellular transcriptome and proteome can be adapted in response to different circumstances. Prominent examples of changes in alternative splicing upon environmental stimuli and resulting effects can be found in the activation of T-cells upon stimulation via antigens (Martinez and Lynch, 2013). For example, alternative splicing of the CD45 transcript upon T-cell activation leads to a shorter, inactive isoform of CD45 and thus to reduced signaling via the T-cell receptor. Here alternative splicing functions as a feedback loop to regulate T-cell activity (Wang et al., 2001; Xu and Weiss, 2002). Furthermore, alternative splicing also plays a role in cell differentiation. For example it could be shown that a change in splice isoform of Ninein under control of Rbfox facilitates differentiation of neural progenitor cells into neurons (Zhang et al., 2016). Dysregulation of alternative splicing can result in various diseases, notably also cancer (David and Manley, 2010).

1.3 SR-proteins – major splicing activators

In humans the SR-protein family of splicing factors comprises 12 core members, SRSF1-12 (Manley and Krainer, 2010). They in general consist of one or two N-terminal RNA-binding domains (RBDs) and a C-terminal arginine-serine rich (RS) domain (Fu and Maniatis, 1992; Zahler et al., 1992). Classification as SR-protein does not only depend on structural similarity, but also on the protein functioning in constitutive and alternative splicing (Long and Caceres, 2009). RS domains were also found in other proteins, which either lack the RBDs or execute other functions (Boucher et al., 2001). While SR-proteins are also characterized by their function in splicing, their functionality goes beyond that as also roles in chromatin interactions (Loomis et al., 2009), transcriptional elongation via Pol II modulation (Lin et al., 2008), NMD regulation (Zhang and Krainer, 2004), mRNA export (Huang and Steitz, 2005) and translation stimulation in the cytosol (Sanford et al., 2004; Michlewski et al., 2008) have been reported.

For their regulating function in splicing multiple modes have been characterized. After binding a pre-mRNA splicing enhancer sequence with their RBD SR-proteins can interact with U1 snRNPs bound at the 5' splice site and U2AF bound at the 3' splice site of the same exon via their phosphorylated RS domain and thus aid in exon definition (Kohtz et al., 1994). But SR-proteins can also form a protein-protein interaction network bridging an intron from 5' splice site to 3' splice site in an RS domain dependent way and thus facilitate spliceosome assembly (Wu and Maniatis, 1993). In another mode, an SR-protein that has bound an exonic splicing enhancer (ESE) can inhibit the effect of an hnRNP bound to an exonic splicing silencer (ESS) on the same exon and thus promote splicing of this exon (Zhu et al., 2001). Interestingly it has been shown that the RS domain can also interact with the branchpoint to facilitate spliceosome assembly (Shen et al., 2004).

It has been shown that SR-proteins are essential for organism development (Jumaa et al., 1999; Ding et al., 2004) and cell differentiation (Wang et al., 2001; Sen et al., 2013). Furthermore their dysregulation is associated with a plethora of cancers (Stickeler et al., 1999; Karni et al., 2007; Jia et al., 2010; Gautrey and Tyson-Capper, 2012; Cohen-Eliav et al., 2013; Tang et al., 2013). Especially mutations in SRSF2 have been linked to leukemia (Yoshida et al., 2011; Lasho et al., 2012; Meggendorfer et al., 2012; Patnaik et al., 2013).

Thus, it is necessary that SR-protein activity is tightly regulated. Post translational modifications (PTMs) are an elegant way to modulate protein activity. For SR-proteins three major PTMs have been reported. Lysine acetylation marks SR-proteins for proteasomal degradation and deacetylation in turn counteracts this, leading to modulated protein homeostasis (Edmond et al., 2011). Arginine methylation has been shown to control subcellular localization of SR-proteins and thus influence their site of action (Sinha et al., 2010). The most well characterized SR-protein PTM is serine phosphorylation in their RS domain. A tightly regulated cycle of phosphorylation and dephosphorylation is necessary for correct SR-protein functions in splicing (Mermoud et al., 1994; Cao et al., 1997). While phosphorylation is crucial for interaction with other splicing factors and spliceosomal components (Xiao and Manley, 1997), dephosphorylation is essential for the continuation of the splicing process after spliceosome assembly (Tazi et al., 1993). In addition to activity modulation, phosphorylation has also been shown to regulate SR-protein shuttling between cytosol and nucleus. While phosphorylated SR-proteins translocate to the nucleus (Yun et al., 2003) and accumulate in nuclear speckles (Saitoh et al., 2004), dephosphorylated SR-proteins get exported from the nucleus together with spliced mRNA (Huang et al., 2004; Reed and Cheng, 2005; Singh et al., 2012). The importance of SR-protein activity regulation via phosphorylation is highlighted as the responsible kinases are required for organism development across species (Kuroyanagi et al., 2000; Loh et al., 2012) and their dysregulation is – same as for SR-proteins – associated with cancer development (García-Sacristán et al., 2005; Hayes et al., 2007; Jang et al., 2008; Gout et al., 2012).

SR-protein phosphorylation is mainly facilitated by two kinase families. The SR-protein specific kinase (SRPK) family comprises the first characterized kinases responsible for SR-protein phosphorylation (Gui et al., 1994a; Gui et al., 1994b) and is conserved throughout all eukaryotes (Giannakouros et al., 2011). While SRPKs are located in the cytosol and nucleus, with cytosolic localization facilitated by a large spacer in the C-lobe (Ding et al., 2006), the second family responsible for SR-protein phosphorylation, the Cdc2-like kinase (CLK) family (Colwill et al., 1996a), is localized solely in the nucleus and lacks this spacer (Colwill et al., 1996b; Duncan et al., 1998). The difference in localization suggests a synergistic relationship with distinct roles for both kinase families (Ngo et al., 2005). While SRPKs are responsible for initial phosphorylation and nuclear import of SR-

proteins, CLKs are responsible for further phosphorylation (Velazquez-Dones et al., 2005) and distribution of SR-proteins from nuclear speckles (Cáceres et al., 1997; Nayler et al., 1997).

1.4 CLKs – dual-specificity kinases controlling alternative splicing

Similar to the SRPK family, the CLK family is conserved throughout eukaryotes, too (Yun et al., 1994). Both families belong to the CMGC (cyclin-dependent kinase (CDK), mitogen-activated protein kinase (MAPK), glycogen synthase kinase (GSK3), CLK) kinase group (Manning et al., 2002; Varjosalo et al., 2013). CDKs and MAPKs constitute the two largest families of this group. The closest families to CLKs in this group are dual-specificity tyrosine-regulated kinases (DYRK) and SRPKs (Figure 1-2 A) (Howard et al., 2014). In humans there are 4 CLK homologues, CLK1-4. Due to a conserved "EHLAMMERILG" motif in the C-lobe CLKs are also referred to as LAMMER-kinases. Notably CLKs are dual-specificity kinases, which are able to auto phosphorylate on tyrosine, serine and threonine residues, but only phosphorylate substrates at the latter two amino acids (Nayler et al., 1997). CLKs are constitutively active, their activity does not depend on phosphorylation of its activation loop (Bullock et al., 2009). Consistent with that, the arginine in the catalytic loop that is present in all kinases with activation loop phosphorylation dependent activity (Johnson et al., 1996) is replaced by a threonine, constituting an HTD motif. But it could be shown that CLK auto phosphorylation modulates substrate phosphorylation and recognition in a substrate specific manner (Prasad and Manley, 2003). While SRSF1 phosphorylation appeared to be dependent on Ser/Thr auto phosphorylation, SRSF2 phosphorylation appeared to be dependent on Tyr auto phosphorylation.

CLKs comprise a variable unstructured N-terminus and a typical kinase domain (Colwill et al., 1996b). The kinase domain (KD) can be subdivided into the N-lobe, adopting mostly β-sheet folds and harboring the αC helix, and the C-lobe, which is mostly α-helical and contains the catalytic center. Distinct structure features in the KD that set CLKs apart from other kinases are a β-hairpin insertion, the αG helix harboring the LAMMER motif, a MAPK-like insertion and the αH helix (Figure 1-2 B). The LAMMER motif has been suggested to influence substrate binding (Kang et al., 2010). While in SRPKs the MAPK-

like insertion forms a binding groove that is essential for its processive activity (Ngo et al., 2008; Long et al., 2019), this binding groove is buried by the αH helix in CLKs (Bullock et al., 2009). The αH helix also buries the αG helix, potentially further interfering with specific substrate interaction. In addition, the β-hairpin covers substrate interaction grooves available in related MAPKs (Bullock et al., 2009). The differences in substrate interactions between SRPKs and CLKs mediated by these structural elements might explain the difference in substrate specificity of both kinase families. While SRPKs strictly prefer Ser-Arg sites, CLKs phosphorylate Ser-Arg, Ser-Lys and Ser-Pro sites (Colwill et al., 1996a). A feature that is present in all protein kinases is the activation segment, a largely unstructured stretch of 20 to 35 residues in close proximity of the catalytic loop that comprises the magnesium binding loop, β-sheet 9, the activation loop and the P+1 loop. Conformational changes and phosphorylation in the activation segment have been shown to influence kinase activity (Nolen et al., 2004). The sequence of the 25 residues constituting the CLK activation segment is highly conserved between all homologues and vertebrate species (Figure 1-2 C). Re-evaluation of a previously published electron density of a hCLK1 crystal (PDB: 2VAG (Fedorov et al., 2011)) revealed an alternative conformation of the activation segment. The unphosphorylated conformation was oriented closer to the catalytic loop in contrast to the conformation phosphorylated at S341 and T342, which is shifted further away from the catalytic loop (PDB: 6TW2 (Haltenhof et al., 2020), see also Figure 1-3 B). Superimposition with a PKA substrate (PDB: 1JBP (Madhusudan et al., 1994)) revealed a steric clash between the substrate and R342 of the phosphorylated but not of the unphosphorylated conformation suggesting the phosphorylated conformation to be inactive.

While CLK KDs are relatively conserved, their N-termini differ in length and amino acid sequence between homologues. The intrinsically disordered N-terminus harbors an RS domain and has been shown to be essential for interaction with substrate SR proteins (Colwill et al., 1996b). Substrate specificity via self-oligomerization and CLK localization to nuclear speckles are also governed by the N-terminus (Keshwani et al., 2015). Furthermore, this RS domain is important for substrate release of CLKs in a SRPK-dependent way. CLK1 alone is unable to release its phosphorylated substrate, but interaction with SRPK1 via its RS domain leads to substrate release (Aubol et al., 2016; Aubol et al., 2018). This is another example for the intimate relationship between CLKs

and SRPKs in SR-protein regulation. While multiple nuclear localization sequences (NLS) can be found in the CLK N-termini, they appear to be not essential for the nuclear localization of CLKs. Instead, CLKs are co-transported with their SR-protein substrates by forming a stable complex via their N-terminus and utilizing the SR-protein NLS (George et al., 2019).

CLK phosphorylation, and thus activity and SR-Protein phosphorylation, can be modulated via extracellular signals. One characterized way is CLK phosphorylation by Akt2 downstream of phosphatidylinositol 3-kinase (PI3K) activation upon insulin stimulation which influences the alternative splicing of protein kinase C βII (PKCβII) pre-mRNA (Jiang et al., 2009). More specifically Akt2 phosphorylates CLK1 at S36, T122 and S139 in the RS domain during preadipocyte differentiation (Li et al., 2013). For CLK2 phosphorylation by Akt in the RS domain (Nam et al., 2010) as well as on T343 in the activation segment (Rodgers et al., 2010) has been shown in different contexts. It has to be noted that also SRPK activity is under control of the PI3K/Akt cascade upon epidermal growth factor (EGF) stimulation (Zhou et al., 2012), which is to be expected since both kinase families act in sync. A scheme of CLK and SRPK modulation downstream of EGFR activation is shown in Figure 1-2 D.

As for SR-proteins, dysregulated CLK expression and activity is associated with cancer development and progression (Naro and Sette, 2013; Blackie and Foley, 2022; Song et al., 2023). But CLKs have also been associated with a wide range of other diseases such as Alzheimer's disease (Glatz et al., 2006; Jain et al., 2014), Duchenne muscular dystrophy (Sako et al., 2017), osteoarthritis (Deshmukh et al., 2019), HIV-1 replication (Wong et al., 2011; Wong et al., 2013), influenza A replication (Artarini et al., 2019) and cardiac hypertrophy (Huang et al., 2022). Thus, it is not surprising that specific CLK inhibitors are sought after as potential therapeutics. Most developed CLK inhibitors are ATP mimetics binding in the ATP binding pocket between N- and C-lobe (Lee et al., 2019; Němec et al., 2019; Martín Moyano et al., 2020; Schröder et al., 2020). One inhibitor is TG003, a benzothiazole, that is specific for CLK1 and 4 (Muraki et al., 2004) and has for example been investigated for prostate cancer treatment (Uzor et al., 2021).

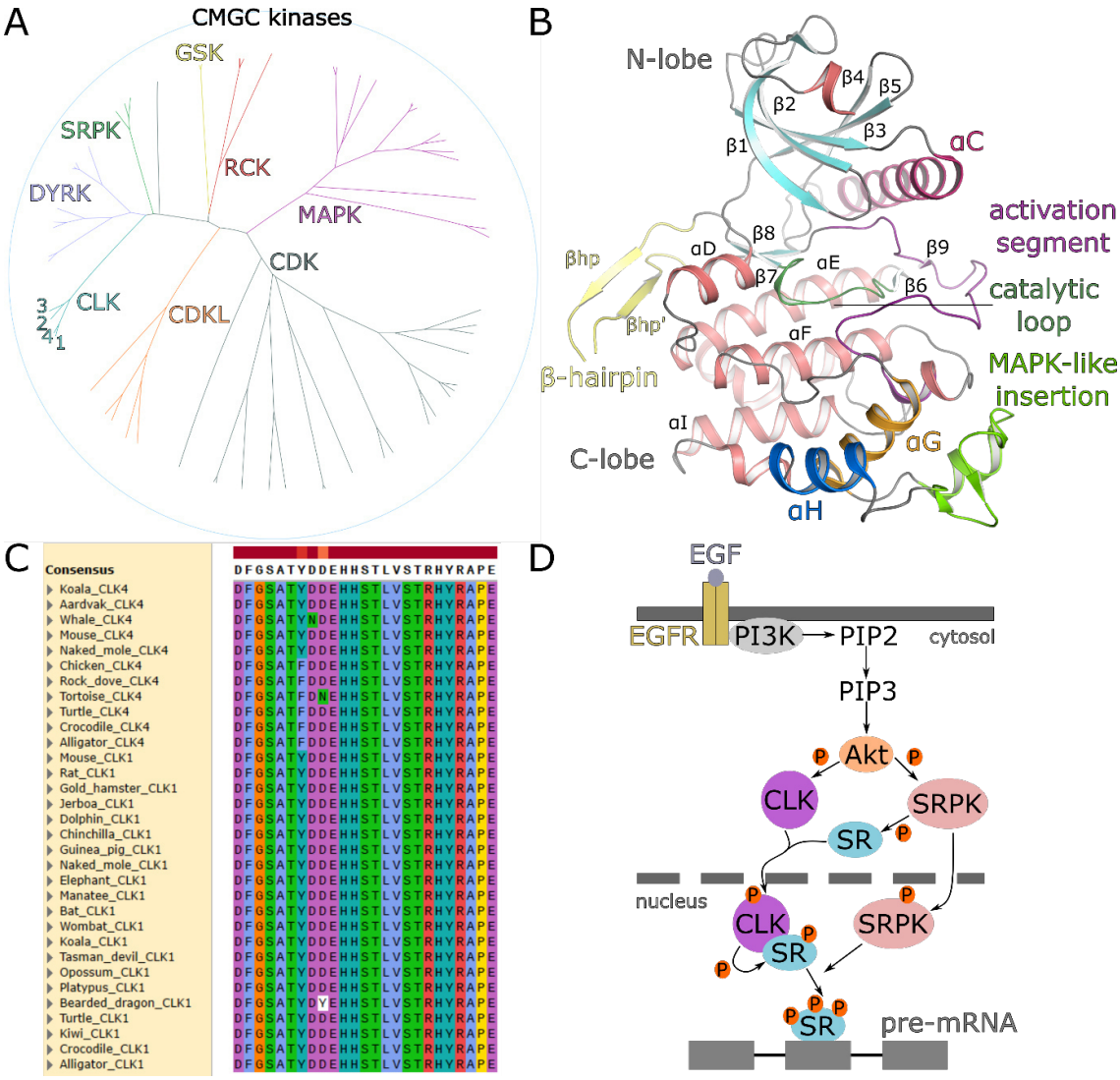

Figure 1-2 CLK phylogeny, structure and regulation. A Phylogenetic tree of the human CMGC kinase group. Family branches are indicated in corresponding colors and numbers indicate position of CLK1-4. Kinome data from (Manning et al., 2002). Tree was visualized with Hypertree v1.2.2 (Bingham and Sudarsanam, 2000). **B** Structure of hCLK1 kinase domain (PDB: 6TW2 (Haltenhof et al., 2020)) depicted as cartoon. α-helices are colored in deepsalmon and β-sheets aquamarine. Secondary structure element labeling according to (Bullock et al., 2009; Modi and Dunbrack, 2019) is indicated. Important structural elements are labeled in different colors. **C** Multiple sequence alignment of CLK1 and CLK4 activation segments of different species. Conservation as colored blocks and consensus sequence shown on top. Residues colored according to properties and conservation (Clustal X color scheme). **D** Scheme of CLK and SRPK modulation upon EGFR activation. PI3K activates Akt via PIP3. Akt phosphorylates CLKs and SRPKs. Initial SR-protein phosphorylation by SRPKs in the cytosol is followed by translocation into the nucleus in complex with CLKs. CLKs hyperphosphorylate SR-proteins. SRPKs initialize SR-protein release from CLKs and hyperphosphorylated SR-proteins regulate alternative splicing. Adapted from (Zhou and Fu, 2013).

1.5 Linking body temperature and alternative splicing

The core body temperature of homeothermic organisms is tightly regulated in a narrow range but oscillates in a circadian manner by around 1 – 4°C (Refinetti and Menaker, 1992; Buhr et al., 2010; Saini et al., 2012). Previously it could be shown that these small changes control rhythmic alternative splicing dependent on RS domain phosphorylation in SR-proteins with higher SR-protein phosphorylation at lower temperatures (Preußner et al., 2017). A previous study from the Heyd laboratory could show that CLKs are the cellular factor linking subtle changes in body temperature to alternative splicing changes (Haltenhof et al., 2020). Human CLK activity was shown to be temperature dependent in a reversible manner in the physiologically relevant temperature range. High activity was observed at lower temperatures while it decreased with increasing temperature. The kinase domain was sufficient to exhibit a very similar temperature activity profile as the full-length CLK. This temperature dependence was found to be mediated by the activation segment. More precisely, it could be pinpointed to two residues, hCLK1 R343 and H344, of which mutation abolished temperature dependent hCLK1 activity. Introduction of H344 in hSRPK1 was sufficient to induce temperature dependence to the otherwise temperature independent active kinase.

Furthermore, it could be shown in the same study (Haltenhof et al., 2020) that the CLK activity range of three poikilotherm species, *Drosophila melanogaster*, *Alligator mississippiensis* and *Trachemys scripta scripta*, is adapted to the growth temperature of the corresponding organism. Interestingly CLK activity also coincides with the temperature ranges observed for temperature dependent sex determination (TSD) (Capel, 2017) for both reptiles (Ferguson and Joanen, 1982). Together with the finding that one temperature dependent intron retention event in *Jarid2* that is associated with TSD (Deveson et al., 2017) is under control of CLK activity this suggests that CLKs are involved in reptile TSD.

Recently temperature dependent CLK activity was found to play a role in immune response. It could be shown that small changes in body temperature below fever temperature can regulate antiviral innate immunity via alternative splicing in context of SARS-CoV-2 infection (Los et al., 2022). At lower temperatures STAT2 expression is decreased via inclusion of a premature termination codon in exon 11, whereas at higher

temperatures an alternative 5' splice site in the same exon is used, which leads to exclusion of the premature termination codon and increased STAT2 expression levels. STAT2 then induces expression of diverse antiviral genes and increases the defense against viral infection. The observed effect could be diminished by the CLK-specific inhibitor TG003, linking this alternative splicing event to CLK activity.

Considering that body temperature decreases with age (Keil et al., 2015) it is of great interest for a population that grows ever older to elucidate the mechanisms by which body temperature changes alternative splicing and thus cell behavior and how detrimental processes can be counteracted. In addition to the already elucidated implications of CLK activity in temperature dependent antiviral response, it needs to be considered that CLKs are associated with a lot of diseases and that solid cancerous tissue exhibits elevated temperatures (Owens et al., 2020). This offers potential novel therapeutic treatment via temperature changes that can be improved by fully understanding temperature dependent CLK activity and how to modulate it.

1.6 *Cyanidioschyzon merolae* – low organism complexity and high temperatures

The red algae *Cyanidioschyzon merolae* (*C. merolae*) was found to inhabit sulfuric hot springs with temperatures of around 45°C and a pH of 1.5 (Luca et al., 1978). It belongs to the most ancient clades of red algaes (Yoon et al., 2004; Yoon et al., 2006) and exhibits an exceptionally simple cellular architecture, lacking a rigid cell wall and vacuoles and containing just one nucleus, one mitochondrion and one plastid (Luca et al., 1978). The *C. merolae* genome is only 16.5 Mbp small and was fully sequenced (Ohta et al., 1998; Matsuzaki et al., 2004; Nozaki et al., 2007). Only 0.5 % of its protein-coding genes contain introns and overall gene redundancy is low. Several genetic modification methods, such as transient gene expression (Ohnuma et al., 2008), homologous recombination (Minoda et al., 2004), stable overexpression (Watanabe et al., 2014) and epitope tagging using marker recycling (Takemura et al., 2018) have been established for *C. merolae*. All of the aforementioned characteristics made it an outstanding candidate as model organism for various processes, such as organelle division (Kuroiwa, 1998; McFadden and Ralph, 2003), photosystem function (Busch et al., 2010; Nikolova et al., 2017), starch

metabolism (Pancha et al., 2019; Takahashi et al., 2021), biofuel production (Pancha et al., 2021) and evolution of pre-mRNA splicing (Stark et al., 2015; Black et al., 2016; Reimer et al., 2017; Wong et al., 2023).

Considering that *C. merolae* possesses such a small genome and only 27 introns, it is not surprising that also its spliceosome is reduced in comparison to other eukaryotes (Stark et al., 2015). Along with spliceosome components, two SR-proteins have been identified. CmRSP31 (gene CYME_CMO009C), homologue to *Arabidopsis thaliana* RSP31, and CmSC35 (gene CYME_CML202C), homologue to human SRSF2. Looking for dual-specificity kinases a LAMMER-like dual-specificity kinase, CmLIK (gene CYME_CMR245C), can be found in *C. merolae*. It is classified as LAMMER-like since the αG helix comprises "EHLQLMQKLLQ" instead of the typical LAMMER motif.

A previous study from the Heyd laboratory investigated the ability of CmLIK-KD to phosphorylate a synthetic GST-RS substrate comprising a GST-tag followed by a PreScission cleavage site, short linker and four Arg-Ser dipeptide repeats (Haltenhof, 2020). They found high substrate phosphorylation between 44°C and 52°C with a maximum at 48°C (Figure 1-3 C). Auto phosphorylation was highest at 52°C. As for other CLKs the temperature activity profile matched the living temperature range. The melting temperature was determined to be 55°C via circular dichroism (CD) spectroscopy, suggesting that the decrease in activity was not due to unfolding but to conformational changes. CmLIK comprises a very long intrinsically disordered N-terminal region and a kinase domain. To get further insights they obtained a first structure of the CmLIK-KD at a resolution of 2.5 Å by X-ray crystallography (Figure 1-3 A). CmLIK-KD exhibited a typical kinase fold as for CLKs. Two major differences in structural elements are evident in comparison to hCLK1. The β-hairpin is replaced by a shorter flexible loop and the MAPK-like insertion comprises an extended loop followed by long α-helix instead of a short α-helix followed by a two-strand β-sheet. Upon closer inspection, a salt bridge is evident between R649 of the P+1 loop in the activation segment (R343 in hCLK1) and D690 located in a loop between αF and αG helix. The corresponding residue in hCLK1 is S384 and the salt bridge is therefore absent. Comparing the activation segment conformation between CmLIK-KD and hCLK1 they found that the salt bridge stabilizes it in the active (in hCLK1 unphosphorylated) conformation (Figure 1-3 B). They hypothesized that this salt bridge mediated CmLIK-KD activity at higher temperatures. To test this, they generated

a CmLIK-KD D690S mutant and observed reduced substrate phosphorylation at 48°C but increased overall auto phosphorylation (Figure 1-3 D). The melting temperature according to CD spectroscopy was reduced to 44°C. In turn a mouse CLK1 (mCLK1) S383D mutant exhibited detectable substrate phosphorylation at 40°C in comparison to no activity in the wildtype (WT). These initial results formed the basis for one of the projects presented in this thesis. Since this study was carried out with a synthetic substrate it remains to be determined if and how CmLIK-KD phosphorylates one of the *C. merolae* SR-proteins. In addition, the impact of the larger structural differences between CLKs and CmLIK-KD should be investigated.

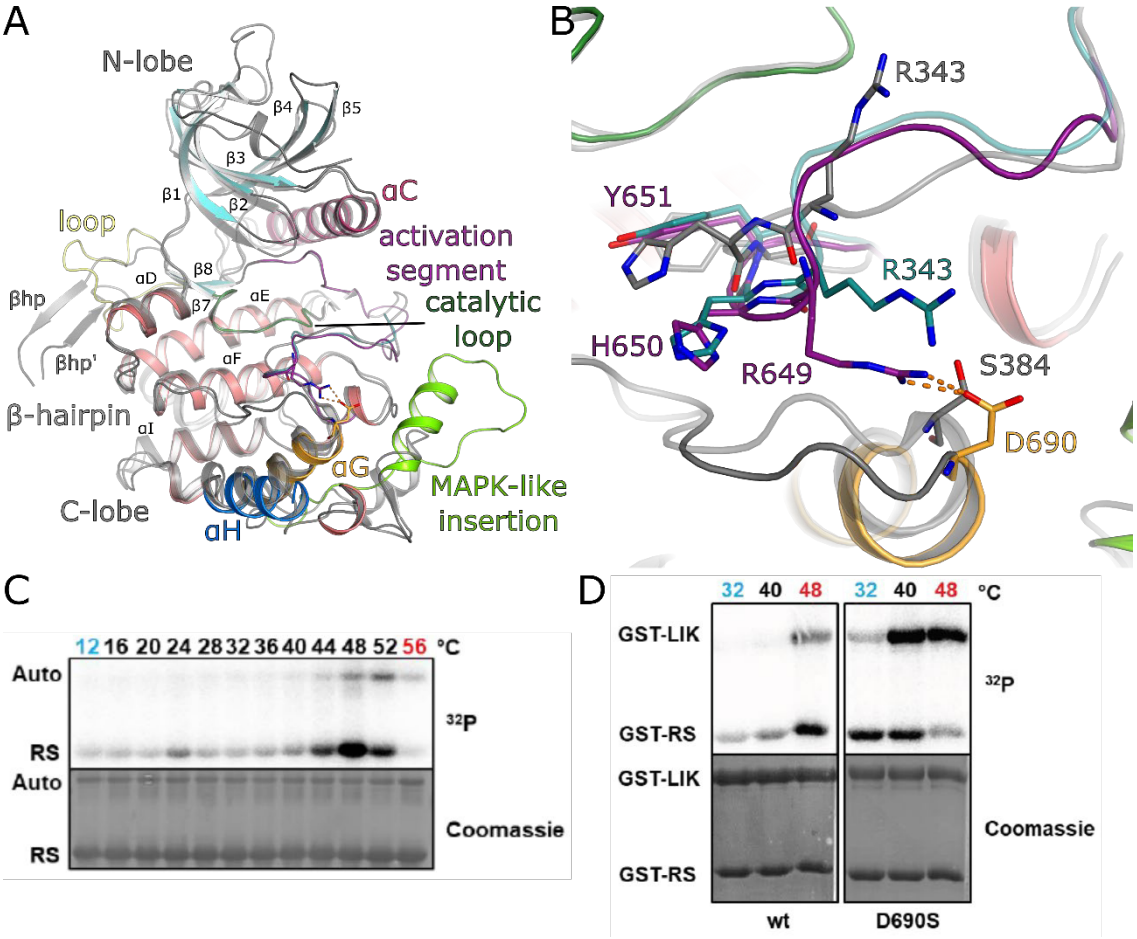

Figure 1-3 Initial analysis of CmLIK-KD. A Superimposition of the first obtained CmLIK-KD structure with hCLK1-KD. Proteins depicted as cartoon. For CmLIK-KD α-helices are colored in deep salmon and β-sheets aquamarine. Secondary structure element labeling according to (Bullock et al., 2009; Modi and Dunbrack, 2019) is indicated. Important structural elements are labeled in different colors. For hCLK1 kinase domain (grey, PDB: 6TW2 (Haltenhof et al., 2020)) β-hairpin is indicated. **B** Zoom of A on the R649-D690 salt bridge. The phosphorylated conformation of the hCLK1 activation segment is colored in grey and the unphosphorylated conformation in deep teal. Residues involved in the conformational change of the P+1 loop are depicted as sticks. **C** Representative gel of on-bead *in vitro* kinase assays of GST-CmLIK-KD WT with synthetic GST-RS

substrate. Kinase is indicated as "auto" and substrate as "RS" on the left. Sample temperature is indicated on top. Protein loading detected by Coomassie staining and phosphorylation detected by autoradiography (^{32}P) is shown. Taken from (Haltenhof, 2020). **D** Representative gels of on-bead *in vitro* kinase assays of GST-CmLIK-KD WT/D690S with synthetic GST-RS substrate. Kinase is indicated as "GST-LIK" and substrate as "GST-RS" on the left. CmLIK-KD variant is indicated on the bottom. Sample temperature is indicated on top. Protein loading detected by Coomassie staining and phosphorylation detected by autoradiography (^{32}P) is shown. Taken from (Haltenhof, 2020).

1.7 *Arabidopsis thaliana* – how plants adapt to elevated temperatures

Arabidopsis thaliana (*A. thaliana*) is a widely used model organism to study land plants (Woodward and Bartel, 2018). A process in plants that is especially interesting considering climate change is thermomorphogenesis (Erwin et al., 1989; Quint et al., 2016), the ability to adjust growth and morphology at high ambient temperatures below heat stress level. Since plants are sessile, they cannot move and must adapt in other ways in response to temperature changes. One observed morphological adjustment is hypocotyl elongation, growth of the stem (Gray et al., 1998). A second change is hyponastic growth, the elongation of the petioles and upwards movement of the leaves (van Zanten et al., 2010). Lastly the plants develop smaller and thinner leaves with decreased stomata density (Vile et al., 2012). All these morphological changes together contribute to enhanced evaporative cooling to mitigate the high temperatures (Crawford et al., 2012) and appeared to be mediated by the phytohormone auxin (indole-3-acetic acid, IAA) (Gray et al., 1998; Stavang et al., 2009; Wit et al., 2014). The transcription factor phytochrome-interacting factor 4 (PIF4) was identified as the major regulator of ambient temperature responses in *A. thaliana* (Koini et al., 2009; Proveniers and van Zanten, 2013). At high temperatures PIF4 binds its target promoters leading to expression of auxin biosynthesis genes such as YUCCA 8 (YUC8) (Sun et al., 2012). Elevated auxin levels in turn induce the expression of small auxin up RNA 1-24 (SAUR 19-24) genes (Franklin et al., 2011) which regulate elongation growth (Chae et al., 2012; Spartz et al., 2012; Spartz et al., 2014). A very simplified scheme of this cascade is shown in Figure 1-4 A. For thermomorphogenesis to function properly PIF4 activity needs to be tightly regulated. In addition to rhythmic PIF4 expression regulated by the circadian clock (Niwa et al., 2009; Nusinow et al., 2011), post translational modifications (Lorrain et al., 2008; Bernardo-García et al., 2014), interactions with other proteins (Foreman et al., 2011) and

competition for promoter binding (Toledo-Ortiz et al., 2014) have been reported as PIF4 regulatory mechanisms. Considering that alternative splicing is a common regulatory mechanism for protein activity, that several temperature dependent alternative splice events have been found in *A. thaliana* (Neumann et al., 2020) and the findings of temperature dependent activity of CLKs, it is not farfetched to surmise that plant CLK homologues play a regulatory role at some level in thermomorphogenesis.

Three CLK homologues were found in *A. thaliana*, AFC1-3 (Bender and Fink, 1994; Golovkin and Reddy, 1999; Rodriguez Gallo et al., 2022). Sequence identity between AtAFC1 and 2 is 70. 8 %, between 1 and 3 64.5 % and between 2 and 3 60.9 % (calculated with Clustal Omega (Madeira et al., 2022)). Their activation segments are highly similar to those of animal CLKs and especially the temperature sensitivity mediating residues of hCLK1 R343 and H344 are conserved (Figure 1-4 B). Previous members of the Heyd laboratory carried out *in vitro* kinase assays with GST-tagged full-length (f.l.) AFCs and a synthetic GST-RS substrate (Figure 1-4 C). They found that all three kinases exhibited distinct temperature activity profiles. AtAFC1 exhibited high substrate phosphorylation at and below 20°C and activity decreased steeply between 20°C and 32°C, with barely any detectable activity at higher temperatures. In contrast, AtAFC3 exhibited low substrate phosphorylation below 16°C followed by a steep increase until a maximum at 24°C. At 36°C AtAFC3 activity decreased again but was still detectable up to 40°C. AtAFC2 exhibited similar activity to AtAFC1 until 20°C but exhibited still higher activity between 24°C and 32°C, though not as high as AtAFC3. No activity could be detected at 36°C and above. Such distinct temperature activity profiles in a set of highly similar kinases prompt the investigation of their structural differences to elucidate elements governing their temperature sensitivity.

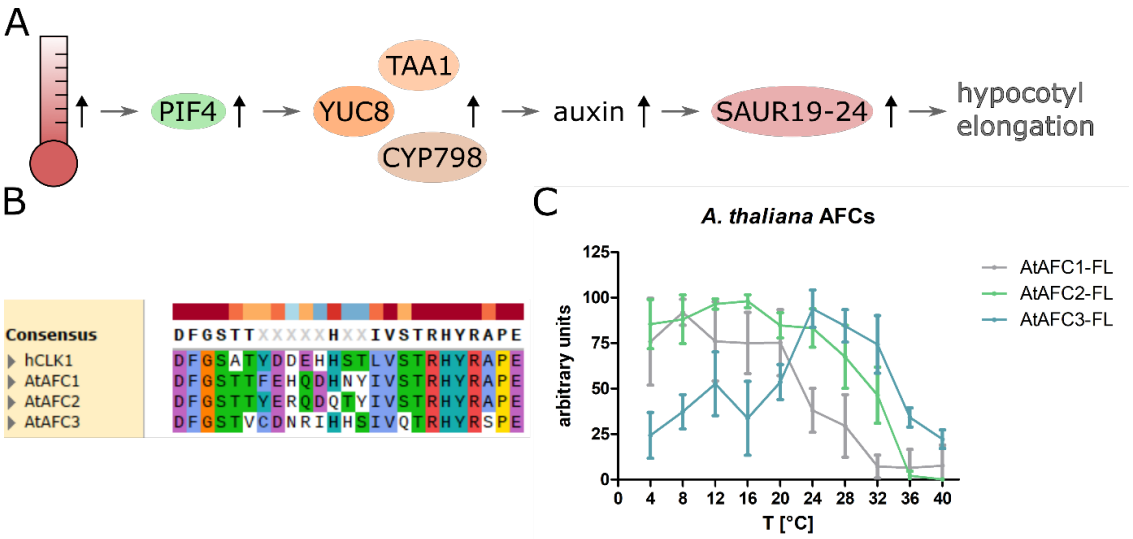

Figure 1-4 Thermomorphogenesis and CLK homologues in A. thaliana. A A very simplified scheme of the cascade mediating thermomorphogenesis in A. thaliana. Increase in temperature causes increased PIF4 expression which in turn increases expression of its target genes (YUC8, TAA1 and CYP798). This leads to more synthesis of the phytohormone auxin which leads to expression of SAUR19-24. These proteins facilitate hypocotyl elongation. Proteins are represented as ovals, black upwards arrows indicate upregulation and grey arrows indicate effects. Adapted from (Proveniers and van Zanten, 2013). **B** Multiple sequence alignment of hCLK1 and AtAFC1/2/3 activation segments. Conservation as colored blocks and consensus sequence shown on top. Residues colored according to properties and conservation (Clustal X color scheme). **C** Quantification of substrate phosphorylation observed in on-bead *in vitro* kinase assays of GST-AtAFC1/2/3 f.l. WT with synthetic GST-RS substrate at indicated temperatures. Phosphorylation was detected by autoradiography (^{32}P) and normalized to highest signal in assay. AtAFC1 n = 3, AtAFC2/3 n = 6. Experiments performed by Miriam Strauch and Paul Wulf.

2 Aims

Aim of this study was the characterization of the underlying molecular mechanisms that match the active temperature range of CLKs and their homologues to the body temperature or physiological environment temperature of their corresponding organisms. As methods for kinase characterization *in vitro* kinase assays, thermostability assays as well as structure elucidation using X-ray crystallography or AlphaFold prediction should be employed.

One approach followed the reconstruction of ancestral CLK sequences and analyzing their differences in amino acid sequences and protein structure in relation to their different temperature-activity profiles. This should shed light on the evolution of CLK temperature sensitivity during the evolution of different species.

A second approach investigated a CLK homologue from the extremophilic red algae *C. merolae*. Not only is this alga an established simple eukaryotic model organism, but the growth temperature of around 45°C requires a kinase that exhibits activity at higher temperatures and thus an attractive candidate for finding mechanisms that stabilize CLKs.

Lastly, three CLK homologues from *A. thaliana* were investigated with the reasoning that plants have to adapt to a wide range of temperatures since they can neither run nor hide. The presence of multiple homologues with distinct temperature-activity profiles suggests that each is used to adapt to a different temperature condition and poses an excellent opportunity to further analyze the molecular mechanisms governing kinase temperature sensitivity with respect to their high similarity.

Understanding the molecular mechanisms that govern the temperature sensitivity of CLKs and especially their plant homologues raises the possibility to engineer kinases in crop plants to adapt them to higher temperatures in the context of global warming.

3 Material and methods

If not stated otherwise, all chemicals were obtained from Carl Roth GmbH.

3.1 Molecular cloning and QuickChange PCR

Selected ancestral CLK f.l. sequences were ordered from Twist Bioscience in pETM-11 vector with 5' *NcoI* site and 3' *XhoI* site. KDs were re-cloned into pET-GST vector using PCR with the pETM-11 f.l. plasmids as templates and suitable primers, restriction digest with *NcoI* and *XhoI* and T4 DNA ligation. *Mus musculus* CLK4-KD (mCLK4-KD), *Alligator mississippiensis* CLK4-KD (AmCLK4-KD) and *Trachemys scripta scripta* CLK1-KD (turtle CLK1-KD) in pGex-6p-1 vector were already available in the laboratory. Similarly to the method described above CmSC35 was re-cloned from an existing plasmid out of the pET-MCN-A vector into pETM-11 vector. CmLIK-KD WT, D690S and hairpin mutant, as well as *A. thaliana* (At)AFC1, AtAFC2 and AtAFC3 f.l. WT in pGex-6P-1 vector were already available in the laboratory. CmLIK-KD T683V, AtAFC2 f.l. C210S and AtAFC3 f.l. Q254A mutants were generated via quick-change PCR. As described above AtAFC2-KD WT and C210S, as well as AtAFC3-KD WT were cloned out of the pGex-6P-1 vector into pETM-11 vector.

Human DYRK3 isoform 2 f.l. in pGex-4T1 and human Sec16 fragment (residues 1102-1405) in pMAL were supplied by Dr. Lucas Pelkmans from the University of Zurich. The Sec16 fragment was re-cloned into pET-GST vector as described above.

All primers were ordered from Eurofins. For all PCRs S7 Phusion polymerase (Biozym, 332530S) was used. FastDigest (Thermo Fisher) restriction enzymes were used with the supplied buffer. T4 DNA ligase from Thermo Fisher (EL0011) was used. Empty pETM-11 and pET-GST vectors were supplied by Dr. Bernhard Loll.

Chemically competent *Escherichia coli (E. coli)* Top10 for cloning and BL21(DE3) pRare for heterologous protein expression were transformed via heat shock at 42°C for 50 s. *E. coli* RosettaGami2 for expression of pETM-11 AtAFC2-KD WT and C210S were transformed using the ROTI®Transform kit (Carl Roth, P043.1) according to manufacturer's instructions.

3.2 Gene expression analysis via RT reaction and qPCR

RNA samples from *A. thaliana* Col-0 and *afc1/2/3* triple knockout plants cultured on 1 % (w/v) sugar supplemented medium at 17°C or 28°C for 8 and 24 h were provided by Dr. Daniel Maag from University of Würzburg. 1 µg of isolated RNA was incubated with 0.48 pmol reverse primer per target transcript and annealing was carried out using a temperature gradient from 90°C to 43°C in 1°C steps. 100 U M M-MuLV reverse transcriptase (Enzymatics # P7040L) was added to the mix and reaction allowed to go on for 30 min at 43°C. Resulting cDNA solutions were diluted with MilliQ H_2O to a final volume of 100 µL. qPCR was then performed in 96-well format with technical duplicates using Biozym Blue S'Green qPCR 2x mix (Biozym Cat # 331416) according to manufacturer's instructions in a Bioer Real-Time-Thermocycler LineGene 9600 Plus for 40 cycles. 8 µL of diluted cDNA was used in a final reaction volume of 20 µL with 5 pmol forward and 5 pmol reverse primer. Gene specific primers for *PIF4*, *YUC8*, *SAUR19* and *SAUR20* were used. AT4G34270 (*TIP41*) was used as a reference gene.

3.3 Reconstruction of ancestral CLK sequences

Ancestral CLK sequences were reconstructed by Dr. Rainer Merkl and Dr. Kristina Straub at University of Regensburg as described previously (Straub and Merkl, 2019). Initially sequences were searched via BLAST (Altschul et al., 1990) with hCLK1 as query and E-value set to 1^{-10}. Only sequences with a query coverage above 90 % were considered. Results were pruned by deselecting sequences with a sequence identity above 99 % and removing sequences that produced large indels in the multiple sequence alignment (MSA). Phylogenetic trees were calculated using Bayesian likelihood-based method and iteratively sequences were pruned to obtain a robust tree with bootstrap values greater than 0.75. The final tree was rooted using hDYRK1A sequence and used for reconstruction of ancestral CLK sequences using FastML (Ashkenazy et al., 2012).
For analysis and visualization of the resulting phylogenetic tree NJplot 2.3 (Perrière and Gouy, 1996) was used. MSAs were analyzed using JalView 2.11.3.2 (Waterhouse et al., 2009) and visualized with SnapGene Viewer 7.1.1 (www.snapgene.com). The body temperature or active ambient temperature of the organisms which constituted the phylogenetic tree were analyzed to select ancestral CLK sequences for further analysis.

3.4 Heterologous protein expression in *E. coli*

Recombinant proteins were expressed in *E. coli* BL21(DE3) pRare cultured in LB medium with 100 µg/mL ampicillin (pGex-6P-1 vector), or 50 µg/mL kanamycin (pETM-11 and pET-GST vector) and 34 µg/mL chloramphenicol by 0.2 mM IPTG induction at an OD_{600} of 0.8 – 1.0 and incubation overnight (ON) at 18°C. Cultures were harvested by centrifugation at 4.5 k x g, 4°C for 15 min and bacterial pellets stored at -20°C until use. For on-bead *in vitro* kinase assays (IVKA) bacterial cultures were induced with 0.4 mM IPTG and split into aliquots equaling a total OD_{600} of 80 prior to harvest via centrifugation. His-AtAFC2-KD WT and C210S were expressed in *E. coli* RosettaGami2 under the same conditions.

3.5 Purification of GST-tagged CmLIK-KD variants

Bacterial pellets (*E. coli* BL21(DE3) pRare, pGex 6P1) were resuspended in lysis buffer (50 mM Tris-HCl pH 7.0, 500 mM NaCl, 10 mM $MgCl_2$, 1 mM DTT), 1 mg DNase I (Roche, 10104159001) was added, cells lysed via sonification at 70 % amplitude, 1 s on, 2 s off for 17 min and centrifuged at 21.5 k x g, 4°C for 1 h. The supernatant was loaded onto 5 mL GST beads (Protino® Glutathione Agarose 4B, Macherey-Nagel REF# 745500). The beads were washed twice with 10 column volumes (CV) lysis buffer and the recombinant protein eluted with 5 CV elution buffer (50 mM Tris-HCl pH 8.5, 500 mM NaCl, 10 mM $MgCl_2$, 1 mM DTT, 20 mM glutathione) in 1 CV fractions. Fractions were analyzed via SDS-PAGE and protein concentrations measured via spectrophotometry using a NanoDrop (DeNovix DS-11) considering the molecular weight and extinction coefficient of the protein of interest. Subsequently fractions containing the protein of interest were pooled, PreScission protease (inhouse production at AG Wahl) was added 1:30 to cleave off the GST-tag and the mixture was dialyzed ON at 4°C in 6-8 kDa MWCO dialysis tubing (Spectrum™, 132660) against 2 L dialysis buffer (50 mM Tris-HCl pH 7.0, 300 mM NaCl, 10 mM $MgCl_2$, 1 mM DTT). The dialyzed mixture was loaded onto 5 mL GST-beads again, the flow-through (FT) was collected, beads washed with 3 CV dialysis buffer and bound protein eluted with 3 CV elution buffer. FT and wash fractions were analyzed via SDS-PAGE and protein concentrations measured via spectrophotometry using a NanoDrop (DeNovix DS-11) considering the molecular weight and extinction coefficient of the

protein of interest. Subsequently FT and wash fractions containing the protein of interest were pooled, concentrated in an Amicon Ultra-15 10 kDa MWCO filter unit (Millipore, UFC901024) and subjected to size exclusion chromatography (SEC) using a HiLoad Superdex S75 16/600 pg column (Cytiva, GE28-9893-33) on a Quest system (BioRad). The pooled fractions were loaded manually onto a 2 mL loop. Flow was set to 1 mL/min, loop was emptied with 10 loop volumes and isocratic elution carried out with 1.2 CV SEC-buffer (50 mM Tris-HCl pH 8.0, 300 mM NaCl, 10 mM $MgCl_2$, 1 mM DTT) while collecting 1.5 mL fractions. Fractions were analyzed via SDS-PAGE according to the chromatogram and protein concentrations measured via spectrophotometry using a NanoDrop (DeNovix DS-11) considering the molecular weight and extinction coefficient of the protein of interest. Subsequently fractions containing the pure protein of interest were pooled, concentrated in an Amicon Ultra-4 10 kDa MWCO filter unit (Millipore, UFC801024) and aliquoted prior to flash freezing in liquid nitrogen and storage at -80°C. For CmLIK-KD D690S the pH of the lysis and dialysis buffers was 7.2. For CmLIK-KD hairpin the pH of all buffers was 8.5. The final protein concentration of CmLIK-KD T683V was 26 µM, of D690S 29 µM and of hairpin 49 µM. CmLIK-KD WT was already available at 65 µM in the laboratory, purified previously by Ana Kotte.

3.6 Purification of His-tagged CmSC35

Bacterial pellets (*E. coli* BL21 pRare, pETM-11 CmSC35) were resuspended in lysis buffer (50 mM Tris-HCl pH 8.0, 500 mM NaCl), 1 tablet cOmplete protease inhibitor (EDTA-free, Roche) and 1 mg DNase I (Roche, 10104159001) were added, cells lysed via sonification at 70 % amplitude, 1 s on, 2 s off for 17 min and centrifuged at 21.5 k x g, 4°C for 1 h. Supernatant was loaded onto 1 mL NiNTA beads (HIS-Select® Nickel Affinity Gel, Sigma Aldrich P6611-25ML). The beads were washed with 10 CV lysis buffer, 10 CV lysis buffer with added 20 mM imidazole and the recombinant protein eluted with 5 CV elution buffer (50 mM Tris-HCl pH 8.0, 500 mM NaCl, 250 mM imidazole) in 1 CV fractions. Fractions were analyzed via SDS-PAGE. Subsequently fractions containing the protein of interest were pooled and diluted with 50 mM Tris-HCl pH 8.0 for a final concentration of 100 mM NaCl. The protein was further purified using a HiTrap Heparin HP 5 mL column (Cytiva, 17-0407-03) on a Quest system (BioRad). The column was equilibrated with 1 CV

buffer A (50 mM Tris-HCl pH 8.0, 0.1 M NaCl) and the protein solution was loaded with a flow rate of 0.5 mL/min. The column was washed with 1 CV buffer A. Elution was carried out at a flow rate of 1 mL/min with a gradient from 0 to 100 % buffer B (50 mM Tris-HCl pH 8.0, 1 M NaCl) over 10 CV followed by a step with 1 CV 100 % buffer B. During elution 1 mL fractions were collected. According to the chromatogram, fractions were analyzed via SDS-PAGE. Fractions containing the protein of interest were pooled and subjected to SEC using a HiLoad Superdex S75 16/600 pg column (Cytiva, GE28-9893-33) on a Quest system (BioRad). The pooled fractions were loaded manually onto a 5 mL loop. Flow was set to 1 mL/min, loop was emptied with 2 loop volumes and isocratic elution carried out with 1.2 CV SEC-buffer (50 mM Tris-HCl pH 8.0, 300 mM NaCl) while collecting 1.5 mL fractions. Fractions were analyzed via SDS-PAGE according to the chromatogram and protein concentrations measured via spectrophotometry using a NanoDrop (DeNovix DS-11) considering the molecular weight and extinction coefficient of the protein of interest. Subsequently fractions containing the pure protein of interest were pooled, concentrated in an Amicon Ultra-4 10 kDa MWCO filter unit (Millipore, UFC801024) to a final concentration of 68 µM and aliquoted prior to flash freezing in liquid nitrogen and storage at -80°C.

3.7 Purification of GST-tagged AtAFC3 f.l. variants

GST-AtAFC3 f.l. WT was purified only by affinity chromatography as described for GST-CmLIK-KD variants (see paragraph 3.5), but using 1 mL GST beads and pooled eluate fractions were concentrated in an Amicon Ultra-0.5 50 kDa MWCO filter unit (Millipore, UFC505024) to a final concentration of 57 µM and aliquoted prior to flash freezing in liquid nitrogen and storage at -80°C.

GST-AtAFC3 f.l. Q254A was purified as described for GST-CmLIK-KD variants (see paragraph 3.5) with the following changes. 2 mL GST beads were used during affinity chromatography. The GST-tag was not cleaved off and pooled fractions after affinity chromatography were directly concentrated and subjected to SEC using a HiLoad Superdex S200 16/600 pg column (Cytiva, GE28-9893-35) on an Äkta pure system (Cytiva). The loop was emptied with 2 loop volumes. The final concentration was 14 µM and 95 µM.

As lysis buffer for GST-AtAFC3 f.l. variants 50 mM Tris-HCl pH 7.2, 500 mM NaCl, 10 mM $MgCl_2$, 1 mM DTT was used. The elution buffer had the same composition with added 20 mM glutathione. The SEC buffer comprised 50 mM Tris-HCl pH 7.2, 300 mM NaCl, 10 mM $MgCl_2$, 1 mM DTT.

3.8 Purification of His-tagged AtAFC3-KD WT

His-AtAFC3-KD WT was purified as described for His-CmSC35 (see paragraph 3.6) with the following changes. Eluate fractions of the NiNTA affinity chromatography containing the protein of interest were concentrated in an Amicon Ultra-4 10 kDa MWCO filter unit (Millipore, UFC801024) and subjected to SEC. A 2 mL loop was used and emptied with 10 loop volumes. The final concentration amounted to 38 µM. Lysis buffer comprised 50 mM Tris-HCl pH 8.0, 500 mM NaCl, 10 mM $MgCl_2$ and SEC buffer 50 mM Tris-HCl pH 8.0, 300 mM NaCl, 10 mM $MgCl_2$.

3.9 On-bead *in vitro* kinase assays

Per investigated kinase and 9 reactions one bacterial pellet equaling a total OD_{600} of 80 was thawed and resuspended in 700 µL lysis buffer (50 mM Tris-HCl pH 7.4, 300 mM NaCl, 2 mM DTT). Cells were lysed via sonification at 40 % amplitude, 0.4 cycle for 1 min and cell debris cleared by centrifugation at 13 k x g, 4°C for 15 min. The cleared lysate supernatant was incubated for 1 h at 4°C with 100 µL 50:50 slurry Protino® Glutathione Agarose 4B (Macherey-Nagel, REF 745500) equilibrated with lysis buffer. Incubated beads were centrifuged at 500 x g, 4°C for 2 min, the supernatant discarded, and beads subsequently washed 4 times with 1 mL lysis buffer via centrifugation at 500 x g, 4°C for 1 min. The 50 µL bead pellet after washing was resuspended in lysis buffer to a final volume of 1 mL. Per reaction 100 µL of the bead slurry were used. The beads were centrifuged once more at 500 x g, 4°C for 1 min and the supernatant discarded. 14 µL 13.8 µM GST-RS synthetic substrate in reaction buffer (50 mM Tris-HCl pH 7.6, 10 mM $MgCl_2$, 5 mM DTT, 0.1 mM spermidine) was added to the beads per reaction and pre-incubated for 20 min at the indicated temperatures. After addition of ATP mixture (γ-^{32}P-ATP : ATP 1 : 20k, ca. 0.3 Ci/mmol) to a final concentration of 22 µM the samples were incubated for 5 min at the same temperatures. The reaction was stopped by addition of

6 x SDS sample buffer and incubation at 95°C for 5 min. Samples were analyzed on 12 % SDS-PAGEs. Gels were stained with Coomassie, de-stained with 10 % (v/v) acetic acid, 40 % (v/v) ethanol and imaged. Subsequently gels were placed on filter paper, dried in a gel drier for 45 min and exposed on phosphoscreens ON. The phosphoscreens were detected in a Typhoon FLA 7000 phosphoimager (650 nm laser, latitude L4, PMT = 500, 100 µm pixel size) and band intensities quantified using ImageQuant TL software. Intensities were normalized to highest signal in assay, divided into auto and substrate phosphorylation. For further analysis GraphPad Prism 9.3.0 was used. Statistically significant differences were determined by two-way ANOVA with Šídák correction. Curve fitting was performed using nonlinear regression with Boltzmann sigmoidal fitting. The resulting best fit values were used to calculate the temperature at which CLK4-KD activity reached 50 % according to equation 1 (see Supplement). Standard deviation was calculated with error propagation according to equation 2 (see Supplement). Statistically significant differences were determined by two-way ANOVA followed by a Tukey HSD post-hoc test.

Synthetic GST-RS substrate was already available as purified protein in the laboratory, previously purified by Paul Wulf.

3.10 *In vitro* kinase assays with purified CmLIK-KD variants

0.5 µM purified CmLIK-KD WT, T683V, D690S or hairpin mutant was pre-incubated with 1 µM CmSC35 in kinase assay buffer (50 mM MES-KOH pH 6.0, 10 mM $MgCl_2$) for 10 min at the indicated temperatures. After addition of ATP mixture (γ-^{32}P-ATP : ATP 1 : 120k, ca. 0.05 Ci/mmol) to a final concentration of 133 µM the samples were incubated for 30 min at the same temperatures. The reaction was stopped by addition of 6 x SDS sample buffer and incubation at 95°C for 5 min. Samples were analyzed on 12 % SDS-PAGEs. Gels were stained with Coomassie, de-stained with 10 % (v/v) acetic acid, 40 % (v/v) ethanol and imaged. Subsequently gels were placed on filter paper, dried in a gel drier for 45 min and exposed on phosphoscreens ON. The phosphoscreens were detected in a Typhoon FLA 7000 phosphoimager (650 nm laser, latitude L4, PMT = 500, 100 µm pixel size) and band intensities quantified using ImageQuant TL software. Intensities were normalized to highest signal in assay, divided into auto and substrate

phosphorylation. Statistically significant differences determined by unpaired Welch t-test using GraphPad Prism 9.3.0.

3.11 *In vitro* kinase assays with purified AtAFC3 f.l. variants

0.5 µM purified GST-AtAFC3 f.l. WT or Q254A was pre-incubated with 2 µM GST-RS in reaction buffer (50 mM Tris-HCl pH 7.6, 10 mM $MgCl_2$, 5 mM DTT, 0.1 mM spermidine) for 20 min at the indicated temperatures. After addition of ATP mixture (γ-^{32}P-ATP : ATP 1 : 20k, ca. 0.3 Ci/mmol) to a final concentration of 22 µM the samples were incubated for 5 min at the same temperatures. The reaction was stopped by addition of 6 x SDS sample buffer and incubation at 95°C for 5 min. Samples were analyzed as described for *in vitro* kinase assays with purified CmLIK-KD variants (see paragraph 3.10).

3.12 Thermal shift assays

CmCLK-KD was mixed with kinase assay buffer (50 mM MES-KOH pH 6.0, 10 mM $MgCl_2$) containing 1:500 SYPRO® Orange Protein Gel Stain (Sigma-Aldrich, S5692) to a final concentration of 1.7 µM in a final volume of 20 µL. The mixture was incubated in a Stratagene Mx3005P Real-Time-Thermocycler (Agilent Technologies) with a temperature range from 25°C to 95°C with a ramp of 1°C/min over 70 min and fluorescence measured. The reaction was also carried out with 500 µM ATP or 500 µM AMPPNP in the mixture, as well as all three conditions also with addition of 1 µM CmSC35. The assay was carried out in 96-well plate format with triplicate measurements. The minima of the second derivate of the resulting fluorescence curves were calculated with Excel and GraphPad Prism 9.3.0 to obtain T_m values. The final T_m values were calculated as the mean of the triplicates and errors were calculated as the standard deviation. Statistically significant differences were determined by unpaired Welch t-test.

3.13 Phosphorylation quantification via intact mass LC-ESI-MS

3.13.1 CmLIK-KD and His-CmSC35 phosphorylation

10 µM CmLIK-KD variant was incubated with 5 µM His-CmSC35 in 50 mM MES-KOH pH 6.0, 10 mM $MgCl_2$ for 10 min at 32°C, 45°C or 49°C. ATP was added to a final

concentration of 2 mM in a final reaction volume of 30 µL and the reaction further incubated at the set temperature. 5 µL sample was taken 2, 5, 10, 20 and 30 min after ATP addition and the reaction was stopped by dilution in 45 µL TA33 (33 % (v/v) acetonitrile (ACN), 0.1 % (v/v) trifluoroacetic acid (TFA) in H_2O). Samples were stored at -20°C until use. The remaining 5 µL after 30 min were diluted with 5 µL 6 x SDS-sample buffer, boiled for 5 min at 95°C and stored at -20°C until they were used for in-gel digest analysis (see paragraph 3.14).

3.13.2 Intact mass LC-ESI-MS

10 µL of each sample was diluted with 30 µL buffer A (0.1 % (v/v) formic acid (FA) in H_2O) to lower ACN concentration. Intact proteins were analyzed using the Ultimate 3000 liquid chromatography system connected to a Q Exactive HF mass spectrometer via the ion max source with HESI-II probe (Thermo Scientific). The following MS source parameters were used: spray voltage 3.6 kV, capillary temperature 320°C, sheath gas 10, auxiliary gas 4, S-lens RF level 60, intact protein mode on. For the analysis 10 µL (approx. 0.13 µg of total protein) of the sample were desalted and concentrated by injection on a reversed-phase cartridge (MSPac DS-10, 2.1×10 mm, Thermo Scientific) at 60°C using buffer A (0.1 % (v/v) FA, 5 % (v/v) ACN in H_2O) at a constant flow rate of 22 µL/min for 3 min. This was followed by a short linear gradient of 5 % – 95 % buffer B (0.1 % (v/v) FA in 80 % (v/v) ACN, 20 % (v/v) H_2O) within 10 min followed by washing and re-equilibration. Full MS spectra were acquired using the following parameters: mass range m/z 600–2500, resolution 15,000, AGC target $3x10^6$, µscans 5, maximum injection time 200 ms. Spectra were deconvoluted, processed, analyzed and peaks quantified using UniChrom of the UniDec software suite (Marty et al., 2015). An averaged spectrum was generated from each measurement, followed by spectral deconvolution using the default settings except for the following adjustments: charge range 1-100, mass range 22-46 kDa, sample mass every 1 Da, peak picking range 10 Da. For further analysis GraphPad Prism 9.3.0 was used and catalytic rates calculated using nonlinear regression with a one phase decay.

3.14 Phosphorylation site analysis via in-gel digest and LC-ESI-MS/MS

3.14.1 SDS-PAGE and band excision

SDS-PAGE samples from CmLIK-KD variant and His-CmSC35 phosphorylation (see paragraph 3.13) corresponding to 2 µg CmLIK-KD and 0.6 µg His-CmSC35 were loaded onto 12 % (v/v) polyacrylamide gels. Gels were run at 100 V for 10 min and subsequently 150 V for 2 h. After staining with Coomassie, the gels were destained with 10 % (v/v) acetic acid and washed with MilliQ H_2O. Protein bands were excised from the gels and cut into approximately 1 mm wide pieces to maximize surface area. Half of each band was used for digestion with trypsin and the other half for digestion with elastase. Both approaches were handled simultaneously. Gel pieces were incubated with 25 mM ammonium bicarbonate, 50 % (v/v) ACN at 45°C for 15 min. Supernatant was removed and gel pieces incubated with ABC buffer (50 mM ammonium bicarbonate) at 45°C for 15 min. Supernatant was again removed, gel pieces incubated with ACN at 45°C for 10 min, supernatant removed and gel pieces dried in a SpeedVac.

3.14.2 Reduction and carbamidomethylation of cysteines

Gel pieces were incubated with 100 mM DTT in ABC buffer at 56°C for 30 min. Supernatant was removed, gel pieces incubated with ACN at 45°C for 5 min and supernatant removed again. For carbamidomethylation gel pieces were incubated with 55 mM iodoacetamide in ABC buffer at RT for 20 min protected from light. Supernatant was removed and the gel pieces washed once with ABC buffer for 10 min at RT and twice with ACN for 5 min at RT before being dried in a SpeedVac again.

3.14.3 Enzymatic digest

15 µL 10 ng/µL trypsin in ABC buffer or 10 µL 10 ng/µL elastase in ABC buffer was added to the corresponding gel pieces, followed by addition of 20 µL ABC buffer and incubation at 37°C ON.

3.14.4 Peptide extraction for LC-ESI-MS/MS analysis

50 µL 0.5 % (v/v) TFA in ACN was added to the gel pieces and the mixture was incubated for 5 min in an ultrasonic bath. Supernatants were transferred into a 96-well plate. 50 µL ACN was added to the gel pieces, incubated for 10 min at RT and the supernatant combined with the first supernatant. Peptides were dried in a SpeedVac and stored at -20°C until use.

3.14.5 LC-ESI-MS/MS analysis

Peptides were reconstituted in 10 µL of 0.05 % (v/v) TFA, 4 % (v/v) ACN in water, and 1 µL was analyzed using an Ultimate 3000 reversed-phase capillary nano liquid chromatography system connected to a Q Exactive HF mass spectrometer (Thermo Fisher Scientific). Samples were injected and concentrated on a trap column (PepMap100 C18, 3 µm, 100 Å, 75 µm i.d. x 2 cm, Thermo Fisher Scientific) equilibrated with 0.05 % (v/v) TFA in water. After switching the trap column inline, LC separations were performed on a capillary column (double nanoViper PepMap Neo C18, 2 µm, 100 Å, 75 µm i.d. x 50 cm, Thermo Fisher Scientific) at an eluent flow rate of 300 nL/min. Mobile phase A contained 0.1 % (v/v) FA in water, and mobile phase B contained 0.1 % (v/v) FA in 80 % (v/v) ACN / 20 % (v/v) water. The column was pre-equilibrated with 5 % mobile phase B followed by an increase of 5 – 44 % mobile phase B over 35 min. Mass spectra were acquired in a data-dependent mode utilizing a single MS survey scan (m/z 300–1650) with a resolution of 60,000, and MS/MS scans of the 15 most intense precursor ions with a resolution of 15,000. The dynamic exclusion time was set to 20 s and automatic gain control was set to $3x10^6$ and $1x10^5$ for MS and MS/MS scans, respectively. Reconstitution and measurement were carried out by Dr. Benno Kuropka. Obtained .raw files were converted to mzML file format with MSConvert from the ProteoWizard software package (Chambers et al., 2012). Peptide identification and quantification was done with FragPipe (v21.1, (Kong et al., 2017)) using the LFQ-Phospho workflow. For trypsin samples “stricttrypsin” and for elastase samples “nonspecific” were used as enzyme specificity in MSFragger. As FASTA sequence database, the sequences of the purified and digested CmLIK-KD and undigested His-CmSC35 proteins supplemented with decoys, common contaminants and the proteome of *E. coli* strain K12

(UP000000625) was used. Data of phosphorylated residues was further analyzed with Excel and GraphPad Prism 9.3.0.

3.15 CmLIK-KD hairpin nucleotide exchange

10 µM CmLIK-KD hairpin was incubated with 1 mM AMPPNP (Jena Bioscience, NU-407-10) in exchange buffer (50 mM Tris-HCl pH 8.5, 300 mM NaCl, 300 mM $(NH_4)_2SO_4$, 10 mM EDTA, 2 mM DTT) for 1 h at room temperature (RT). The exchange was quenched by addition of $MgCl_2$ to a final concentration of 20 mM and incubation on ice for 5 min. The protein was concentrated and washed three times with washing buffer (50 mM Tris-HCl pH 8.5, 300 mM NaCl, 1 mM DTT) in an Amicon Ultra-0.5 10 kDa MWCO filter unit (Millipore, UFC501024) to get rid of ammonium sulfate and EDTA.

3.16 Protein crystallization

3.16.1 CmLIK-KD WT crystallization

5.6 mg/mL CmLIK-KD WT and 4 mg/mL His-CmSC35 in the presence of 3 mM ATP-γ-S (Roche, 11162306001) and 4.5 mM $MgCl_2$ were crystallized in hanging drop format with 1 µL protein solution + 1 µL reservoir solution drops and 1 mL reservoir solution (0.1 M Tris-HCl pH 8.0, 20 % (v/v) ethanol) at 18°C. Crystals were soaked in reservoir solution supplemented with 20 % (w/v) ethylene glycol for cryo protection, flash frozen in liquid nitrogen for storage and used for X-ray diffraction experiments at BESSY II (Helmholtz-Zentrum (HZB), Berlin, Germany), beamline 14-2.

3.16.2 CmLIK-KD hairpin crystallization

2.2 mg/mL CmLIK-KD hairpin was used for crystallization trials in sitting drop format with 0.1 µL protein solution and 0.1 µL reservoir solution drops in 96-well plate format. Plates were prepared using a mosquito® LV pipetting robot (sptlabtech) and incubated at 4°C. The Classics Suite (Qiagen), PEG I suite (Qiagen), PEG II suite (Qiagen) and Index (Hampton research) screens were used for initial crystallization trials. Initial hit conditions are listed in Table 2. Fine screens based on the conditions PEG I G4 and PEG II H10 were carried out in sitting drop format in a 48-well plate, with 1 µL protein solution and 1 µL reservoir solution drops and 200 µL reservoir solution at

4°C. The fine screens yielded rod/envelope shaped crystals in 0.25 M calcium acetate, 4 % (w/v) PEG-8000 (well A6). Crystals were soaked in reservoir solution supplemented with either 20 % (w/v) ethylene glycol or 30 % (w/v) glycerol for cryo protection, flash frozen in liquid nitrogen for storage and used for X-ray diffraction experiments at BESSY II, beamline 14-2. Crystals of the same crystal form were obtained in 0.25 M calcium acetate, 6 % (w/v) PEG-8000 (FS#1B6) and used to prepare a seed stock. Larger crystals of the same form were obtained after longer time in 0.25 M calcium acetate, 14 % (w/v) PEG-3350 (well A2). Crystals were soaked in reservoir solution supplemented with 20 % (w/v) ethylene glycol for cryo protection, flash frozen in liquid nitrogen for storage and used for X-ray diffraction experiments at PETRA III (Deutsches Elektronen-Synchrotron (DESY), Hamburg, Germany), beamline P11.

For seed stock preparation crystals and the complete drop were transferred into a tube containing a PTFE Seed Bead™ (Hampton research, HR2-320) and 50 µL reservoir solution and vortexed twice for 30 s with a 30 s pause on ice in between. Afterwards 150 µL reservoir solution was added, the tube vortexed briefly and the generated seed stock transferred to a new tube and stored at 4°C.

2.3 mg/mL CmLIK-KD hairpin with nucleotide exchanged to AMPPNP (see paragraph 3.15) was used in a new fine screen around hit conditions of the first fine screen with streak seeding using the FS#1B6 seed stock. The fine screen was carried out in the same format as the first and seeding was done in dilution by successively streaking through quadruplicate drops with a cat whisker. 0.25 M calcium acetate, 4 % (w/v) PEG-8000 with streak seeding yielded bigger, bipyramidal crystals. These were soaked in reservoir solution supplemented with either 20 % (w/v) ethylene glycol or 30 % (w/v) glycerol for cryo protection, flash frozen in liquid nitrogen for storage and used for X-ray diffraction experiments at BESSY II, beamline 14-2.

The previous fine screen was repeated in part with 2.6 mg/mL CmLIK-KD hairpin with nucleotide exchanged to AMPPNP in the same way. Bipyramidal crystals obtained in the same condition were soaked in reservoir solution supplemented with 20 % (w/v) ethylene glycol for cryo protection, flash frozen in liquid nitrogen for storage and used for X-ray diffraction experiments at PETRA III, beamline P11.

3.16.3 His-AtAFC3-KD WT crystallization trials

1.6 mg/mL His-AFC3-KD WT was used for crystallization trials in sitting drop format with 0.1 µL protein solution + 0.1 µL reservoir solution drops in 96-well plate format. Plates were prepared using a mosquito® LV pipetting robot (sptlabtech) and incubated at 18°C. The Classics Suite (Qiagen) and Index (Hampton research) screens were used for crystallization trials.

3.17 X-ray diffraction experiments and structure modelling

All X-ray diffraction experiments at BESSY-II and PETRA III and dataset procession using XDSAPP (Krug et al., 2012) were carried out by Dr. Bernhard Loll. Data was further handled with the PHENIX suite (Liebschner et al., 2019). Data quality was assessed with Xtriage and phasing performed with molecular replacement using Phaser-MR (McCoy et al., 2007) and the previously obtained CmLIK-KD WT structure as search model. The model resulting from molecular replacement was further refined in iterative cycles with phenix.refine (Afonine et al., 2012) and manual rebuilding in Coot 0.9.6 (Emsley et al., 2010). MolProbity (Williams et al., 2018) was used for structure data validation. Polder electron density maps were calculated using phenix.polder (Liebschner et al., 2017).

3.18 AlphaFold prediction of ancestral CLK4-KD structures

The structures of selected reconstructed ancestral CLK-KDs were predicted using AlphaFold 2.3.1 (Jumper et al., 2021) in monomeric mode running on the high-performance computer at ZEDAT, FU Berlin (Bennett et al., 2020). Per kinase the model with highest ranking was used for analysis. Models were analyzed using PyMOL 2.3.4 (Schrödinger and DeLano, 2020).

3.19 Structural analysis of AtAFC AlphaFold predictions

To assess structural differences in the AFC family predictions of full-length *A. thaliana* AFC1, AFC2 and AFC3 structures by AlphaFold (Jumper et al., 2021) published in the AlphaFold protein structure database (Varadi et al., 2022) as entries P51566 (AtAFC1), P51567 (AtAFC2) and P51568 (AtAFC3) were used. For analysis only the kinase domains, AtAFC1 residues 89-467, AtAFC2 residues 72-427 and AtAFC3 residues 46-400 were

considered. Structure data was analyzed with PyMOL 2.3.4 (Schrödinger and DeLano, 2020) and Coot 0.9.6 (Emsley et al., 2010). Similarity of structures was calculated with the rigid jFATCAT algorithm (Ye and Godzik, 2003; Li et al., 2020) via the RCSB PDB pairwise structure alignment tool.

4 Results

4.1 Gradual evolution of temperature sensitivity in kinases – a function older than CLKs

Aiming to investigate how the temperature activity profiles of CLKs from different organisms evolved to accommodate their body or habitat temperatures we selected 231 CLK1 and CLK4 sequences from different animals. Our cooperation partners from the University of Regensburg, Dr. Rainer Merkl and Dr. Kristina Straub, iteratively calculated several phylogenetic trees, pruned the used sequences until they obtained a phylogenetic tree suitable for ancestral sequence reconstruction and rooted the tree with DYRK1 as outgroup (Figure 6-1). Here we focused on the smaller CLK4 tree in general and especially on the differences between bird and turtle ancestors (Figure 4-1 A). Both groups are closely related but show stark differences in body / habitat temperature – birds being homeotherm with body temperatures around 41°C (Prinzinger et al., 1991) and turtles being poikilotherm with active temperatures between 28°C and 33°C (Crawshaw et al., 1980). This placed them as good candidates to investigate the diverging evolution between homeotherm and poikilotherm animals and closely related CLKs that should possess highly different temperature activity profiles. First, we aligned the sequences of three reconstructed ancestral CLKs with the sequences of chicken, soft-shell turtle, alligator and mouse (Figure 4-1 B). The chosen reconstructed sequences were: N3 for all CLK4s, N7 the turtle ancestor and N9 the bird ancestor. All sequences showed over 80 % identity with the lowest identity being between mouse and soft-shell turtle at 80.5 %. As expected, most variations were found in the variable N-terminus. Since previous studies of our lab showed that the kinase domain was sufficient to display a CLKs temperature activity profile (Haltenhof et al., 2020) we focused on differences in the kinase domain.

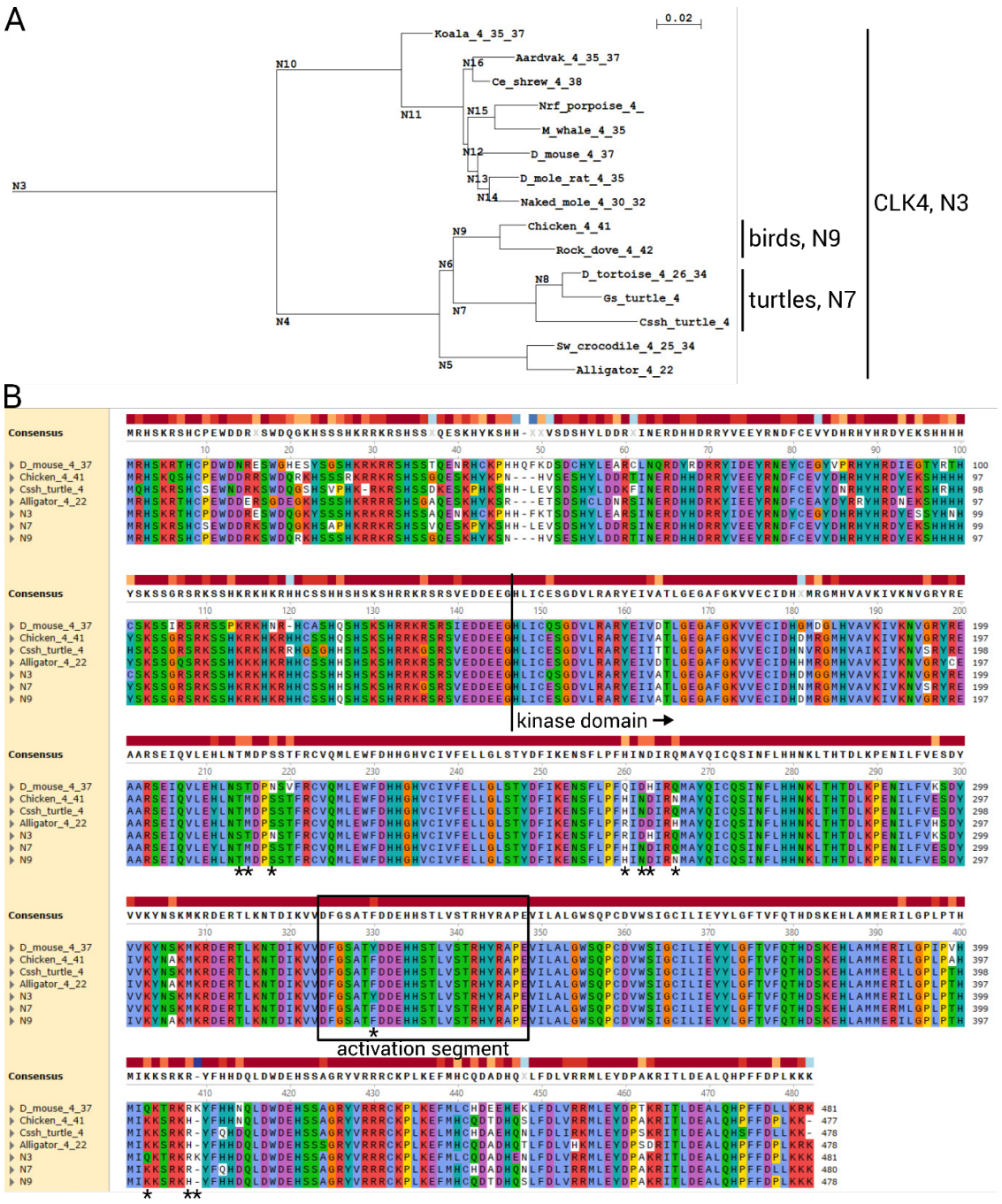

Figure 4-1 Reconstruction of ancestral CLK4 sequences. A Phylogenetic tree of selected CLK4 sequences. Calculated as part of a phylogenetic tree also comprising selected CLK1s and rooted with DYRK1 as outgroup (Figure 6-1) by Dr. Rainer Merkl and Dr. Kristina Straub. Species are labeled as "species_CLK1/4_body temperature or active temperature range in °C if applicable". Identifiers of calculated ancestral sequences are indicated at branches. Branch length scale indicated on top. Ancestral CLK4s that were further used and their corresponding branches indicated on the right. **B** Multiple sequence alignment of selected existing CLK4 sequences (mouse, chicken, turtle and alligator) and three reconstructed ancestral CLK4s – N3 common, N7 turtle and N9 bird CLK4 ancestor. Conservation as colored blocks and consensus sequence shown on top. Residues colored according to properties and conservation (Clustal X color scheme). Kinase domain and activation segment are indicated. Asterisks indicate residues that differ between N3 and N9 and exhibited changes in interactions in AlphaFold predictions (Figure 4-2).

4.1.1 AlphaFold predictions facilitate exploration of interaction differences due to residue changes in reconstructed ancestral CLK4s.

The effect of differences in protein sequence are not necessarily clear from the sequence alone. Therefore, we performed AlphaFold monomer predictions for the kinase domains of N3, N9 and N7. All adopted the typical kinase fold and no differences in overall folding could be observed (Figure 4-2 A, Figure 4-3 A). In Figure 4-2 A and B a superimposition of N3 and N9 is shown. Residues that differ between both kinases were depicted as sticks and their interacting residues examined. We observed three clusters of differing interactions. The corresponding residues are marked with asterisks in the multiple sequence alignment (Figure 4-1 B). At the N-terminal end of the αE helix D261 in N3 forms a salt bridge to R259 in the loop before it, possibly stabilizing this region more (Figure 4-2 C). In N9 this salt bridge is absent and N259 just forms an H-bond with R262, an interaction that is negligible due to both residues already being part of the αE helix. In the C-lobe of N3 R407 forms H-bonds to I401 and H412 and stabilizes a loop in the MAPK-like insertion after the αG helix (Figure 4-2 D). The orientation of R407 is facilitated by the insertion of an additional residue, K408, in comparison to N9. The most striking difference in interaction is at Y329 of the activation segment of N3 which forms an H-bond to H210 of the αC helix (Figure 4-2 E). This interaction that stabilizes the activation segment is absent in N9, where the corresponding residue is F327 which is unable to form an H-bond. H210 of N3 is further stabilized by H-bonds to S213 and T214 via its backbone oxygen. The only interaction network that is more stabilizing in N9 is around S215 in the loop directly C-terminal of the αC helix, with H-bonds to D213 and T217. Overall N3 appeared to display more stabilizing H-bond networks, leading to the hypothesis that N3 would exhibit a temperature activity profile shifted to higher temperatures compared to N9.

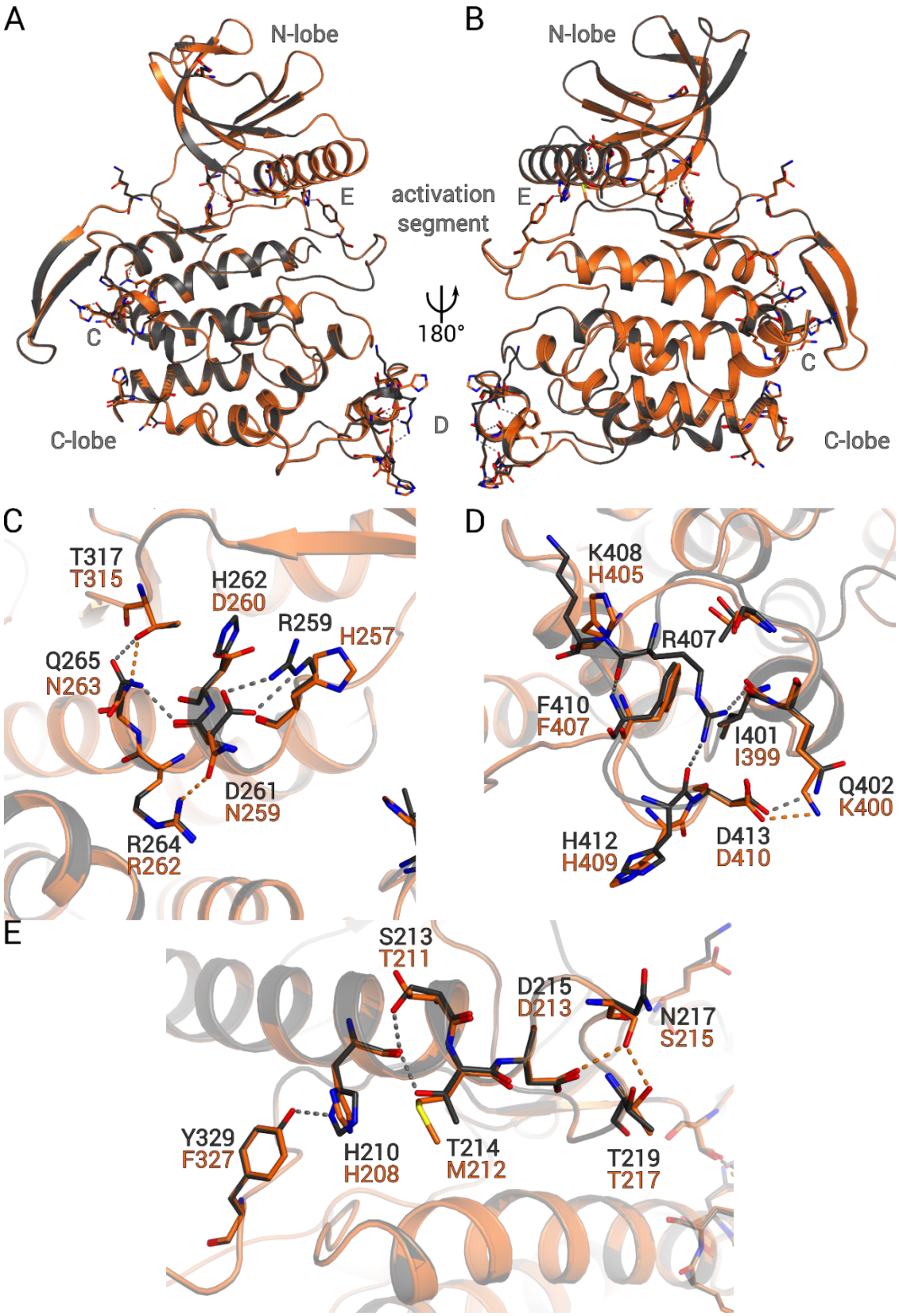

Figure 4-2 Kinase domain structure comparison of CLK4 N3 and N9. A AlphaFold predictions of the kinase domains of CLK4 N3 (residue 146-481) and N9 (residue 144-478) overlaid with each other. N3 is depicted in dark grey and N9 in orange. Overall structure is depicted as cartoon. Residues differing between N3 and N9 (but not N7) and their interacting residues are depicted as sticks. H-bonds (distance cut-off = 3.2 Å) from N3 are colored light grey and from N9 orange. N-lobe, C-

lobe and activation segment are indicated as orientation aide. Areas depicted in C-E are indicated with the corresponding letter. **B** Image as in A, turned 180° around Y axis. **C** Zoom-in on interaction networks in the C-lobe. Residues are labelled in the corresponding color of the kinase. **D** Zoom-in on interaction network around R407 of N3 close to the LAMMER motif. Labeling as in C. **E** Zoom-in on interaction network around H210 of N3, influencing the activation segment around Y329. Labeling as in C.

Comparing the AlphaFold predictions of N9 and N7 no differences in overall folding were evident (Figure 4-3 A). Mapping the residues in which both kinases differed yielded two interactions that changed. In N7 Y210 of the αC helix formed an H-bond with N280 of the αE helix, bridging N- and C-lobe (Figure 4-3 B). This could potentially influence the dynamic shift of both lobes to one another. On the other hand, N263 of the αE helix of N9 formed an H-bond to T315 of the β-hairpin which was not predicted for Q265 of N7 (Figure 4-3 C). Due to the lack of distinct interaction differences between both kinases we could not form a hypothesis on their temperature activity profiles, but since turtles are active at lower temperatures than the body temperature of birds, we proposed that N7 would exhibit a temperature activity profile shifted to lower temperatures compared to N9.

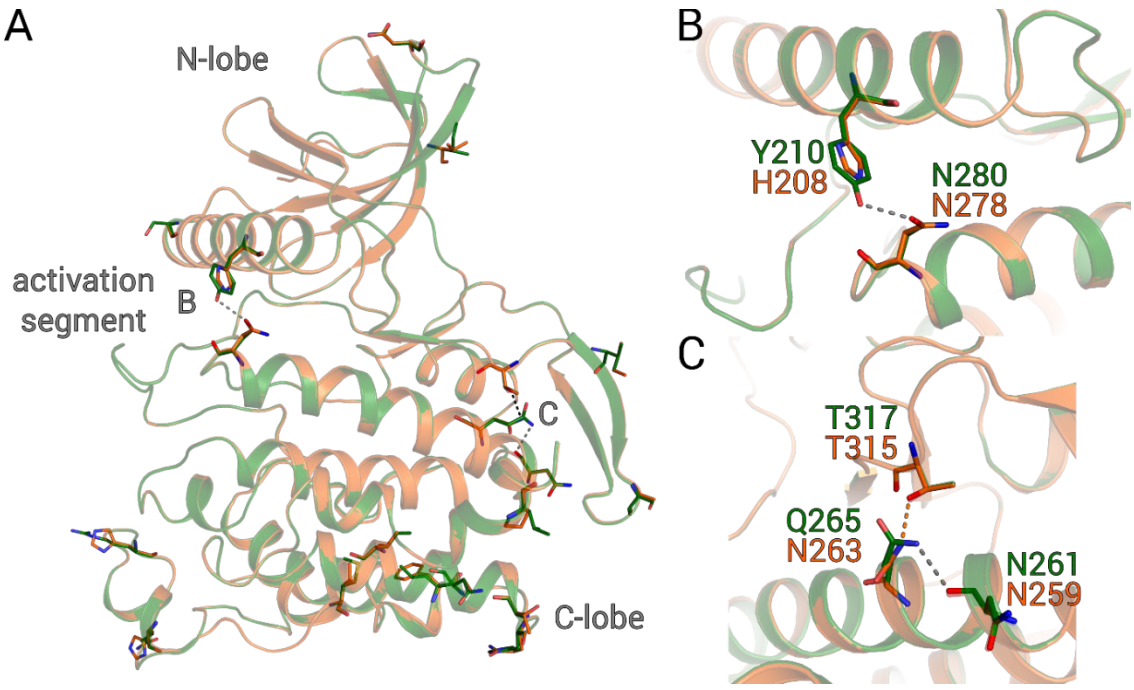

Figure 4-3 Kinase domain structure comparison of CLK4 N7 and N9. A AlphaFold predictions of the kinase domains of CLK4 N7 (residue 146-480) and N9 (residue 144-478) overlaid with each other. N7 is depicted in green and N9 in orange. Overall structure is depicted as cartoon. Residues differing between N7 and N9 and their interacting residues are depicted as sticks. H-bonds (distance cut-off = 3.2 Å) from N7 are colored light grey and from N9 orange. N-lobe, C-lobe and

activation segment are indicated as orientation aide. Areas depicted in B and C are indicated with the corresponding letter. **B** Zoom-in on interaction of N7 Y210 close to the activation segment. Residues are labelled in the corresponding color of the kinase. **C** Zoom-in on interactions of residue 265/263 in both kinases in the C-lobe. Labeling as in B.

4.1.2 *In vitro* kinase assays reveal a gradual shift in CLK temperature activity profiles from a common ancestor towards living species.

To elucidate the temperature activity profiles of the reconstructed ancestral CLKS we ordered the sequences of N3, N7, N9 and chicken CLK4 as synthetic genes optimized for expression in *E. coli*, re-cloned the kinase domains into pET-GST vector and expressed them in *E. coli* BL21(DE3) pRare. In addition, we also expressed GST-tagged mouse and alligator CLK4-KD and turtle CLK1-KD. These constructs were already available in the laboratory. The expressed proteins were used for on-bead *in vitro* kinase assays with synthetic GST-RS substrate.

N3, the ancestor to all CLK4s exhibited a similar auto phosphorylation activity compared to mouse CLK4 as a control (Figure 4-4 A, B). Substrate phosphorylation was significantly elevated at 35°C and 38°C. In comparison N9, the bird ancestor, also exhibited elevated auto phosphorylation at 35°C and 38°C in addition to even further elevated substrate phosphorylation at 38°C. Furthermore, substrate phosphorylation was still detectable at 40°C. Auto phosphorylation at 35°C was even more pronounced in chicken CLK4 even though it was slightly decreased at 38°C compared to N9. Substrate phosphorylation by chicken CLK4 was comparable to N9, with activity at 35°C in general higher. The dip in auto and substrate phosphorylation at 33°C between high activity at 31°C and 35°C by chicken CLK4 was reproducible and no effect of unequal protein loading as is evident in Coomassie staining (Figure 4-4 A). 50 % substrate phosphorylation could be observed at 36.5°C with N3, 38.2°C with N9, 38.0°C with chicken, and 33.3°C with mouse CLK4 (Figure 4-4 C). The temperature activity profiles show a gradual evolution to higher temperatures from N3 to chicken via N9. For mouse CLK4 the temperature activity profile shifted towards lower temperatures compared to the N3 ancestor.

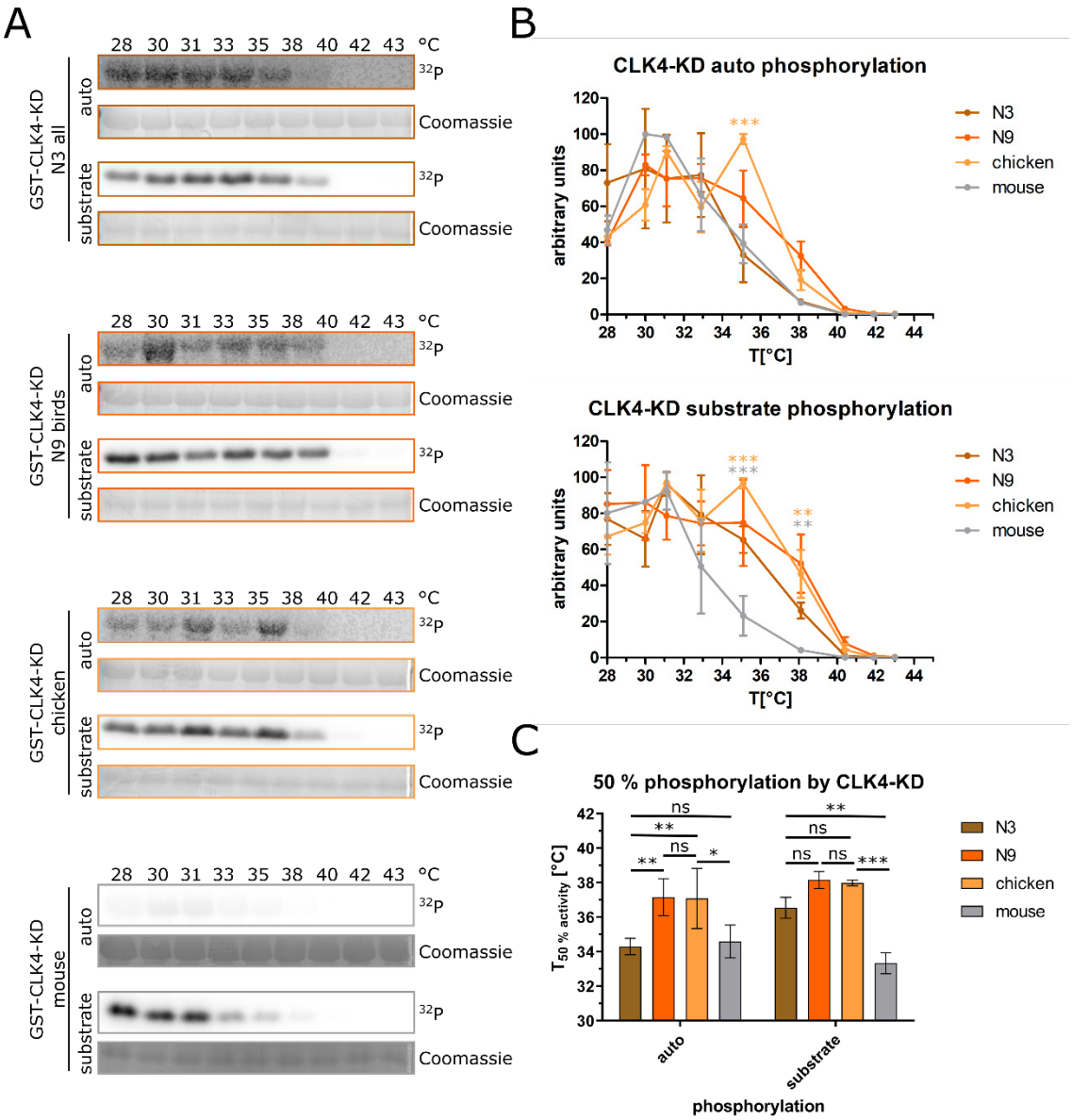

Figure 4-4 Development of ancestral CLK4 temperature-activity profiles towards birds. **A** Representative gels of on-bead *in vitro* kinase assays of GST-CLK4-KD N3, N9, chicken and mouse with synthetic GST-RS substrate. Respective kinase is indicated on the left and sample temperature is indicated on top. Protein loading detected by Coomassie staining and phosphorylation detected by autoradiography are shown for the kinase (auto) and substrate. **B** Quantification of auto and substrate phosphorylation from the on-bead *in vitro* kinase assays in A. Radioactive signal was normalized to highest signal in assay. Shown are mean and standard deviation. Respective kinase is indicated in the legend on the right. Statistically significant differences between N3 and other kinases determined by two-way ANOVA with Šídák correction are indicated as asterisks in the color corresponding to the kinase (*: $p < 0.05$, **: $p < 0.01$, ***: $p < 0.001$). N3 n = 3, N9 and chicken n = 4, mouse n = 2. **C** Temperature at which CLK4-KD activity reaches 50 %. Calculated by nonlinear regression with Boltzmann sigmoidal fitting from the data in B. Standard deviation was calculated with error propagation. Statistically significant differences determined by two-way ANOVA followed by a Tukey HSD *post-hoc* test are indicated as asterisks (*: $p < 0.05$, **: $p < 0.01$, ***: $p < 0.001$).

In agreement with previous assays (Haltenhof et al., 2020) alligator CLK4 and turtle CLK1 displayed temperature activity profiles shifted to even lower temperatures than mouse CLK4, both in auto and substrate phosphorylation. In contrast to our expectations and the observed intermediate shift in the temperature activity profile of N9 towards chicken CLK4, N7 CLK4 exhibited significantly elevated auto phosphorylation between 35°C and 40°C compared to N3 (Figure 4-5 A, B). This shift was even more pronounced than for N9 and chicken, especially at 40°C. Substrate phosphorylation was also significantly elevated even compared to N9 and chicken at 38°C and 40°C. 50 % substrate phosphorylation could be observed at 32.1°C with turtle CLK1 and alligator CLK4, and at 39.3°C with N7 CLK4 (Figure 4-5 C). While we could show a gradual evolution of temperature activity profiles from a common CLK4 ancestor towards birds, we could not show the same kind of evolution towards turtles.

4.1.3 Temperature dependent activity of DYRK3 shows that thermosensitivity did not evolve in CLKs.

To broaden our understanding of the evolution of thermosensitivity in kinases we looked at the family closest to CLKs, the DYRK kinase family of which DYRK1 was used as an outgroup for the construction of the CLK1/4 phylogenetic tree. GST-tagged human DYRK3 isoform 2 was used in on-bead *in vitro* kinase assays with a GST-tagged section of its physiological substrate Sec16 (residues 1102-1405) (Figure 4-6 A, B). Similar to hCLK1 (Haltenhof et al., 2020) we observed highest activity below 37°C. While the decline of activity between 35°C and 38°C appeared to be rather shallow, a steep decline in phosphorylation between 38°C and 39°C was evident. The observation of temperature dependent DYRK3 activity is surprising, considering that the activation segment of DYRK3 exhibits only 44 % sequence identity to hCLK1 (Figure 4-6 C, calculated with Clustal Omega (Madeira et al., 2022)) and that it lacks the histidine (hCLK1 H343) which was shown to mediate hCLK1 thermosensitivity and was sufficient to introduce thermosensitivity in hSRPK1 (Haltenhof, 2020). These results suggest that thermosensitivity did not evolve in the CLK family, but before DYRK and CLK families diverged.

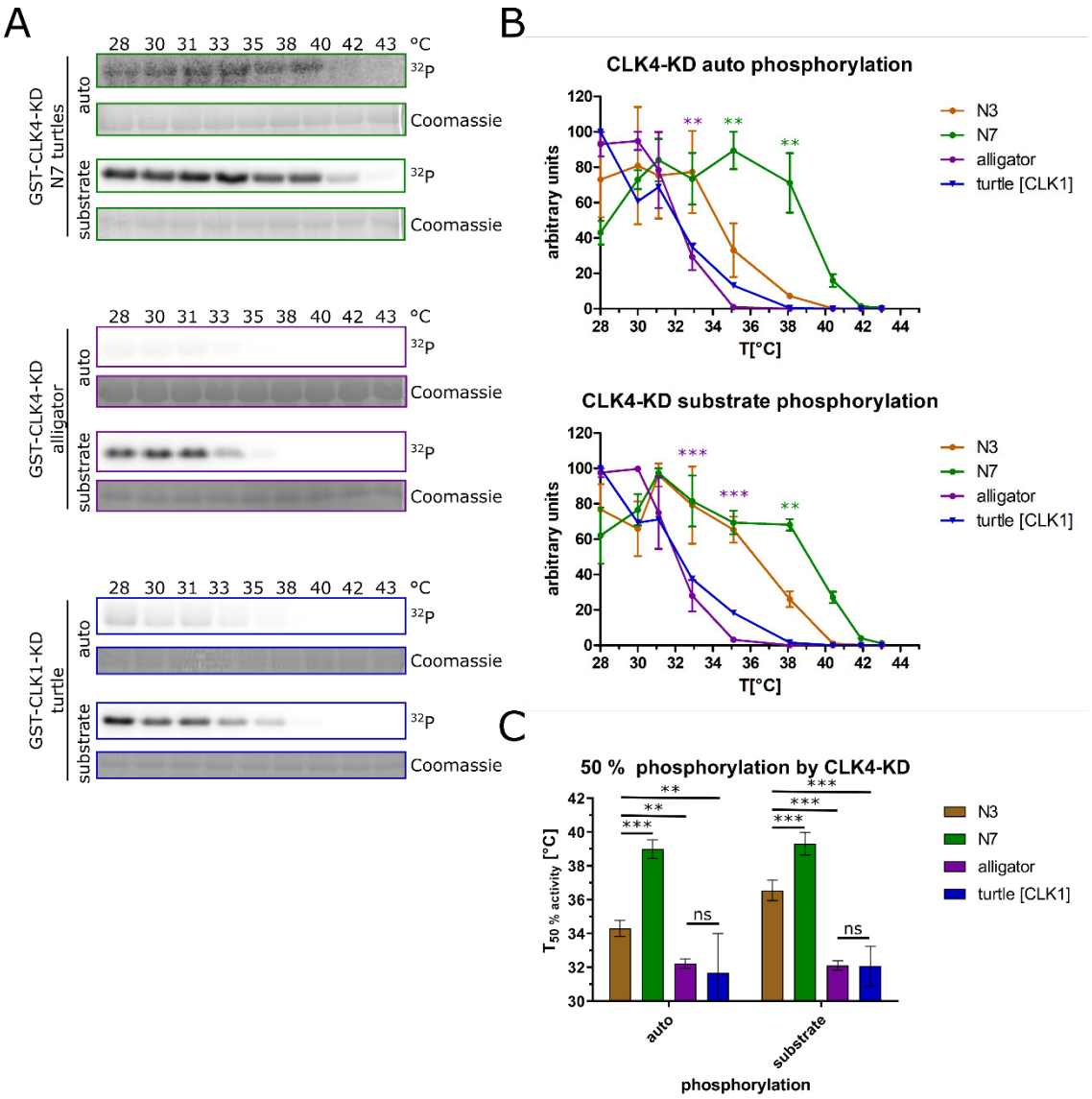

Figure 4-5 Development of ancestral CLK4 temperature-activity profiles towards reptiles. **A** Representative gels of on-bead *in vitro* kinase assays of GST-CLK4-KD N7 and alligator and GST-CLK1-KD turtle with synthetic GST-RS substrate. Respective kinase is indicated on the left and sample temperature is indicated on top. Protein loading detected by Coomassie staining and phosphorylation detected by autoradiography are shown for the kinase (auto) and substrate. **B** Quantification of auto and substrate phosphorylation from the on-bead *in vitro* kinase assays in A. N3 data is taken from Figure 4-4. Radioactive signal was normalized to highest signal in assay. Shown are mean and standard deviation. Respective kinase is indicated in the legend on the right. Statistically significant differences between N3 and other kinases determined by two-way ANOVA with Šídák correction are indicated as asterisks in the color corresponding to the kinase (*: $p < 0.05$, **: $p < 0.01$, ***: $p < 0.001$). N3 and N7 n = 3, alligator n = 2, turtle n = 1. **C** Temperature at which CLK4-KD activity reaches 50 %. Calculated by nonlinear regression with Boltzmann sigmoidal fitting from the data in B. Standard deviation was calculated with error propagation. Statistically significant differences determined by two-way ANOVA followed by a Tukey HSD *post-hoc* test are indicated as asterisks (*: $p < 0.05$, **: $p < 0.01$, ***: $p < 0.001$).

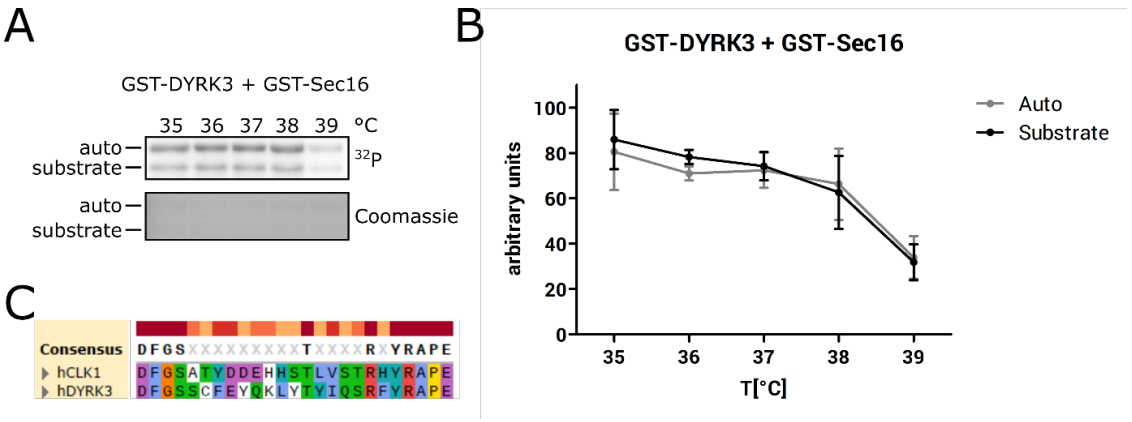

Figure 4-6 GST-DYRK3 exhibits temperature dependent phosphorylation of GST-Sec16. **A** Representative gel of on-bead *in vitro* kinase assays of GST-DYRK3 (full length isoform 2, Uniprot O43781-2) with GST-Sec16 (residues 1102-1405) as substrate. Sample temperature is indicated on top. Protein loading detected by Coomassie staining and phosphorylation detected by autoradiography are shown for the kinase (auto) and substrate. **B** Quantification of auto and substrate phosphorylation from the on-bead *in vitro* kinase assays in A. Radioactive signal was normalized to highest signal in assay. Shown are mean and standard deviation. n = 3. **C** Multiple sequence alignment of hCLK1 (residues 325-349) and DYRK3 (residues 335-359) activation segments. Conservation as colored blocks and consensus sequence shown on top. Residues colored according to properties and conservation (Clustal X color scheme).

4.2 *C. merolae*– adapting kinase activity to inhabiting sulfuric hot springs

As stated in the introduction *C. merolae* is well suited as a model organism to study splicing due to its low complexity. Its extreme habitat, as well as its genetic ancientness also make it a suitable candidate to study the evolution and adaptation of its molecular mechanisms and proteins.

4.2.1 CmLIK-KD phosphorylates CmSC35 in a temperature dependent manner.

In this context we continued to investigate the *C. merolae* CLK homologue CmLIK. Previously the activity of CmLIK-KD was only investigated using a synthetic GST-RS substrate in on-bead *in vitro* kinase assays (Haltenhof, 2020). We cloned, expressed and purified one of the two *C. merolae* SR-proteins, CmSC35, the homologue to human SRSF2 (Stark et al., 2015) and used it as a substrate in *in vitro* kinase assays with CmLIK-KD WT (Figure 4-7). For auto phosphorylation we observed a peak at 49°C in agreement with previous observations, where the maximum was observed at 52°C. However, where GST-RS was also phosphorylated the most at 48°C (Figure 1-3 C) we observed maximum CmSC35 phosphorylation at 32°C. Substrate phosphorylation decreased with increasing temperature. At 45°C, the habitat temperature, CmSC35 phosphorylation amounted to 50 % relative to maximum observed activity. While at 49°C still over 25 % activity was observed, this was decreased to below 10 % at 52°C and barely any activity could be observed at 54°C. Unlike for other CLKs auto phosphorylation and substrate phosphorylation do not correlate for CmLIK-KD and CmSC35. As auto phosphorylation increases, substrate phosphorylation decreases.

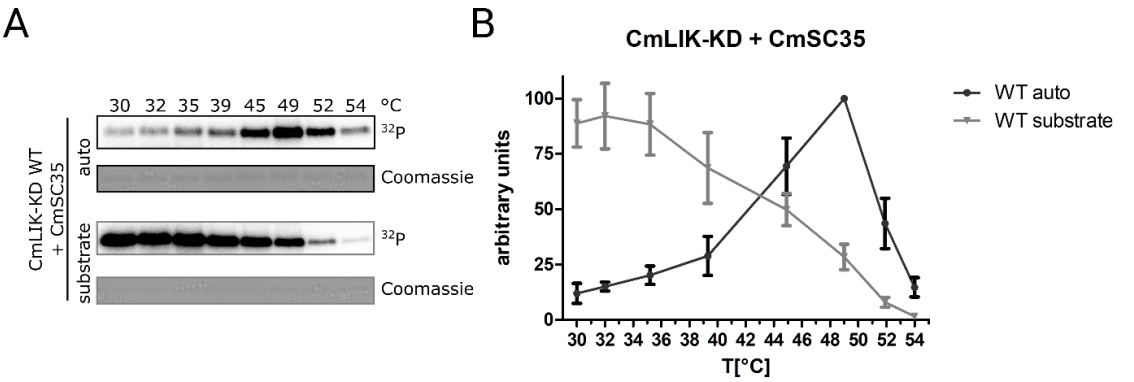

Figure 4-7 CmLIK-KD phosphorylates itself and CmSC35 in a temperature dependent manner. **A** Representative SDS-PAGE gel of *in vitro* kinase assays of purified CmLIK-KD WT with physiological CmSC35 substrate. Sample temperature is indicated on top. Protein loading detected by Coomassie staining and phosphorylation detected by autoradiography are shown for the kinase (auto) and substrate. **B** Quantification of auto and substrate phosphorylation from the *in vitro* kinase assays in A. Radioactive signal was normalized to highest signal in assay. Shown are mean and standard deviation. The mean of all experiments was taken. n = 8.

4.2.2 Characterization of CmLIK-KD nucleotide binding and auto interaction.

Since we already obtained a crystal structure of the CmLIK kinase domain we aimed to co-crystallize it with its physiological substrate CmSC35 in the presence of a non-hydrolysable ATP analogue to elucidate the substrate binding mode. We managed to obtain rod-shaped crystals of the space group $P2_12_12_1$. While the spacegroup was the same as from the first obtained structure, the unit cell parameters differed, all axes being longer in the new crystals (Table 3). The crystals yielded a structure at 2.69 Å resolution and the asymmetric unit comprised only two copies of CmLIK-KD. No binding of CmSC35 could be observed (Figure 4-8 A). Superimposition of both CmLIK-KD copies on each other (Figure 6-3 A) revealed that chain B (deep teal) adopted a more open conformation with a shifted N-lobe in relation to chain A (grey). The closed conformation is the completely active conformation while the open conformation is the switch between inactive and active conformation (Kornev et al., 2006). In both chains the coordinated adenosine of the nucleotide is visible (Figure 4-8 B, Figure 6-3 B). While polder electron density maps support that these atoms are indeed present (Figure 4-8 C, Figure 6-3 C), no electron density could be observed for the phosphate groups, suggesting that the nucleotides were completely dephosphorylated. In addition to the polder electron density maps the presence of the adenosine is supported by the sidechain position of

L555, which is flipped out of the nucleotide binding pocket in comparison to the first obtained structure without bound nucleotide where it blocks the pocket (Figure 6-3 D). Here we could show the adenosine coordinating residues in CmLIK being the backbone of E553, H554 and L474.

We could observe one interaction interface between both chains, comprising the loop after the αH helix of chain B and the N-lobe of chain A (Figure 4-8 D). Here E767-B forms an H-bond to the backbone of V453-A, K481-A located in β2 forms an H-bond with the backbone of H769-B, S476-A located in β1 forms an H-bond to P774-B and E775-B forms an H-bond to R500-A, located between β3 and αC helix. The last 7 C-terminal residues of both chains could not be built. But the C-terminus of chain B is located in such a way, that the C-terminal tail could protrude towards the catalytic center of chain A (Figure 4-8 A). This could suggest that the observed interactions between both chains are not only crystal contacts, but part of the interaction during trans auto phosphorylation of CmLIK-KD.

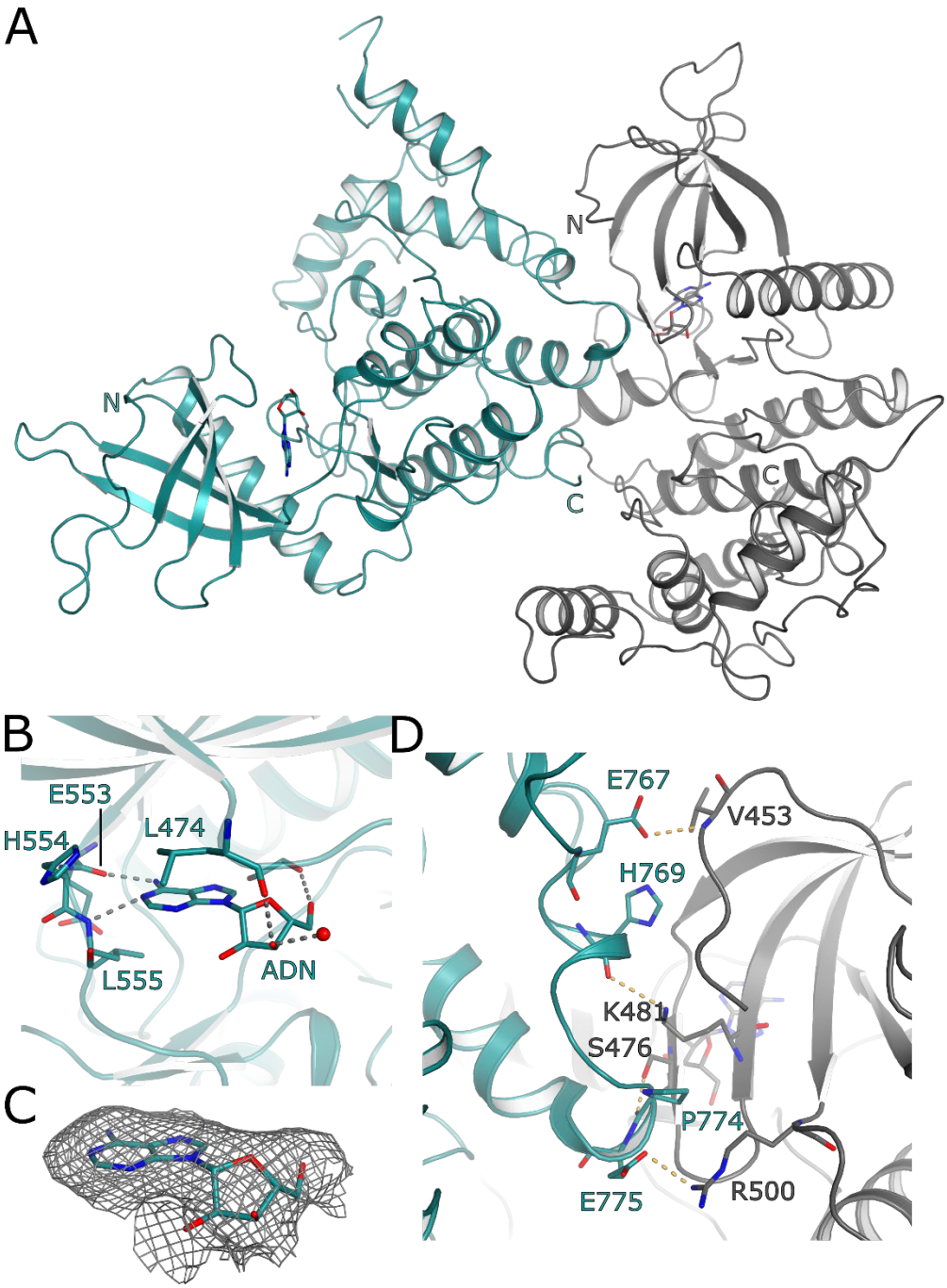

Figure 4-8 CmLIK-KD WT structure with bound adenosine. A Asymmetric unit contents of CmLIK-KD WT structure at 2.69 Å resolution. Protein depicted as cartoon, chain A colored in grey, chain B in deep teal. Nucleotide depicted as sticks. N- and C-termini of are indicated. **B** Nucleotide binding pocket of chain B. Residues interacting with adenosine depicted as sticks and labeled. **C** Polder electron density map of chain B adenosine contoured at σ = 3.0. **D** Interactions of chain B C-lobe with chain A N-lobe. Interacting residues are depicted as sticks and labeled. H-bonds (distance cut-off = 3.2 Å) are depicted as dashed lines in bright orange.

4.2.3 CmLIK-KD exhibits an inhibitory auto phosphorylation close to the activation segment at T683.

Upon further inspection difference density near chain B T683 suggested the presence of a phosphorylation at this residue (Figure 4-9 A). A polder electron density map supported the presence of TPO683 in chain B (Figure 4-9 B). The phosphate group forms two H-bonds, to E677 of the αF helix and to Y651 of the activation segment (Figure 4-9 A). These interactions might stabilize the activation segment of CmLIK in a phosphorylation-dependent manner. To elucidate the potential role of CmLIK auto phosphorylation at T683 we cloned and purified a T683V exchange mutant. In *in vitro* kinase assays the mutant exhibited slightly decreased auto phosphorylation below 39°C and significantly increased CmSC35 phosphorylation at 39°C and 45°C (Figure 4-9 C, D). Apo CmLIK-KD T683V exhibited a melting temperature (T_m) decreased by 0.4°C compared to the WT (Figure 4-9 E). While the presence of ATP increased the T_m of the WT by 4.9°C, this increase was reduced in T683V to 2.7°C, yielding a $\Delta\Delta T_m$ of -2.3°C. The presence of a non-hydrolysable ATP analogue, AMPPNP, led to a T_m increase by 1.5°C, 1.3°C respectively, yielding only a $\Delta\Delta T_m$ of -0.3°C. Thus, the abolishment of CmLIK T683 leads to a significant decrease of phosphorylation dependent protein stabilization. Together these results suggest that CmLIK exhibits an auto phosphorylation at T683, among other sites. This auto phosphorylation likely stabilizes the activation segment, and thus the kinase, in a conformation that is less favorable for substrate phosphorylation. The CmLIK-KD T683 auto phosphorylation could not be detected via LC-ESI-MS/MS after in-gel digest with elastase, but the data showed low peptide counts and intensities for residue T683 in general due to its position in the protein, so this does not disprove the auto phosphorylation.

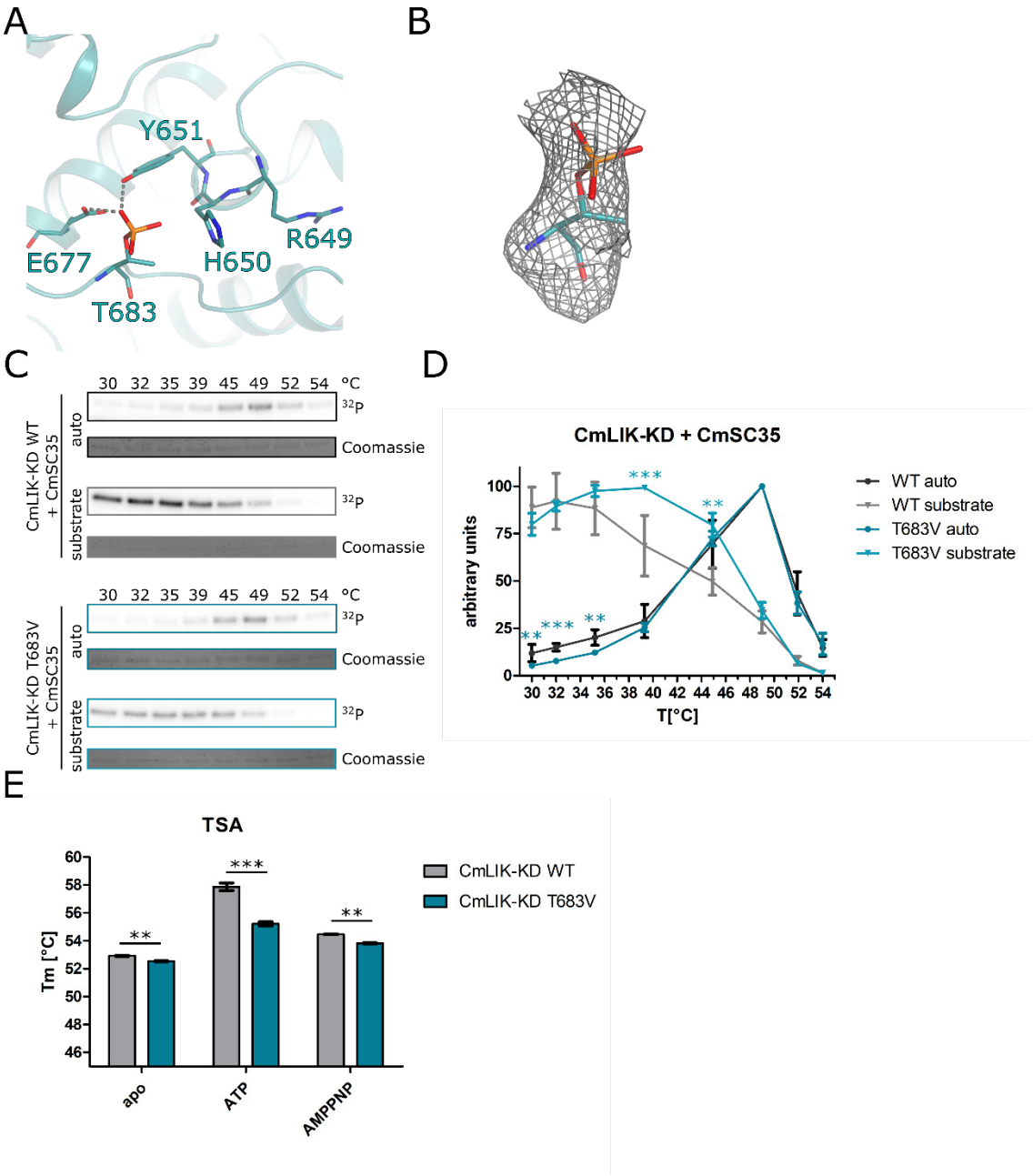

Figure 4-9 Auto phosphorylation of CmLIK-KD T683 exhibits an auto inhibitory effect. A Zoom in on phospho-threonine (TPO) 683 of chain B of the CmLIK-KD structure from Figure 4-8, protein depicted as cartoon and interacting residues depicted as sticks. H-bond distance cut-off = 3.2 Å. **B** Polder electron density map of chain B TPO 683 contoured at σ = 3.0. **C** Representative SDS-PAGE gels of *in vitro* kinase assays of purified CmLIK-KD WT and T683V mutant with physiological CmSC35 substrate. Respective kinase is indicated on the left and sample temperature is indicated on top. Protein loading detected by Coomassie staining and phosphorylation detected by autoradiography are shown for the kinase (auto) and substrate. **D** Quantification of auto and substrate phosphorylation from the *in vitro* kinase assays in C. Radioactive signal was normalized to highest signal in assay. Shown are mean and standard deviation. For the WT the mean of all experiments was taken. Respective kinase is indicated in the legend on the right. Statistically significant differences between WT and T683V variant determined by unpaired Welch t-test are indicated as asterisks in the color corresponding to auto or substrate phosphorylation (*: $p < 0.05$, **: $p < 0.01$, ***: $p < 0.001$). WT n = 8 and T683V n = 3. **E** Melting temperature of CmLIK-KD WT and T683V mutant with or without indicated nucleotide in assay buffer determined by

thermal shift assay. Shown are mean and standard deviation. Respective kinase is indicated in the legend on the right. Statistically significant differences determined by unpaired Welch t-test are indicated as asterisks (*: $p < 0.05$, **: $p < 0.01$, ***: $p < 0.001$). n = 3.

4.2.4 A salt bridge facilitates CmLIK-KD activity at higher temperatures.

In the first CmLIK-KD structure a salt bridge between D690 (loop between αF and αG helix) and R649 of the activation segment could be observed (Figure 1-3 B) and an exchange mutant D690S, replacing the aspartate with a serine present in hCLK1, exhibited reduced activity at high temperatures in assays with a synthetic GST-RS substrate (Haltenhof, 2020). We wanted to further characterize this mutant and its activity on the physiological substrate. The D690S mutant exhibited significantly elevated auto phosphorylation between 32°C and 45°C and significantly decreased auto phosphorylation at 49°C. CmSC35 phosphorylation was significantly reduced at 45°C and nearly abolished at 49°C and higher temperatures in the *in vitro* kinase assays (Figure 4-10 A, B). This proved that the salt bridge is essential for CmLIK activity at and above 45°C, the physiological habitat temperature of *C. merolae* (Luca et al., 1978). Further we subjected the D690S exchange mutant to a thermal shift assay. The mutant T_m was 4.5°C lower than the WT in the apo state and 4.0°C lower in the presence of AMPPNP (Figure 4-10 C). In contrast the difference between D690S and WT was just -1.4°C in the presence of ATP. So, we observed a phosphorylation dependent stabilization of 4.0°C in the WT and 7.1°C in the mutant, yielding a $\Delta\Delta T_m$ of 3.1°C. This surprising phosphorylation dependent restoration of protein stability might be due to the presence of a new phosphorylation site at D690S, the phosphoserine mimicking the aspartate and restoring the salt bridge. Indeed, we could observe phosphorylation at D690S after incubation for 30 min in the presence of ATP and CmSC35 at 32°C and even more so at 45°C and 49°C via LC-ESI-MS/MS after in-gel digest with elastase (Figure 4-10 D). Considering that not only this phosphorylation site is present in hCLK1 (S384), but also the interacting arginine (R343), auto phosphorylation and thus stabilization of the activation segment might also play a role in hCLK1 function.

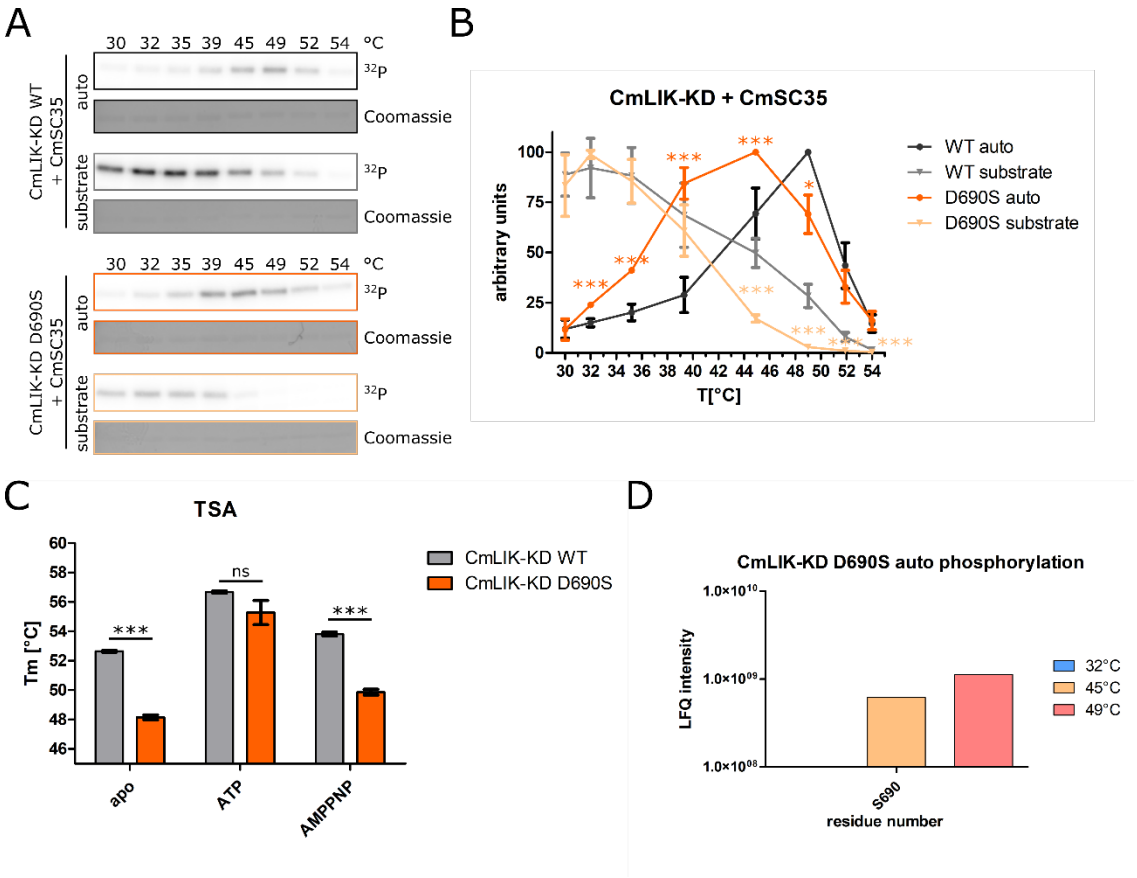

Figure 4-10 Abolishing the salt bridge at D690 impairs CmLIK-KD activity at high temperatures. **A** Representative SDS-PAGE gels of *in vitro* kinase assays of purified CmLIK-KD WT and D690S mutant with physiological CmSC35 substrate. Respective kinase is indicated on the left and sample temperature is indicated on top. Protein loading detected by Coomassie staining and phosphorylation detected by autoradiography are shown for the kinase (auto) and substrate. **B** Quantification of auto and substrate phosphorylation from the *in vitro* kinase assays in A. Radioactive signal was normalized to highest signal in assay. Shown are mean and standard deviation. For the WT the mean of all experiments was taken. Respective kinase is indicated in the legend on the right. Respective kinase is indicated in the legend on the right. Statistically significant differences between WT and D690S variant determined by unpaired Welch t-test are indicated as asterisks in the color corresponding to auto or substrate phosphorylation (*: $p < 0.05$, **: $p < 0.01$, ***: $p < 0.001$). WT n = 8 and D690S n = 3. **C** Melting temperature of CmLIK-KD WT and D690S mutant with or without indicated nucleotide in assay buffer determined by thermal shift assay. Shown are mean and standard deviation. Respective kinase is indicated in the legend on the right. Statistically significant differences determined by unpaired Welch t-test are indicated as asterisks ($p < 0.05$). n = 3. **D** Label-free quantification (LFQ) of intensities of peptides containing phosphorylated residue S 690. CmLIK-KD D690S was incubated with CmSC35 in the presence of ATP at different temperatures for 30 min, protein separated via SDS-PAGE, in gel digested with elastase, peptides extracted and subjected to LC-ESI-MS/MS. Data was analyzed and spectra quantified using FragPipe LFQ-phospho workflow.

4.2.5 Insertion of the CLK β-hairpin destabilizes CmLIK-KD.

Apart from the afore mentioned salt bridge and the MAPK-like insertion in the C-lobe one major difference evident between hCLK1-KD and CmLIK-KD is the β-hairpin located

upstream of the activation segment, connecting it with the loop harboring the catalytically active aspartate (Figure 1-3 A). This structural motif is conserved in animal CLKs (Figure 4-2 A, Figure 4-3 A) and also plant CLK homologs (Figure 4-17 A, Figure 4-18 A) but absent in CmLIK. To investigate the potential effect of the β-hairpin we cloned and purified a CmLIK-KD hairpin mutant where residues 610-624 were replaced with residues 297-319 of mCLK1. First, we attempted to crystallize apo CmLIK-KD hairpin mutant to see if the inserted residues adopted the β-hairpin fold and obtained small envelope-shaped crystals of the spacegroup $P2_12_12_1$ which yielded a dataset with the resolution of 2.50 Å from measurement at BESSY-II, beamline 14-2. A larger envelope-shaped crystal of the same spacegroup was measured at PETRA-III, beamline P11. The dataset yielded unit cell parameters closely resembling those of the first CmLIK-KD WT structure (Table 3) and a structure at 1.77 Å resolution, with one copy of CmLIK-KD hairpin in the asymmetric unit and no visible density for bound nucleotide, as well as the sidechain of L555 blocking the nucleotide binding pocket (Figure 4-11 A). Overall, the structure of CmLIK-KD did not change, and no significant shift was observed upon hairpin insertion, suggesting that the protein remained intact and functional. The inserted residues adopted the β-hairpin fold similar to hCLK1 (Figure 4-11 B) showing that mutant generation was successful. In addition, we attempted co-crystallization of the CmLIK-KD hairpin mutant with AMPPNP, a non-hydrolysable ATP analogue, to investigate nucleotide binding. Refining the previous apo conditions and utilizing seeding we obtained bipyramidal crystals. Two crystals yielded datasets with 2.10 Å, 2.17 Å resolution respectively at BESSY-II, beamline 14-2 and one crystal yielded a dataset with 1.86 Å resolution at PETRA-III, beamline P11. All three structures did not differ from the obtained apo structure, no density for bound nucleotide could be observed and the sidechain of L555 blocked the nucleotide binding pocket (data not shown). In *in vitro* kinase assays CmLIK-KD hairpin mutant exhibited significantly reduced CmSC35 phosphorylation at 35°C and higher temperatures (Figure 4-11 C, D). While auto phosphorylation was significantly increased at 30°C up to 45°C compared to the WT, it was nearly abolished at 49°C and higher temperatures. Thermal shift assay revealed a decreased T_m of 47.7°C for the apo mutant, 4.9°C lower than the WT (Figure 4-11 E). The presence of ATP increased the mutant T_m to 51.4°C in a fashion similar to the WT with a

$\Delta\Delta T_m$ of 0.1°C. These results suggest that the shorter loop in CmLIK is important for its stability as well as activity at higher temperatures.

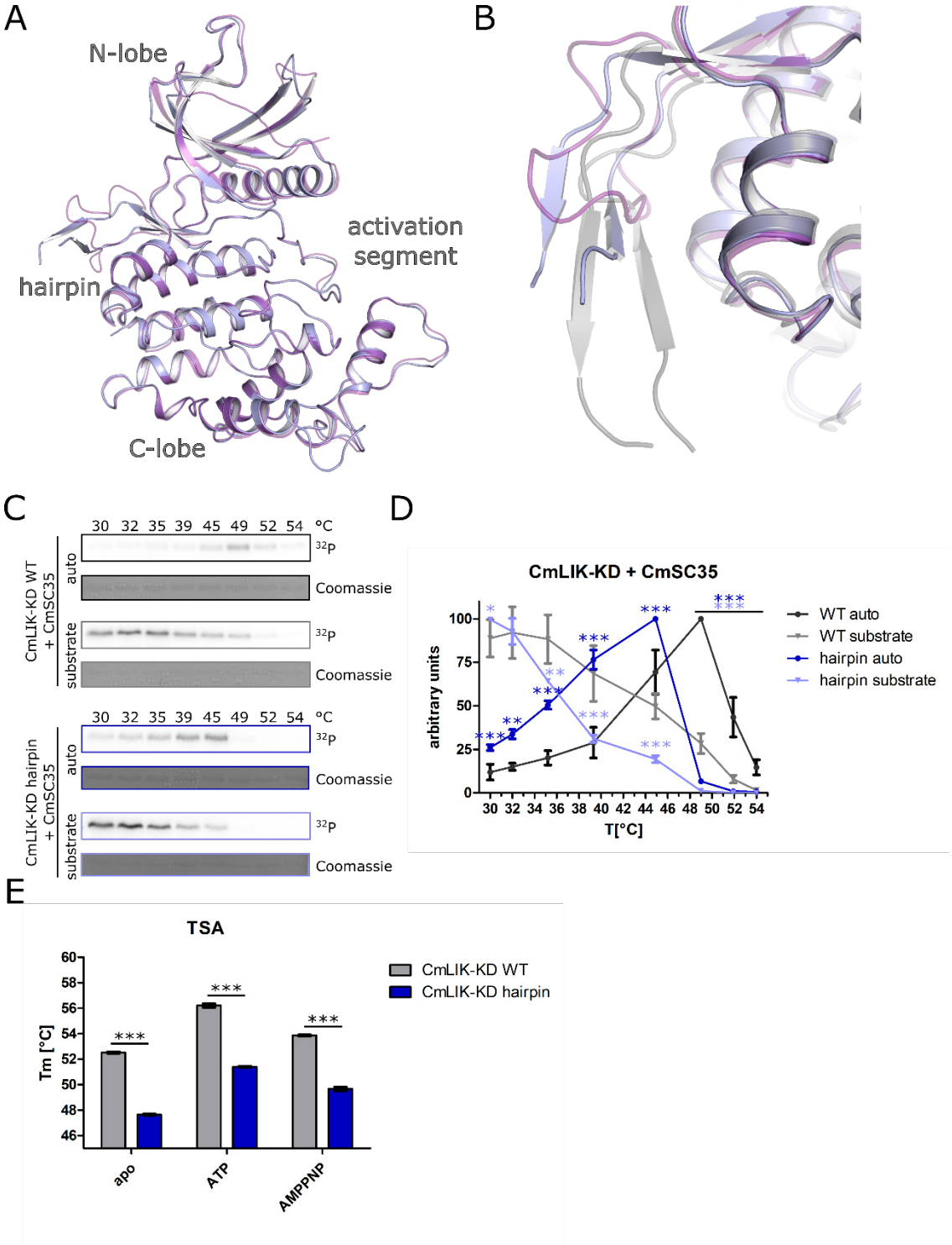

Figure 4-11 Insertion of hairpin lowers CmLIK-KD activity at higher temperatures. **A** Superimposition of CmLIK-KD hairpin mutant structure at 1.77 Å (light blue) with CmLIK-KD WT (deeppurple) represented as cartoon. Domain elements indicated. **B** Zoom on hairpin from A. Additionally, structure of hCLK1 (6TW2, grey) superimposed on CmLIK-KD. **C** Representative SDS-PAGE gels of *in vitro* kinase assays of purified CmLIK-KD WT and hairpin mutant with physiological CmSC35 substrate. Respective kinase is indicated on the left and sample temperature is indicated

on top. Protein loading detected by Coomassie staining and phosphorylation detected by autoradiography are shown for the kinase (auto) and substrate. **D** Quantification of auto and substrate phosphorylation from the *in vitro* kinase assays in C. Radioactive signal was normalized to highest signal in assay. Shown are mean and standard deviation. For the WT the mean of all experiments was taken. Respective kinase is indicated in the legend on the right. Respective kinase is indicated in the legend on the right. Statistically significant differences between WT and hairpin variant determined by unpaired Welch t-test are indicated as asterisks in the color corresponding to auto or substrate phosphorylation (*: $p < 0.05$, **: $p < 0.01$, ***: $p < 0.001$). WT n = 8 and hairpin n = 3. **E** Melting temperature of CmLIK-KD WT and hairpin mutant with or without indicated nucleotide in assay buffer determined by thermal shift assay. Shown are mean and standard deviation. Respective kinase is indicated in the legend on the right. Statistically significant differences determined by unpaired Welch t-test are indicated as asterisks (*: $p < 0.05$, **: $p < 0.01$, ***: $p < 0.001$). n = 3.

4.2.6 Quantification of phosphorylations by CmLIK-KD via intact mass LC-ESI-MS.

Radioactive *in vitro* kinase assays are limited in information as only total amount of phosphorylation is quantified. We wanted to investigate how many sites in CmSC35 and CmLIK-KD are phosphorylated per molecule in dependence of kinase variant, temperature and time. To accomplish this, we incubated kinase and substrate in the presence of ATP at different temperatures, took samples at different timepoints, stopped the reaction by dilution in TA33 and analyzed the samples via intact mass LC-ESI-MS. All samples yielded distinct kinase and substrate peaks. Phospho-species peaks could be distinguished in deconvoluted spectra by 80 Da difference per incorporated phosphate. In CmLIK-KD WT up to 11 auto phosphorylations per molecule (P/m) were observed at 49°C (Figure 4-12 A). While the main population showed 3 P/m at 2 and 5 min, this shifted steadily towards 4.5 P/m over the course of 30 min. In accordance with previously discussed observations the D690S mutant main population showed 4 P/m at 2 min at 49°C, one more than the WT, probably located at S690 (Figure 4-12 B). We could observe up to 13 P/m and over the course of 30 min the main population shifted to 6 P/m. In contrast to the other two mutants, the hairpin mutant showed a main population with 3 P/m at 49°C throughout the whole time course (Figure 4-12 C). The P/m were distributed in a sharp peak, only broadening slightly towards 6 or more P/m. The maximum number of P/m observed was 10. In Figure 4-12 D the final distribution of P/m after 30 min for all three CmLIK variants is shown. Here it becomes evident that the almost Gaussian distribution of P/m centered at 4.5 sites in the WT is shifted by one phosphorylation in the D690S mutant and decreased to a sharp peak around 3 sites in the hairpin mutant.

For CmSC35 we observed a Gaussian distribution of P/m centered around 1.5 P/m after incubation with CmLIK-KD WT for 5 min at 32°C (Figure 4-12 E). This distribution shifted gradually over the time course, the center being 4.5 P/m after 30 min and no unphosphorylated CmSC35 was left. A maximum of 10 P/m could be observed. Incubation with the D690S mutant led to a slower increase in phosphorylated populations and only to an almost Gaussian distribution centered around 2.5 P/m after 20 min (Figure 4-12 F). This distribution changed barely between 20 and 30 min and in contrast to the WT unphosphorylated CmSC35 could still be detected. The hairpin mutant exhibited a similarly slow increase in phosphorylations as the D690S mutant but phosphorylated CmSC35 to a lesser extent with the main populations having 1.5 P/m after 30 min (Figure 4-12 G). In Figure 4-12 H the CmSC35 P/m distributions after 30 min at 32°C for all three CmLIK-KD variants are shown. It is evident that both mutants are unable to fully phosphorylate CmSC35 compared to the WT. This activity impairment in the mutants could also be characterized by looking at the decrease of unphosphorylated CmSC35 over the time course. We plotted the relative abundance of unphosphorylated CmSC35 over the time of incubation with CmLIK-KD WT at the three temperatures (Figure 4-13 A) and calculated the catalytic rates via nonlinear regression with a one phase decay (Table 1). In agreement with our *in vitro* kinase assays the catalytic rate decreased with increasing temperature but was still quantifiable at 49°C with 1.01 min^{-1}. For the D690S mutant a catalytic rate could only be calculated at 32°C (Figure 4-13 B), but for the hairpin mutant 45°C also yielded an analyzable curve (Figure 4-13 C). Comparison of all variants at 32°C (Figure 4-13 D and Table 1) revealed a roughly halved catalytic rate for D690S mutant and 5 times lower catalytic rate for hairpin mutant compared to the WT. These results complement our previous insights, and show that both mutants not only affect the general catalytic rate of CmLIK and total CmSC35 phosphorylation, but also the maximum number of sites that are phosphorylated on a single CmSC35 molecule. Differences in activity between mutants could be revealed even at 32°C where CmLIK activity is highest, and no differences could be observed in radioactive *in vitro* kinase assays. While the shift in total auto phosphorylation activity appeared very similar between D690S and hairpin mutant in the radioactive assays (Figure 4-10 B, Figure 4-11 D) the intact mass analysis revealed contrasting effects in

auto phosphorylation site usage, hairpin lowering and D690S increasing the number of phosphorylated sites on a single CmLIK molecule.

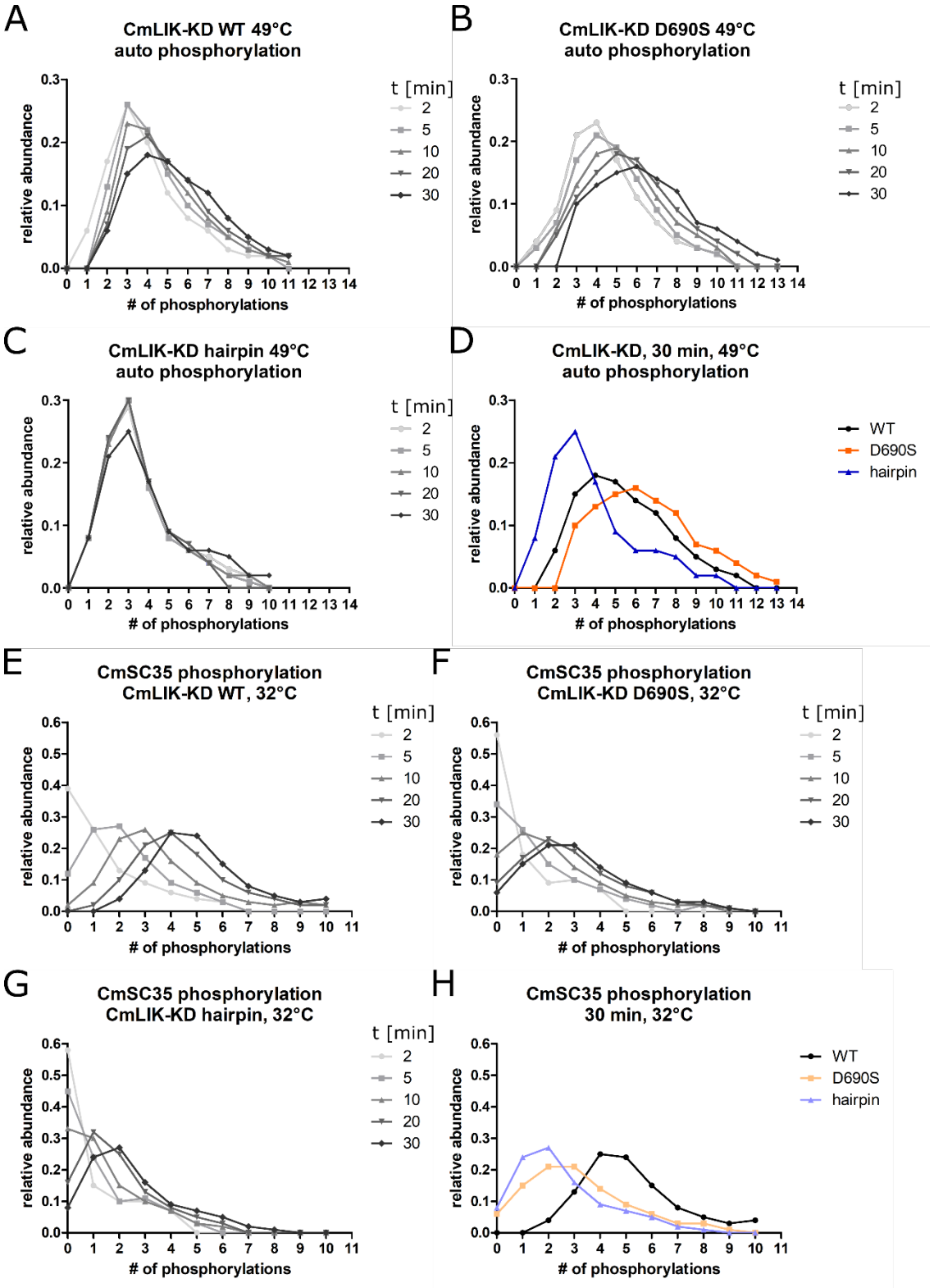

Figure 4-12 Investigation of CmLIK-KD auto and substrate phosphorylation via intact mass LC-ESI-MS. CmLIK-KD and CmSC35 incubated in the presence of ATP at different temperatures. Samples

taken at indicated timepoints, reaction stopped by TA33 addition and subjected to intact mass LC-ESI-MS. Spectra were deconvoluted and peaks quantified with UniDec software suite. Peak intensities were normalized to the highest peak and abundance of phosphorylated species calculated relative to the sum of all normalized peak intensities. **A** Auto phosphorylation of CmLIK-KD WT at 49°C at indicated timepoints. **B** As A for CmLIK-KD D690S. **C** As A for CmLIK-KD hairpin. **D** Auto phosphorylation of indicated CmLIK-KD variants after 30 min at 49°C. **E** Phosphorylation of CmSC35 by CmLIK-KD WT at 32°C at indicated timepoints. **F** As E with CmLIK-KD D690S. **G** As E with CmLIK-KD hairpin. **H** Phosphorylation of CmSC35 by indicated CmLIK-KD variants after 30 min at 32°C.

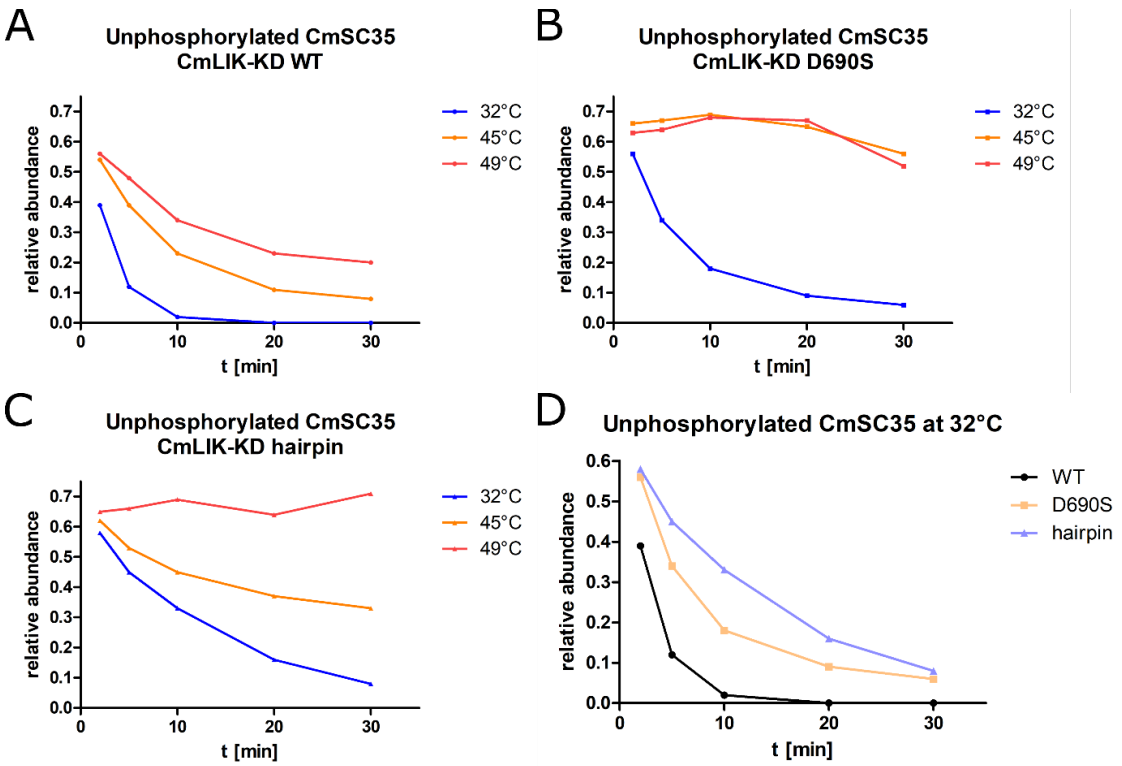

Figure 4-13 CmLIK-KD mutants exhibit impaired decrease of unphosphorylated CmSC35. CmLIK-KD and CmSC35 incubated in the presence of ATP at different temperatures. Samples taken at indicated timepoints, reaction stopped by TA33 addition and subjected to intact mass LC-ESI-MS. Spectra were deconvoluted and peaks quantified with UniDec software suite. Peak intensities were normalized to the highest peak and abundance of phosphorylated species calculated relative to the sum of all normalized peak intensities. Only relative abundance of unphosphorylated CmSC35 is shown. A In presence of CmLIK-KD WT at indicated temperatures. **B** As A for CmLIK-KD D690S. **C** As A for CmLIK-KD hairpin. **D** At 32°C in presence of indicated CmLIK-KD variants.

Table 1 Catalytic rates (K) with standard deviation (SD) of CmSC35 phosphorylation

	WT		D690S		hairpin	
T [°C]	K [min^{-1}]	SD [min^{-1}]	K [min^{-1}]	SD [min^{-1}]	K [min^{-1}]	SD [min^{-1}]
32	0.392	0.006	0.187	0.012	0.074	0.008
45	0.132	0.003	-	-	0.103	0.011
49	0.101	0.016	-	-	-	-

4.2.7 Characterization of phosphorylation sites in CmLIK-KD and CmSC35.

After analysis of how many phosphorylation sites per molecule were used in CmSC35 and CmLIK-KD we wanted to elucidate which exact sites were phosphorylated. For this purpose, we used the 30 min timepoint samples from the above-mentioned assay, separated the proteins via SDS-PAGE, excised the bands, digested one half with trypsin and the other half with elastase and analyzed the extracted peptides via LC-ESI-MS/MS. The elastase digested samples yielded no additional phosphorylated sites in CmLIK-KD that were not detected in the trypsin samples, except for the D690S mutant where phosphorylated S690 could be detected (Figure 4-10 D). The trypsin digested samples yielded sequence coverages of 63 – 77 % (Table 4). Between all sampled temperatures we found 20 sites that were phosphorylated in CmLIK-KD WT (Figure 4-14 A). While in most sites the intensity difference between 32°C and 49°C was less than one order of magnitude, six residues showed more drastic changes. Phosphorylation of Y468 increased by almost two orders of magnitude between both temperatures. Phosphorylation of T490 and T599 occurred only at 49°C and of S647 and T648 only at 45°C. S770 was phosphorylated at 45°C and 49°C. These pronounced changes suggest a role in auto inhibitory phosphorylation. While no clear role for Y468 and T490 in the N-lobe can be proposed, T599 is in the catalytic center of CmLIK-KD and might interfere directly with the catalyzed reaction. The corresponding residues to S647 and T648 are also phosphorylated in hCLK1, and molecular docking data suggests that their phosphorylation interferes with substrate binding, exerting an inhibitory effect (Haltenhof et al., 2020). S770 is located in the loop after the αH helix, which buries the αG helix and the binding grooved formed by the MAPK-like insertion. The MAPK-like insertion has been shown to be involved in substrate interaction and processivity in

SRPKs (Ngo et al., 2008; Long et al., 2019), so this phosphorylation might influence substrate binding. All observed CmLIK-KD phosphorylation sites were mapped onto the structure we obtained (Figure 4-15).

Consistent with the *in vitro* kinase assays CmLIK-KD auto phosphorylation in general (Figure 6-5 C) was higher than WT in both mutants at 32°C (Figure 6-5 A) and 45°C (Figure 4-14 B) but lower at 49°C (Figure 6-5 B). At 45°C differences in auto phosphorylation between the variants were the most pronounced in the *in vitro* kinase assays. Here we observed an increase of phosphorylation of residues Y468 and S770 by one order of magnitude in CmLIK-KD D690S (Figure 4-14 B). Even more pronounced was the difference for S647 and T648, the residues that have a suggested auto inhibitory effect also in hCLK1, where phosphorylation increased by three orders of magnitude in the D690S mutant. This suggests that impaired CmSC35 phosphorylation by CmLIK-KD D690S might not only be caused by lack of the salt bridge stabilization but also increased inhibitory auto phosphorylation. The hairpin mutant appears to have lost the ability to phosphorylate S647, T648 and S770. Phosphorylation of T620 (T627 in the hairpin mutant) was increased by one order of magnitude compared to the other variants. Notably this residue is shifted in the sequence due to the hairpin insertion. Despite the drastic change in amount of phosphorylations per molecule in the hairpin mutant (Figure 4-12 D) the site usage shows little difference to the WT apart from the three aforementioned residues.

At 32°C we could identify 6 phosphorylation sites for CmSC35 in trypsin digested samples (Figure 4-16) while obtaining a sequence coverage of 55.86 % in all samples (Table 5). While for most sites no differences between the variants could be observed, usage of the phosphorylation site T147 was slightly impaired in both mutants. In 32°C samples digested with elastase the sequence coverage was increased to 62-88 % (Table 5) but only 4 phosphorylation sites could be detected. This was probably caused by the loss of overall intensity due to the nonspecific cleavage by elastase and less efficient ionization of phosphorylated peptides in the positive ion mode during ESI. In addition to S60 and T147, which were also detected in the trypsin samples, we could identify S36 as a phosphorylation site in all samples and S37 in both mutant samples (Figure 6-6 A). In sum we could identify 8 phosphorylation sites in CmSC35, but this list is likely not complete due to relatively low sequence coverage. Especially the C-terminal RS repeats (residue

196-216), which are the most likely phosphorylation sites, could not be detected due to their repetitive nature interfering with obtaining detectable peptides. Also, intact mass LC-ESI-MS detected up to 10 phosphorylations in CmSC35 (Figure 4-12 H).

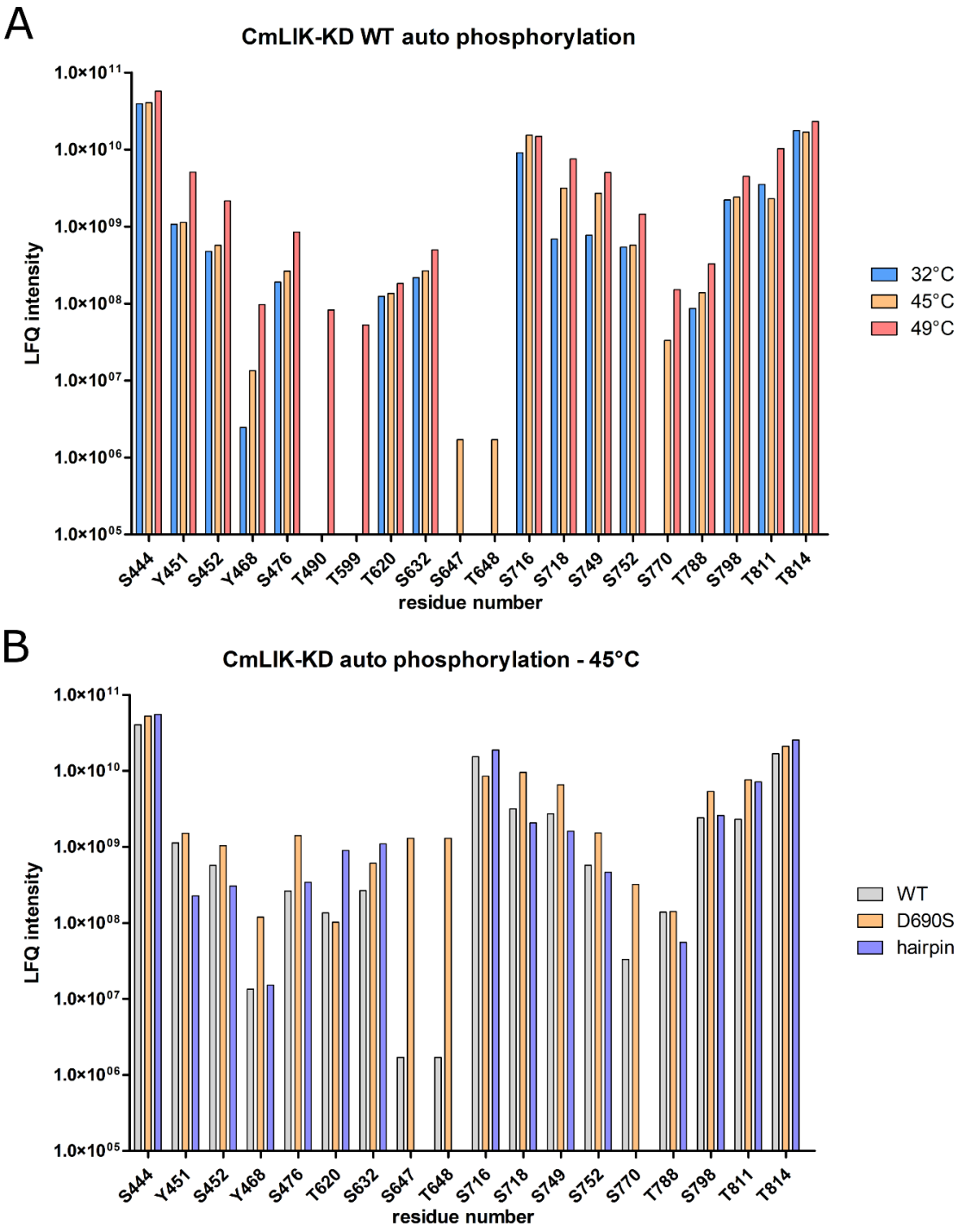

Figure 4-14 Elucidation of phosphorylated residues in CmLIK-KD variants and CmSC35 by LC-ESI-MS/MS. A Label-free quantification (LFQ) of phosphopeptide intensities of CmLIK-KD WT. CmLIK-KD WT was incubated with CmSC35 in the presence of ATP at 32°C, 45°C and 49°C for 30 min, proteins separated via SDS-PAGE, in gel digested with trypsin, peptides extracted and subjected to LC-ESI-MS/MS. Data was analyzed and spectra quantified using the FragPipe LFQ-phospho workflow. Intensities are displayed on a logarithmic scale. **B** Experimental setup as in A, but

incubated at 45°C and also CmLIK-KD D690S and hairpin mutant were included. Residue numbers correspond to CmLIK WT.

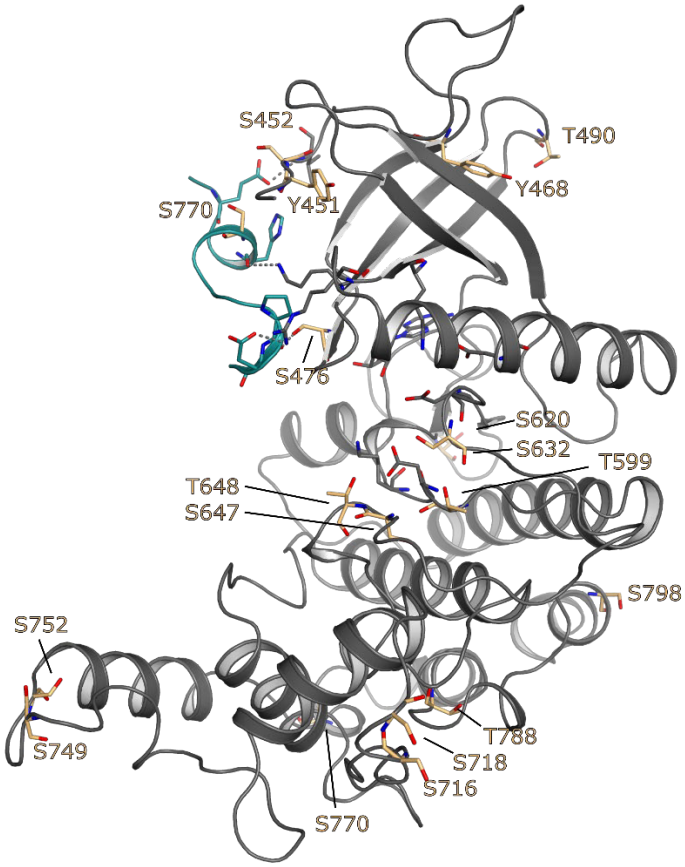

Figure 4-15 Phosphorylation site mapping onto CmLIK-KD WT structure. CmLIK-KD WT structure at 2.69 Å resolution. Protein depicted as cartoon, chain A colored in grey, chain B in deep teal. For chain B only regions interacting with chain A are shown. Nucleotide, interacting residues and phosphorylation sites observed by LC-ESI-MS/MS analysis depicted as sticks. H-bonds (distance cut-off = 3.2 Å) are depicted as dashed lines in grey. Phosphorylation sites are colored in light orange and labeled.

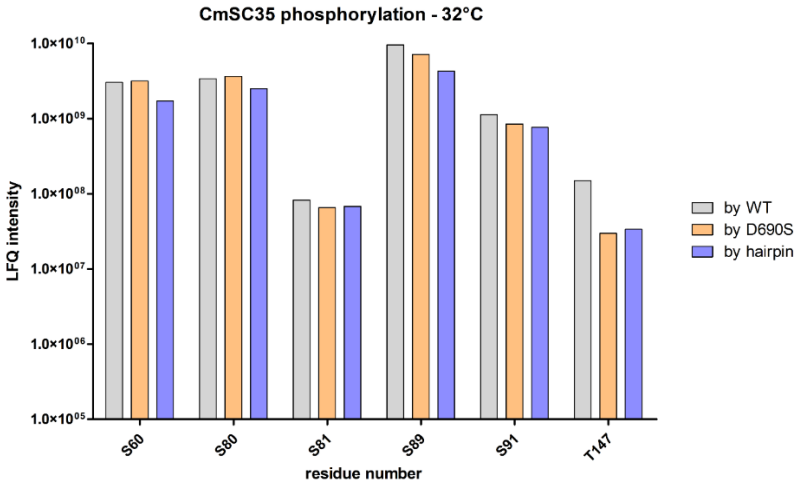

Figure 4-16 Elucidation of phosphorylated residues in CmSC35 by LC-ESI-MS/MS. Label-free quantification (LFQ) of phosphopeptide intensities of CmSC35. Indicated CmLIK-KD variants were

incubated with CmSC35 in the presence of ATP at 32°C for 30 min, proteins separated via SDS-PAGE, in gel digested with trypsin, peptides extracted and subjected to LC-ESI-MS/MS. Data was analyzed and spectra quantified using the FragPipe LFQ-phospho workflow. Intensies are displayed on a logarithmic scale.

4.3 *A. thaliana* – different kinases catering to different needs

Since plants can neither regulate their temperature nor move to a habitat with a stable temperature they have to adapt to a broad range of temperatures. As such it was not a surprise that there are three CLK homologs – AFCs – present in *A. thaliana* that exhibit each distinct temperature activity profiles (Figure 1-4). These closely related proteins with high similarity but distinct activities are superb candidates to elucidate structural elements that govern the active temperature range.

4.3.1 Stabilization of the activation segment via an H-bond network mediates AtAFC3 activity at high temperatures.

With this aim in mind, we compared AlphaFold predictions of the kinase domains of AtAFC1 and AtAFC3, the kinases with the most contrasting temperature activity profiles, available in the AlphaFold Protein Structure Database (Figure 4-17 A). Both proteins adopted a typical kinase fold and did not differ in any structural elements, disregarding a different orientation on the flexible loop end of the β-hairpin upstream of the activation segment, yielding a r.m.s.d. of 1.28 Å and a TM-score of 0.92 while the sequences were 68 % identical. Closer inspection revealed two clusters of differing interactions in the activation segment. In AtAFC3 Q254 of the activation segment forms H-bonds with Y258 and S260, also of the activation segment, and C273 and S277 of the αF helix (Figure 4-17 B). These interactions might stabilize the activation segment in general and especially the loop containing R256 and H257. The corresponding residues in hCLK1 (R342 and H343) were shown to be essential for temperature dependent activity (Haltenhof et al., 2020). In contrast in AtAFC1 the corresponding residue S301 forms just one H-bond with T239 of the catalytic loop. The second cluster is centered around an H-bond between T290 and Q294 in AtAFC1, which pulls the activation loop inward towards the catalytic center and allows H296 to interact with the backbone of F291, both interactions stabilizing this region. H-bonds between the backbone of Q294 and H296, and D295 and N297 further aid in stabilization. These interactions are not present in

AtAFC3, since the corresponding threonine is replaced by valine (AtAFC3 V243) and glutamine by arginine (AtAFC3 R247) (Figure 4-17 C). To investigate the more defined interaction cluster around AtAFC3 Q254 we cloned and purified a Q254A exchange mutant of AtAFC3. In *in vitro* kinase assays with a synthetic GST-RS substrate we observed elevated auto phosphorylation of AtAFC3 Q254A between 12°C and 24°C and significantly decreased auto phosphorylation at 32°C and above. Auto phosphorylation at 40°C was completely abolished. Substrate phosphorylation was significantly impaired at 36°C and almost completely abolished at 40°C (Figure 4-17 D, E). These results suggest that the activation segment stabilization by Q254 in AtAFC3 is essential for its activity at high temperatures. However, the loss of these interactions was not sufficient to increase its activity at temperatures below 24°C and activity at 32°C was not impaired. For the complete shift of the temperature activity profile towards AtAFC1 the additional exchange of the second interaction cluster and/or creating an interaction between residue 254 and T195 might be needed. In order to further validate the interactions of AtAFC3 Q254 we cloned AtAFC3-KD WT into pETM-11 vector, expressed the protein in *E. coli* BL21(DE3) pRare and purified His-AtAFC3-KD WT. Initial crystallization trials using the Classics Suite (Qiagen) and Index (Hampton research) screens yielded only precipitate or clear drops and no crystals.

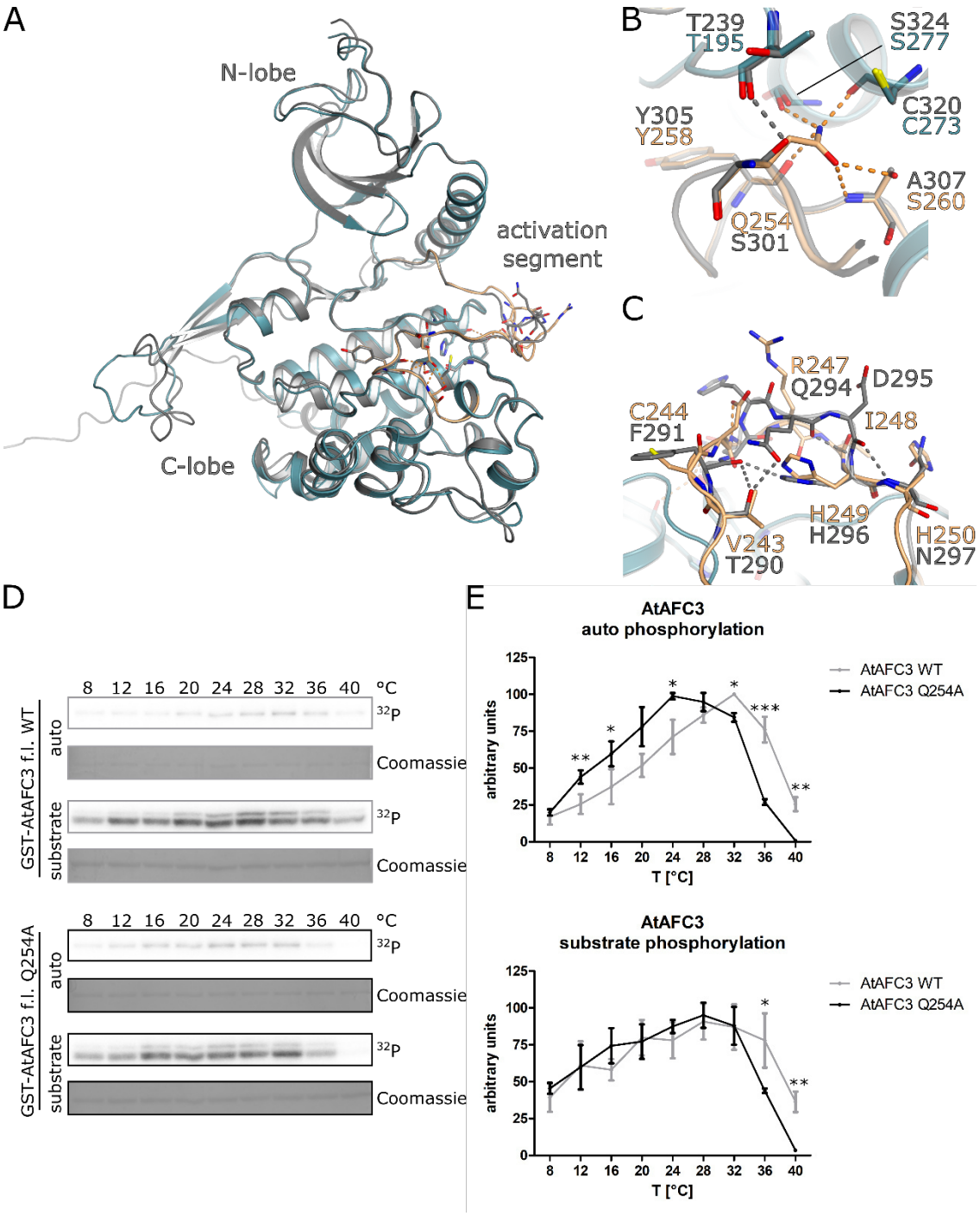

Figure 4-17 An H-bond network around Q254 is essential for AtAFC3 activity at high temperatures. **A** Superimposition of AlphaFold predictions of AtAFC3-KD (P51568, teal) and AtAFC1-KD (P51566, grey) represented as cartoon. AtAFC3 activation segment is colored in light orange. Domain elements indicated. **B** Zoom on H-bond network around AtAFC3 Q254 from A. Q254, interacting residues and corresponding residues from AtAFC1 are depicted as sticks. H-bonds (distance cut-off = 3.2 Å) of AtAFC3 shown in orange and of AtAFC1 in grey. **C** Zoom on H-bond network around AtAFC3 N246 from A. Depiction as in B. **D** Representative SDS-PAGE gels of *in vitro* kinase assays of purified GST-AtAFC3 f.l. WT and Q254A mutant with synthetic GST-RS substrate. Respective kinase is indicated on the left and sample temperature is indicated on top. Protein loading detected by Coomassie staining and phosphorylation detected by autoradiography are shown for the kinase (auto) and substrate. **E** Quantification of auto and substrate phosphorylation from the *in vitro* kinase assays in D. Radioactive signal was normalized

to highest signal in assay. Shown are mean and standard deviation. Respective kinase is indicated in the legend on the right. Statistically significant differences determined by unpaired Welch t-test are indicated as asterisks (*: $p < 0.05$, **: $p < 0.01$, ***: $p < 0.001$). WT n = 4 and Q254A n = 3.

4.3.2 AlphaFold predictions suggest copper-dependent activity of AtAFC2.

Similarly to our comparison between AtAFC1 and AtAFC3 we compared AlphaFold predictions of AtAFC1 and AtAFC2 (Figure 4-18 A). As for AtAFC3, the overall fold did not differ between both proteins, yielding a r.m.s.d. of 0.86 Å and a TM-score of 0.91 while the sequences were 76 % identical. While we did not observe outstanding differing interactions in the activation segment, we could observe a potential disulfide bridge between C210 of the αE helix and C159 located in a loop directly downstream of the αC helix (Figure 4-18 B). This bond would connect the N-lobe with the C-lobe and could influence their orientation towards each other or the dynamic of their shifts and thus AtAFC2 catalytic activity, maybe explaining its relatively broad temperature range of activity. Furthermore, in close proximity to the catalytic center and activation segment we observed an arrangement of one histidine and three methionine residues, that resembles a motif commonly found in copper coordination centers (Rubino and Franz, 2012). Precisely the site comprises M145 of the αC helix, M214 of the αE helix and M219 and H221 of the catalytic loop (Figure 4-18 C). This kind of site composition has been reported for example in the Cu(I)-binding site of CopC (Arnesano et al., 2003). Due to the involvement of the histidine at the catalytic center this could suggest a temperature independent regulation of AtAFC2 and rather copper dependent kinase activity. Aiming to validate the disulfide bridge in AtAFC2 we cloned a C210S exchange mutant. Expressed in *E. coli* BL21(DE3) pRare and subjected to on-bead *in vitro* kinase assays with synthetic GST-RS substrate the AtAFC2 C210S mutant showed a temperature activity profile similar to the WT (Figure 6-7). Considering that BL21(DE3) pRare is not a suitable strain for expression of proteins with disulfide bridges and that the reaction buffer contained 5 mM DTT this result was not surprising. We re-cloned AtAFC2-KD WT and C210S into pETM-11 vector and expressed both proteins in *E. coli* RosettaGami2. During purification of His-AtAFC2-KD WT the protein precipitated after affinity chromatography as well as after SEC in standard buffer conditions. This prevented us from further exploring this approach.

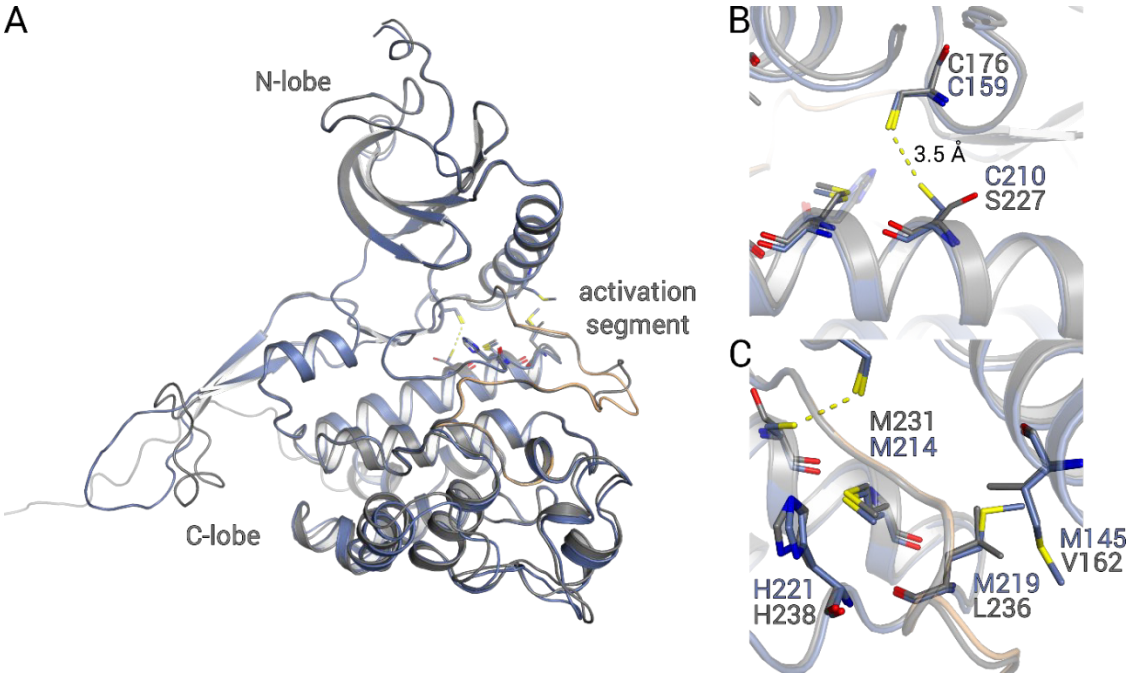

Figure 4-18 AtAFC2 structure prediction hints at activity regulation via a disulfide bridge and copper binding. A Superimposition of AlphaFold predictions of AtAFC2-KD (P51567, blue) and AtAFC1-KD (P51566, grey) represented as cartoon. AtAFC2 activation segment is colored in light orange. Domain elements indicated. **B** Zoom on potential disulfide bridge between AtAFC2 Cys 159 and Cys 210 from A. Both residues and corresponding residues from AtAFC1 are depicted as sticks. Distance between both Cys shown in yellow. **C** Zoom on AtAFC2 residues constituting a potential copper binding motif from A. Potential coordinating residues and corresponding residues from AtAFC1 are depicted as sticks.

4.3.3 AtAFCs regulate thermoresponsive hypocotyl growth in an auxin-dependent way via *PIF4* expression.

To characterize AtAFC1-3 function further our cooperation partner at the University of Würzburg, Dr. Daniel Maag, generated AtAFC triple knock-out (TKO) plant lines via CRISPR-Cas9 and cultured these plants at 17°C and 28°C. In comparison to the WT/Col-0 they observed reduced thermoresponsive hypocotyl growth. This phenotype could also be induced with the CLK inhibitor TG003. Interestingly the phenotype of the TKO plants could be rescued by applying 1 µM picloram, a synthetic analogue to the phytohormone auxin. Knock-out of *PIF4*, a transcription factor regulating auxin levels (Franklin et al., 2011), also produced a phenotype similar to the AtAFC TKOs. In an effort to investigate if AtAFCs regulate thermoresponsive hypocotyl growth in a PIF4 and auxin dependent manner we carried out gene expression analysis with RNA samples from the AtAFC TKO and WT plants provided by our cooperation partner. While the Col-0 samples showed

elevated expression of *PIF4* after 8 h at 28°C and even more so after 24 h at 28°C, AtAFC TKO showed significantly reduced *PIF4* expression after 24 h at 28°C, the level being similar to the 17°C samples (Figure 4-19 A). In addition, expression of *YUC8*, another *PIF4* target (Stavang et al., 2009), was also significantly reduced in AtAFC TKO compared to elevated levels at 28°C in Col-0 (Figure 4-19 B). The elevated expression of *SAUR19* and *SAUR20*, both targets of auxin and drivers of temperature dependent hypocotyl growth (Franklin et al., 2011), at 28°C was significantly impaired in AtAFC TKO (Figure 4-19 C, D). These results suggest that AtAFCs regulate thermoresponsive hypocotyl growth in an auxin-dependent way via modulation of *PIF4* expression.

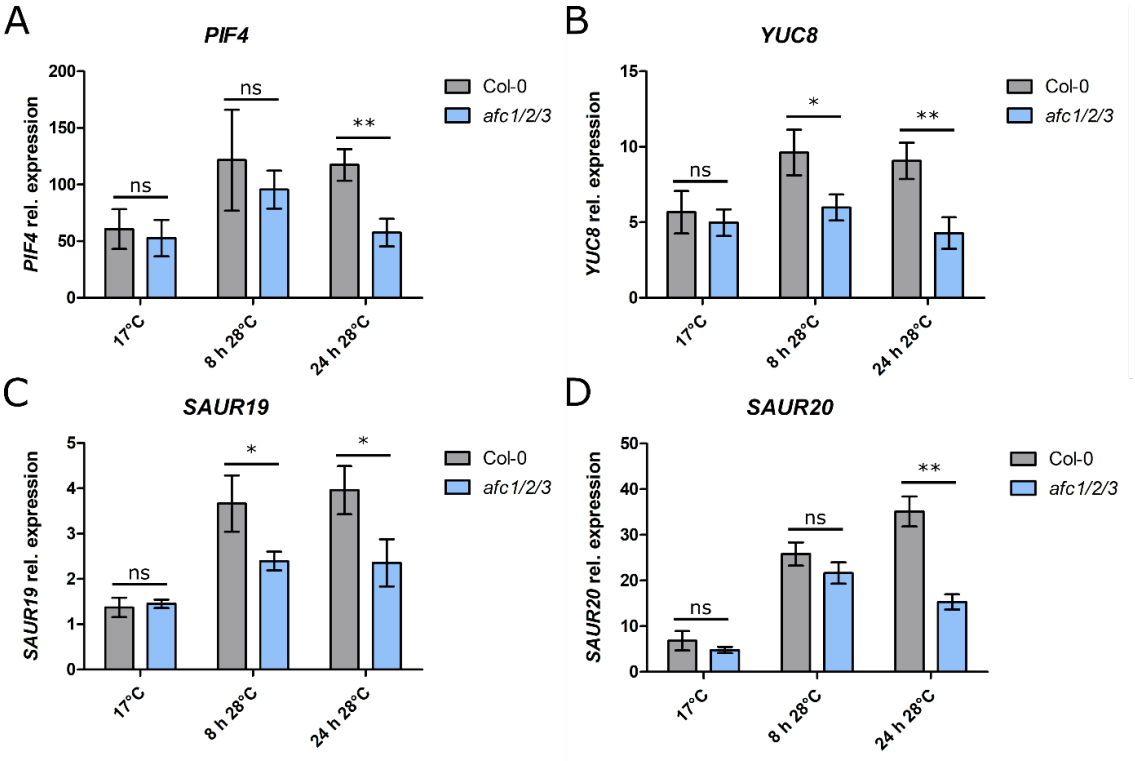

Figure 4-19 AtAFCs influence heat response gene expression in a PIF4 dependent manner. Gene expression analysis via RT-qPCR of AtAFC triple knock-out (afc1/2/3) and WT (Col-0) plants cultured at 17°C or 28°C for 8 h or 24 h. qPCR with gene-specific primers for **A** PIF4. **B** YUC8. **C** SAUR19. **D** SAUR20. 17°C n = 4, 28°C n = 3. Measurements in technical duplicates. Relative expression to TIP41(AT4G34270) was calculated. Shown are mean and standard deviation. Statistically significant differences determined by unpaired Welch t-test are indicated as asterisks (*: $p < 0.05$, **: $p < 0.01$, ***: $p < 0.001$). Plant RNAs were supplied by Dr. Daniel Maag.

5 Discussion

5.1 Evolution of CLK active temperature range.

We successfully expressed reconstructed ancestral CLK4 kinase domains and characterized their temperature activity profiles. A gradual shift of the active temperature range from a common ancestor, whose activity curve was higher than mouse but lower than birds via an intermediate bird ancestor could be shown (Figure 4-4 B). Revisiting the observed structural differences between N3 and N9 the small changes in interactions (Figure 4-2) agree with only slight differences in the temperature activity profiles. But in contrast to our results in the *in vitro* kinase assays one would expect N3 to exhibit activity at higher temperatures because there the interactions stabilize the kinase more, especially the interaction between activation segment and αC helix (Figure 4-2 D). No clear structure-activity relationship can be drawn from the structure predictions and the *in vitro* kinase assays. Since the structures are AlphaFold predictions information on side chain orientation might not necessarily represent the native state and some changed interactions might have escaped detection. Furthermore, CLK substrate binding is not fully characterized so far, in contrast to for example SRPKs, and no distinct binding grooves are known. Some differing residues might affect substrate interaction depending on their orientation which might change with temperature.

For an intermediate turtle ancestor, the active temperature range was even higher than for birds despite reptile CLKs exhibiting a lower active temperature range (Figure 4-5 B). Considering that only 10 residues differ between both intermediate ancestors kinase domains (N7 and N9, Figure 4-1 B) and that these differences only amount to two small changes in intra molecular interactions (Figure 4-3) the similar active temperature range is not surprising. The slightly higher activity at higher temperatures in N7 CLK4-KD might be due to the interaction between αC and αE helix (Figure 4-3 B). This unexpected result could be due to a fault in ancestor selection for analysis, where N7 is still closer related to birds than to turtles, and N8 should have been selected. But this would mean, that the whole shift from a CLK active up to 40°C to one that is not active above 35°C has to be pinpointed to a substitution of aspartate to asparagine in position 332 in the activation

segment and alanine to serine in position 444 at the αI helix (see MSA, Figure 4-1 B), since these are the only two residue differing between N7 and N8. This is highly unlikely since both residue changes are not conserved in Chinese soft-shell turtle CLK4 (Cssh_turtle_4), green sea turtle CLK1 (Gs_turtle_1) and, more importantly, western painted turtle CLK1 (Ps_turtle_1), which exhibited activity only at low temperatures in our assays (Figure 4-5 B). Especially the more likely residue in the activation segment is an aspartate here. When comparing the sequences of all CLK4-KDs used in these assays (Figure 4-4 and Figure 4-5), only 10 unique residues can be found in the alligator CLK4 sequence (see MSA, Figure 4-1 B). All are located away from the catalytic center and the activation segment, and no direct impact can be inferred. Of these residues two changes are also evident in the turtle CLK1, arginine 199 in the αC helix is replaced by a cysteine and arginine 455 in the αI helix is replaced by a lysine. For arginine 455 no interaction or function can be inferred. Arginine 199 of the αC helix forms H-bonds to a conserved aspartate 231 in β5-sheet and might aid in orientation of the αC helix. However, in mouse CLK4 arginine 199 is also present despite activity at low temperatures. Also, these residues are not changed in the other turtle CLK4 sequences. To investigate if these residues are involved in CLK temperature activity profile regulation, N7 CLK4-KD exchange mutants R199C and R455K could be generated and subjected to *in vitro* kinase assays. If these residues are indeed responsible for CLK activity at low temperatures the CLK4s of the turtles in the MSA should be investigated for their temperature activity profiles to elucidate if they are active in the expected way according to the active temperature range of the turtles. If these CLKs show temperature activity profiles similar to their reconstructed ancestor above their active temperature range, it could suggest that poikilotherms possess multiple CLKs with activity in different temperature ranges.

In conclusion we could show a gradual evolution of the CLK4 active temperature range from a reconstructed common ancestral CLK4 via an intermediate bird ancestor CLK4 towards chicken CLK4. This gradual evolution could not be shown for the investigated poikilotherm CLK4s and further investigation is necessary.

More kinases from our reconstructed ancestral CLKs could be used to investigate the evolution of CLK1 activity. The CLK1 temperature activity profiles of certain animals would also be interesting. Kiwi CLK1 originates from a bird that shows a relatively low body temperature of 38°C (Farner et al., 1956) and platypus CLK1 originates from the

evolutionary most distinct mammal (Bino et al., 2019), that has a body temperature of 32°C (Grant, 1983) and can't withstand ambient temperatures exceeding 30°C (Robinson, 1954). The CLK1 of bearded dragon harbors a unique tyrosine at residue number 332 in the activation segment that is an aspartate in all other CLKs and its LAMMER motif is changed to LAMMQK. Since expression and/or purification of the full-length kinases proved difficult they could not be investigated in this project. After re-cloning of the corresponding kinase domains, they could be subjected to *in vitro* kinase assays as we showed for the selected CLK4s.

It has been shown that the kinase domain is sufficient to exhibit a similar temperature activity profile as the full-length kinase for CLK homologues from human and mouse (Haltenhof et al., 2020) and *A. thaliana* (data not published yet), with the N-terminus shifting the activity just slightly. Nevertheless, it would be of interest to elucidate how big the effect of the N-terminus of the reconstructed ancestral CLKs is, especially since the majority of amino acid sequence differences are located in the N-terminus (Figure 4-1 B). In addition, it has been shown that the N-terminus influences CLK localization and substrate interaction (Aubol et al., 2014; George et al., 2019). Unfortunately, soluble full-length ancestral CLKs could not be expressed. This could be solved by inclusion of different solubility tags, such as thioredoxin (Trx) (LaVallie et al., 1993) or maltose binding protein (MBP) (Pryor and Leiting, 1997).

5.2 Temperature sensitivity is not unique to the CLK family.

Our initial results concerning DYRK3 temperature dependent activity (Figure 4-6) suggest that not only the CLK family is thermosensitive. For the DYRK family reversibility of the inactivation at high temperatures needs to be shown as it was for CLKs (Haltenhof et al., 2020). In addition, thermostability of DYRK3 needs to be characterized using TSA or CD spectroscopy to be sure that local conformation changes and not global unfolding is the driver of inactivation at higher temperatures. Both assays were beyond the scope of this initial test. Since DYRK3 is involved in regulation of ER export (Gallo et al., 2023) this

suggests, that temperature could play a role in organization of ER exit sites and protein transport.

It has been shown that SRPKs, the next closest family (Figure 1-2 A), are not thermosensitive in contrast to CLKs and DYRKs (Haltenhof et al., 2020). Comparing the activation segments of all three families (Figure 6-2), serine at position 4, aspartate/glutamate at position 8, threonine at position 14 and proline at position 24 could play a role in mediating temperature sensitivity. Also, DYRK1 should be investigated as here position 8 and 14 are different compared to other DYRKs and CLKs. Other members of the CMGC group, especially GSKs and RCKs, should be investigated to determine if temperature sensitivity evolved after a DYRK and CLK ancestor diverged from SRPKs or if temperature sensitivity evolved earlier in the CMGC group and SRPKs lost it.

5.3 CmLIK phosphorylates CmSC35 in a temperature dependent manner.

We could show *in vitro* that one of the two existing SR-proteins in *C. merolae*, CmSC35, homologue to hSRSF2, gets phosphorylated in a temperature dependent manner by CmLIK, a LAMMER-like kinase present in this organism (Figure 4-7). In agreement with previous findings in other organisms (Haltenhof et al., 2020) substrate phosphorylation is high at the lower border (40°C) of *C. merolae* habitat temperature (Miyagishima and Tanaka, 2021) and steeply decreases over the habitat temperature range until nearly no activity can be observed at the upper border (52°C). This suggests, that even with only 27 introns (Stark et al., 2015) some splice events in *C. merolae* might be controlled by temperature and play a role in adaption to temperature changes and that this regulation mechanism is present already since the most simplest eukaryotes evolved.

While CmLIK auto phosphorylation observed in the assays with CmSC35 closely resembles the observations with GST-RS as substrate (Haltenhof, 2020), the substrate phosphorylation differs. The activity curve with CmSC35 aligns better with *C. merolae* habitat temperature and considering that CmSC35 is an expected physiological substrate this likely reflects nature better. Apart from the substrate used, there are two major differences between those assays which might affect the phosphorylation. While CmLIK-KD and CmSC35 were assayed in solution, GST-RS and GST-CmLIK-KD were investigated

coupled to glutathione beads. Possibly both proteins could not adapt favorable orientations towards each other at low temperatures due to steric hindrance. In addition, the reaction buffers differed. The CmSC35 assays were carried out in a MES buffer at pH 6.0 and the GST-RS assays in Tris-HCl pH 7.4. Tris buffer pH is significantly more temperature sensitive compared to MES, decreasing with increasing temperature. However, an effect of the pH is very unlikely as hCLK1 activity was shown to be constant over a range of different pH values (Haltenhof et al., 2020).

CmSC35 harbors four Arg-Ser dipeptides in its RS domain. Our intact mass LC-ESI-MS results show that while the main population exhibits 4.5 phosphorylations per molecule we can detect up to 10 phosphorylations per molecule (Figure 4-13 D). This suggested that CmSC35 also gets phosphorylated outside of its RS domain. Indeed, we found seven phosphorylation sites in our LC-ESI-MS/MS experiments (Figure 4-14 B, Figure 6-6 A). Four are located in the intrinsically disordered N-terminus and three in the folded RRM motif. To our surprise these phosphorylations increased with higher temperatures (Figure 6-6 B) in contrast to the total phosphorylation of CmSC35. This, together with their location outside of the RS domain, might suggest that they are *in vitro* artifacts. Another possibility would be that these phosphorylations are a separate regulatory mechanism that's inhibiting SR-protein function, especially with respect to those located in the RRM and possibly interfering with RNA binding. This could be investigated by generating phosphomimetic mutants of CmSC35, replacing serine with aspartate (Léger et al., 1997), and testing these mutants for their ability to enhance splicing. As expected, the phosphorylations in the RS domain could not be detected in the trypsin samples as trypsin cleaves after arginine residues (Keil, 1992), generating just short dipeptides that are neither detectable nor would they be assignable. Elastase, which has broader specificity (Rietschel et al., 2009), did not yield detectable peptides in this region either. In an effort to elucidate phosphosite usage in the RS domain one could repeat the experiment and use chemical cleavage by formic acid after aspartate residues (Li et al., 2001) possibly combined with chymotrypsin digest, cleaving after aromatic residues (Keil, 1992), to generate peptides of appropriate sizes. Another option would be to analyze the samples with matrix-assisted laser desorption/ionization combined with in-source decay (MALDI-ISD) MS to resolve the C-terminus where the RS domain is located (Nicolardi et al., 2020). This method poses the problem that CmLIK-KD and CmSC35 need

to be separated before spotting on the matrix because else signals from both proteins would overlap and make peptide peak assignment impossible.

Having characterized the phosphorylation of CmSC35, it would be of interest to also determine if and how CmLIK phosphorylates the second SR-protein found in *C. merolae*, CmRSP31. Expression of GST-tagged full-length CmRSP31 under standard conditions failed repeatedly. Generation of constructs containing CmRSP31 with different solubility tags, such as thioredoxin (Trx) (LaVallie et al., 1993) or maltose binding protein (MBP) (Pryor and Leiting, 1997), might solve this problem and enable investigation of the second SR-protein.

5.4 Regulation of CmLIK-KD active temperature range.

Aside from its activity at high temperatures, CmLIK sets itself apart from other CLKs as its auto phosphorylation does not follow the same pattern as the substrate phosphorylation. As auto phosphorylation increases, substrate phosphorylation decreases. This suggests, that while for other CLKs auto phosphorylation enhances activity it is inhibitory for CmLIK-KD.

We characterized one phosphorylation at T683 via structural analysis and generation of a mutant lacking this phospho site. The significant decrease in T_m of the T683V mutant that is only observed in the presence of ATP and neither with AMPPNP nor in the apo state is an evidence for a phosphorylation dependent stabilization of CmLIK-KD via T683. Abolishment of T683 phosphorylation increased substrate phosphorylation significantly at 39°C and 45°C indicating that here auto phosphorylation is used for fine tuning CmLIK activity at the lower temperature edge. This activity is likely mediated by interactions of the phosphorylated threonine with E677 of the αF helix and Y651 of the activation segment, stabilizing the activation segment in an unfavorable conformation for catalysis. A significant decrease in auto phosphorylation could only be observed below 35°C, where total auto phosphorylation was low. This is likely due to the fact, that one missing

phosphorylation site is not detectable if up to 11 sites are phosphorylated per molecule at higher temperatures, as is evident in our intact mass LC-ESI-MS data (Figure 4-12 A). In addition, we identified several auto phosphorylation sites via LC-ESI-MS/MS. While not for all sites a probable effect could be inferred from their position in the structure, some residues positions hint at their function (Figure 4-15).

Phosphorylation of Y468 and T490 might disturb folding of the N-lobe, especially since T490 forms an H-bond to D487 that stabilizes the loop between β2 and β3. One of the most striking sites is T599 which is located directly in the catalytic center. Phosphorylation at this residue would very likely interfere with the catalyzed reaction. Phospho site S632 is located in the P-loop (Saraste et al., 1990), at the site of Mg^{2+} coordination. Even though we could not show metal coordination in our structure due to lack of density, the aspartate of the DFG motif is usually involved in metal coordination in kinases (Knape and Herberg, 2017) and the loop this residue is in is termed the Mg^{2+}-binding loop (Nolen et al., 2004). As such phosphorylation at S632 is likely to interfere with Mg^{2+} coordination necessary for catalytic activity.

The residues corresponding to S647 and T648 in hCLK1 have been suggested to position the activation segment in a conformation which clashes with substrate binding (Haltenhof et al., 2020). S620 is located in the loop that replaces the β-hairpin which is present in all other CLKs and buries the MAPK substrate interaction groove (Bullock et al., 2009), so this might have an effect on substrate interaction in CmLIK. Similarly, S749, S752 and S770 are located around the αH helix which buries the substrate binding groove present in SRPK (Ngo et al., 2008; Bullock et al., 2009). In fact, S770 is located in the interaction interface between the C-lobe of chain B and N-lobe of chain A in our crystal structure (Figure 4-8 D), sandwiched between the interactions of E767 with V453 and F772 with K481. On the opposite side of S770, the phospho sites Y451 and S452 are located in the N-lobe part of this interface. Another phospho site, S476, is directly involved in the interaction interface, as this Ser forms an H-bond to the backbone of P774, adjacent to E775 which forms an H-bond to R500, the last interaction that constitutes the interaction interface. So, phosphorylation at these four sites is very likely

to interfere with interaction between CmLIK monomers and might also play a role in substrate binding.

For S716 and S718, located in the MAPK-like insertion, and T788 and S798, located towards the C-terminus, no effect could be inferred. The role of phosphorylation at T811 and T814 in the C-terminal tail is also not clear. Interestingly the C-terminal tail of chain B of our structure can be modeled with low confidence in a way that it interacts with the αH helix, P+1 loop and S632 of chain A (Figure 6-4 A) and position T814 in a position near the catalytic center suitable for phosphorylation (Figure 6-4 B).

Overall, the observed phosphorylations might exert auto inhibitory effects either by disturbing the catalytic center or by interfering with substrate binding. Detailed information on the effects of individual auto phosphorylations could be obtained by generating mutants that either mimic phosphorylation – replacement of serine or threonine by aspartate (Léger et al., 1997) – or by abolishing the phospho site, for example by replacement with alanine or valine. Especially phosphomimetic replacement of S467 and S770 would be interesting for investigation of the observed interaction interface and to elucidate if these phosphorylations interfere with substrate interaction.

While we identified 20 phosphorylated sites in CmLIK (Figure 4-14 A), we observed a maximum of 11 phosphorylations per molecule (Figure 4-12). This suggests, that even after 30 min at 49°C not all possible phosphorylation sites are used on every molecule and that a heterogenous population with differing phosphorylations exists. Considering how close some phosphorylation sites are with only one or no residue between them it is possible that some sites are redundant. Considering that only about 75 % of CmLIK-KD sequence was covered by LC-ESI-MS/MS analysis it is likely that not all phosphorylation sites were observed. For example, T683 was not detected in this assay because of its position in a sequence lacking coverage even though its phosphorylation could be proven with other methods. Thus, it would be interesting to repeat the assay with a different set of proteases for digestion to expand the sequence coverage. A suitable protease would be chymotrypsin (Keil, 1992).

We could expand the characterization of a salt bridge between the activation segment and the loop between αF and αG helix that is essential for CmLIK activity at 45°C and 49°C, so in the range that is relevant to *C. merolae* habitat temperature (Figure 4-10 A, B). The CmLIK-KD D690S exchange mutant in which the salt bridge was abolished by

replacing the aspartate involved in it by the serine that is the corresponding residue in hCLK1 exhibited reduced thermostability in the apo state and in presence of AMPPNP. This decrease could be almost rescued in the presence of ATP, so in a phosphorylation dependent manner (Figure 4-10 C). In accordance with this the D690S mutant exhibited elevated auto phosphorylation at 45°C and less in the radioactive assays (Figure 4-10A, B), on average one auto phosphorylation more than the WT in intact mass LC-ESI-MS analysis (Figure 4-12 D) and phosphorylation on S690 could be observed by LC-ESI-MS/MS (Figure 4-10 D). The stabilizing effect of serine phosphorylation is not surprising since aspartate can be used to mimic phosphorylated serine (Léger et al., 1997), which is here used the other way around. Considering that this serine and the arginine in the activation segment are conserved throughout animal CLKs this observation has implications beyond CmLIK. In human, mouse and other mammalian CLKs this serine is even followed by an arginine, creating a canonical CLK target phosphorylation site. It is likely that other CLKs are auto phosphorylated in a stimulating way at this serine to stabilize the activation segment in an active conformation. This also agrees with the observation that in other CLKs auto and substrate phosphorylation correlate with each other (Haltenhof et al., 2020). Previously it has been shown that substituting this serine in mCLK1 with aspartate, mimicking phosphorylation and establishing the CmLIK salt bridge, results in activity at higher temperatures than the WT (Haltenhof, 2020). To further investigate the role of phosphorylation of this serine it would be of interest to replace it with alanine to abolish the phosphorylation site and see which effect lack of phosphorylation causes in comparison to constitutive phosphorylation.

Even though the loop between β7 and β8 in CmLIK is unstructured and flexible it appeared to be essential for CmLIK thermostability (Figure 4-11 E), substrate and auto phosphorylation (Figure 4-11 C,D, Figure 4-12 C, G). In the structure of the CmLIK-KD hairpin mutant we obtained (Figure 4-11 A) the protein folded correctly, no interactions out of this region were changed and the hairpin insertion also did not interfere with the interaction interface observed in the CmLIK-KD WT structure. So, while we observed a drastic effect of the mutant, we could not find a molecular basis for this. One possible reason for this would be that the flexibility of the CmLIK loop is needed to allow an interaction with itself and/or the substrate in a mode, that is different from the one observed in the WT structure and that the extension by the β-hairpin paired with its more

rigid folding interferes with this. Considering the drastically reduced number of auto phosphorylations per CmLIK-KD molecule we observed in the hairpin mutant (Figure 4-12 D), even though no residues for which phosphorylation was observed in the WT were lost by the insertion, it seems very likely that the β-hairpin blocks an interaction site that is important for stabilizing auto phosphorylation.

All in all, we could characterize several modes of activity regulation in CmLIK-KD. Activity at high temperatures is achieved by stabilization of its activation segment via a salt bridge between D690 and R649, while it is fine-tuned towards the lower temperature edge by auto phosphorylation at T683 which interacts with E677 and Y651. CmLIK-KD auto phosphorylation at high temperatures appears to act auto inhibitory either by disrupting the catalytic center or interfering with substrate interaction interfaces. The flexible loop between β7 and β8 appears to be important for substrate interaction and thermostability. In addition, we could show one possible mode of binding for trans auto phosphorylation depending on the interaction of the loop between αH and αI helix of one CmLIK-KD molecule with the N-lobe of another CmLIK-KD molecule.

5.5 Activation segment stabilization appears to be a common mechanism for CLK activity at high temperatures.

During the investigation of AtAFC temperature sensitivity regulation we found an H-bond network around Q254 in the AtAFC3 activation segment that was not present in AtAFC1 (Figure 4-17 B). Elimination of this H-bond network by mutation of Q254 to alanine reduced AtAFC3 activity at high temperatures (Figure 4-17 E). Taken together with our observations on the importance of the salt bridge in CmLIK, this suggests that activation segment stabilization in the P+1 loop by extended H-bonds is a common motif in CLKs active at high temperatures. To validate the significance of the H-bond network around AtAFC3 Q254 further, generation of an AtAFC1 S301Q exchange mutant and investigation of its activity at high temperatures would be of interest.

Abrogation of the H-bond network around Q254 reduced AtAFC3 activity at high temperatures but failed to enhance activity at low temperatures to AtAFC1 level. Thus, a different mechanism must inhibit AtAFC3 activity, respectively enhance AtAFC1 activity at low temperatures. Possibly this is facilitated by changes of conformation and

interactions in the activation loop directly after the P-loop (Figure 4-17 C). While in AtAFC3 this loop (^{243}VCDNRIHHS^{251}) is oriented more outwards and exhibits more interactions with other structural elements, it is oriented more towards the catalytic center and exhibits more interactions with itself in AtAFC1 (^{290}TFEHQDHNY^{298}). These interactions likely stabilize an inactive conformation in AtAFC3 and an active conformation in AtAFC1, resulting in opposite effects when they're loosened at high temperatures. This hypothesis could be tested by generation of AtAFC1 and AtAFC3 mutants where this loop is exchanged.

5.6 AtAFC2 might link rhythmic copper homeostasis to alternative splicing.

For AtAFC2 initial assays observed relatively stable activity up to 24°C followed by a decrease until activity was almost abolished at 36°C. This observation is consistent with a relatively recent publication (Lin et al., 2022). When investigating the structural differences between AtAFC2 and AtAFC1 we observed two very striking elements. A possible disulfide bond connecting N- and C-lobe (Figure 4-18 B) and a copper binding motif (Rubino and Franz, 2012) between αC and αE helix close to the catalytic center, which could also involve the histidine of the catalytic loop HTD motif (Figure 4-18 C). The two cysteines could also participate in copper coordination since they're directly adjacent to the other motif, but their orientation and distance makes a disulfide bond more likely. Both observations taken together with the relatively stable activity across a broad temperature range could indicate that AtAFC2 activity is less temperature dependent and more sensible to copper binding.

Interestingly copper uptake in *A. thaliana* is under control of an autoregulatory negative feedback loop (Peñarrubia et al., 2010), as expression of copper transporters (COPT) is downregulated by copper (Sancenón et al., 2003). This feedback loop results in oscillation of copper levels which in turn results in rhythmic expression of copper response genes (Cohu and Pilon, 2007) under control of cis regulatory elements in their promotors, GTAC motifs (Kropat et al., 2005), and the corresponding trans acting factors, SPL transcription factors (Yamasaki et al., 2009). It has been shown that rhythmic copper homeostasis influences the circadian clock and is itself also influenced by it in *A. thaliana* (Perea-García et al., 2016). Connection of copper with circadian rhythms has also been

reported in other organisms (Bell-Pedersen et al., 1996; Borjigin et al., 1999; Riese et al., 2008). Considering that CLKs control rhythmic splicing in mammals (Preußner et al., 2017; Haltenhof et al., 2020), it is not too farfetched that AtAFC2 connects rhythmic copper homeostasis with alternative splicing in *A. thaliana*. To explore this hypothesis, it would be of utmost interest to investigate copper dependent activity of AtAFC2.

We generated an AtAFC2 C210S mutant to investigate the effect of the disulfide bridge. Under the previous assay conditions, the mutant showed the same activity as the WT (Figure 6-7). In retrospect this result is not surprising for two reasons. On one hand both proteins were expressed in *E. coli* BL21(DE3) pRare. Unspecialized *E. coli* strains are in general not suitable for expression of proteins with disulfide bonds due to the reductive cytoplasm (Prinz et al., 1997), so no disulfide bond would be present in the WT due to the expression system. On the other hand, the standard *in vitro* kinase assay buffer contained 5 mM DTT, which would reduce any disulfide bond present in the WT.

We tried to circumvent the first issue by changing the expression system to *E. coli* RosettaGami2, a strain that contains a mutation in the *trxB* gene and is suitable for cytoplasmatic expression of proteins containing disulfide bonds (Derman et al., 1993). While we observed expression of both His-TEV-AtAFC2-KD WT and C210S both proteins precipitated during purification at various stages. To solve this problem buffer screens should be carried out. So far Tris-HCl has been used as a buffer system with pH 8.0 and 7.5, yielding no differences. Addition of $MgCl_2$ to stabilize the kinase also yielded no improvement. The buffer system could be changed to MES or HEPES for example and a broader pH range should be tested. Addition of glycerol could be tried. For hCLK1 addition of 50 mM L-Glu and 50 mM L-Arg was used to increase solubility (Golovanov et al., 2004; Bullock et al., 2009) this could also be tried for AtAFC2.

Once both proteins are purified in sufficient amount their temperature activity profile should be characterized by *in vitro* kinase assays without DTT in the reaction buffer. The assays should also be carried out at a stable temperature with different concentrations of $CuSO_4$ in the reaction buffer to investigate copper dependence of AtAFC2 activity. For characterization of both disulfide bond formation and copper coordination AtAFC2-KD WT crystallization should be attempted. Disulfide bond formation could also be investigated via LC-ESI-MS/MS (Lakbub et al., 2018) or using Ellman's reagent after carboxymethylation of free thiols (Aitken and Learmonth, 2009). Copper binding could

also be evaluated using colorimetric assays (Wilkinson-White and Easterbrook-Smith, 2008).

While elucidating if AtAFC2 activity is copper dependent is of great interest, investigation of the effect of the potential disulfide bond is also relevant. If a change of activity is observed in dependence of the presence of the disulfide bond, this would be an example that kinase sequence and structure need to be investigated for disulfide bonds prior to *in vitro* kinase assays. Also, this would suggest that maybe not all kinase assays performed so far reflect the physiological activity as DTT is used as a component in standard *in vitro* kinase assays buffers and disulfide bond effects are lost.

5.7 AFCs contribute to thermomorphogenesis in a PIF4 dependent manner.

Our cooperation partner at University of Würzburg could show impaired thermomorphogenesis in *afc1/2/3* triple knock-out *A. thaliana* plants. The gene expression analysis presented here shows that this impairment is mediated via downregulation of heat induced PIF4 expression and subsequent reduction of expression of PIF4 target genes, including auxin biosynthesis genes such as YUC8, which in turn leads to reduced auxin levels and thus to reduced inducible expression of auxin target genes, such as SAUR19 and SAUR20, which regulate elongation growth. This is in line with current knowledge of thermomorphogenesis under PIF4 control (Quint et al., 2016). AtAFC activity seems to be especially necessary to sustain elevated PIF4 levels during longer exposure to high temperatures (Figure 4-19 A). With these insights we can add temperature dependent AtAFC activity, respectively alternative splicing, as another player in the complex control of PIF4 expression and activity. This is further supported by observed differences in temperature dependent splicing in *afc1/2/3* triple knock-out plants. Most notably splicing of transcripts of genes involved in RNA processing, among them SR proteins, changed in the knock-outs (data not published yet).

In contrast to our findings that AtAFC activity is needed for correct induction of heat responsive hypocotyl growth, a relatively recent study attributed an inhibitory role in the context of heat induced hypocotyl growth to AtAFC2 (Lin et al., 2022). In single knock-outs of our cooperation partner at University of Würzburg no phenotype could be observed (data not published yet). While the above-mentioned study showed a

phenotype for AtAFC2 knock-out, they did neither show gene expression analysis of any genes involved in the cascade controlling thermomorphogenesis, nor analysis of alternative splice events in the transcripts of these genes in the AtAFC2 knock-out. So, they could not elucidate where AtAFC2 would exert regulatory function during thermomorphogenesis. The *in vitro* kinase assays shown for AtAFC2 are subject to the same limitations described above, as the kinase was expressed in an *E. coli* strain not suitable for disulfide bond generation and DTT in the reaction buffer would reduce any present disulfide bond. This means that the observed temperature activity relationship is not necessarily physiologic. We could not elucidate separate functions for individual AtAFCs in thermomorphogensis, but rather show that the ensemble of AtAFC1/2/3 is necessary for correct regulation of this process. The lack of phenotypes in single AtAFC knock-outs might be due to redundancy in substrate phosphorylation. Considering that AtAFC2 and AtAFC3 activity at 28°C do not differ significantly and that also AtAFC1 still shows moderate activity this is not unlikely. Still the findings of the above-mentioned study could agree with our results if we assume that AtAFC1 and/or AtAFC3 are necessary for heat induced PIF4 expression and AtAFC2 fine tunes gene expression downstream of PIF4 via alternative splicing of induced transcripts.

5.8 Application of CLK homologue active temperature range modulation.

In this thesis we have characterized several structural mechanisms of CLK homologues that modulate the active temperature range of the kinases, especially with regard to enabling activity at high temperatures.

In humans the discovery of temperature dependent CLK activity can be used to enhance treatment of diseases in which dysregulation of CLKs plays a role by reducing or increasing the temperature of the patient or at least the affected tissue additionally to other treatments. For certain cancers hyperthermia treatment is already established (Crezee et al., 2021). But since CLK dysregulation is associated with more diseases thermal treatment could also be applied for other diseases such as osteoarthritis (Deshmukh et al., 2019) or Alzheimer's disease (Glatz et al., 2006).

Having shown that plant CLK homologues, AFCs, play a role in thermomorphogenesis regulation and thus in adaptation to higher temperatures and considering the rising

threat of global warming for crop plants (Janni et al., 2023), engineering of crop plant AFCs might pose one part of a solution to the challenge of global warming. We could show that activation segment stabilization is a viable method to allow AFC activity at higher temperatures. Introduction of the salt bridge present in CmLIK necessitates just a single residue replacement with aspartate in AFCs and could very likely enable AFC activity at higher temperatures. This could facilitate adaptation of plant growth to higher temperatures via simple genetic engineering. Other viable changes in AFC activation segment environment could be explored via modelling of mutants with AlphaFold and molecular dynamics simulations (Hollingsworth and Dror, 2018) followed by generation of transgenic plants with promising AFC mutant candidates.

Other organisms threatened by global warming are reptiles that exhibit temperature dependent sex determination due to increasing feminization or masculinization of the species (Valenzuela et al., 2019). Since it has been shown that the temperature dependent switch of CLK activity of such reptiles coincides with the switch between male and female producing temperature (Haltenhof et al., 2020), engineering those CLKs to exhibit activity at higher temperatures, for example by introduction of elements stabilizing the activation segment, might be a way to preserve sex distribution in those species.

6 Supplement

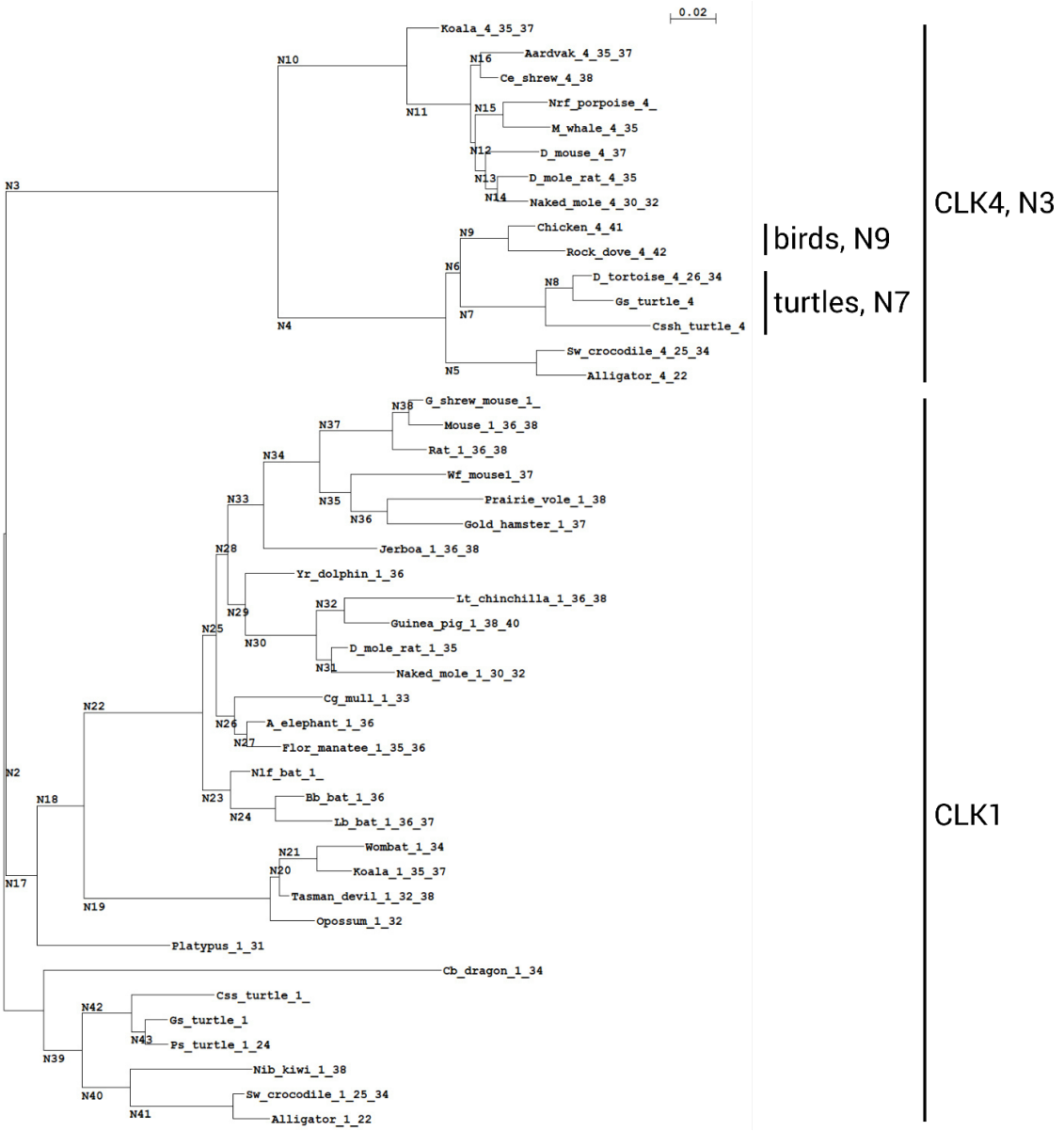

Figure 6-1 Phylogenetic tree of CLK1 and CLK4. Phylogenetic tree of selected CLK1 and CLK4 sequences calculated by Dr. Rainer Merkl and Dr. Kristina Straub. Rooted using DYRK1 as outgroup. Species are labeled as "species_CLK1/4_body temperature or active temperature range in °C if applicable". Identifiers of calculated ancestral sequences are indicated at branches. Branch length scale indicated on top. Ancestral CLK4s that were further used, and their corresponding branches indicated on the right.

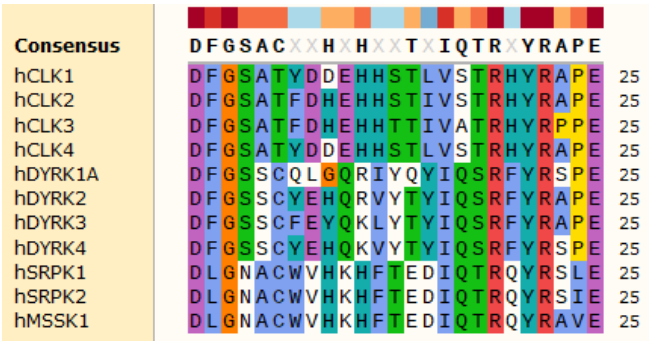

Figure 6-2 Human CLK, DYRK and SRPK family activation segment sequences. Multiple sequence alignment of hCLK1-4, hDYRK1-3, hSRPK1/2 and hMSSK1 activation segments. Conservation as colored blocks and consensus sequence shown on top. Residues colored according to properties and conservation (Clustal X color scheme).

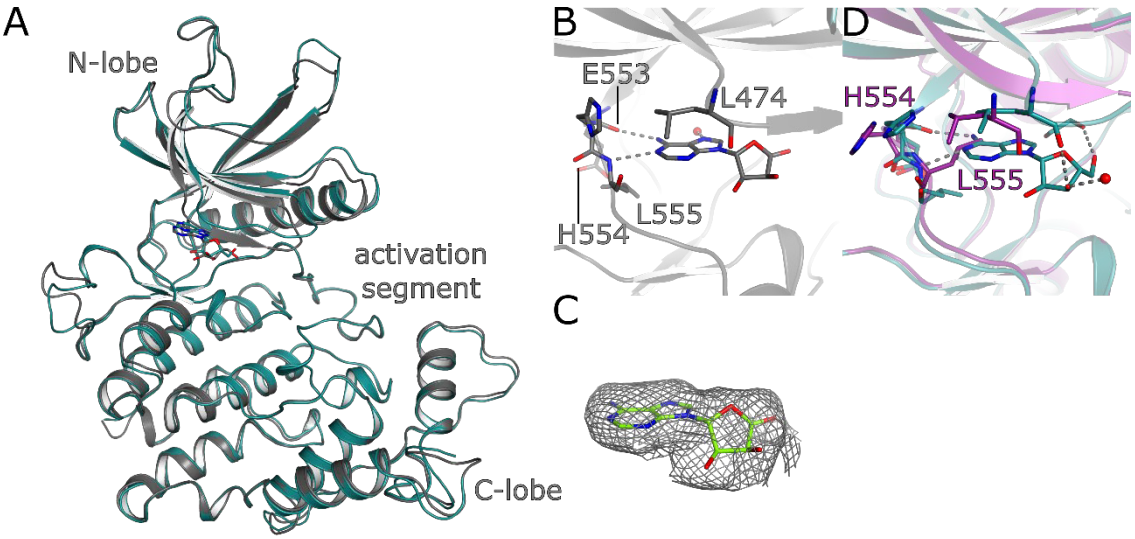

Figure 6-3 Comparison of CmLIK-KD WT chain A and B. A Asymmetric unit contents of CmLIK-KD structure at 2.69 Å resolution. Protein depicted as cartoon, chain A colored in grey, chain B colored in deep teal. Nucleotide depicted as sticks. Superimposition of chain B on chain A. **B** Zoom in on adenosine of chain A, interacting residues depicted as sticks. H-bond distance cut-off = 3.2 Å. **C** Polder electron density map of chain A adenosine contoured at σ = 3.0. Adenosine colored in chartreuse. **D** Zoom in on adenosine of chain B superimposed with first CmLIK-KD WT structure in deep purple. Interacting residues depicted as sticks.

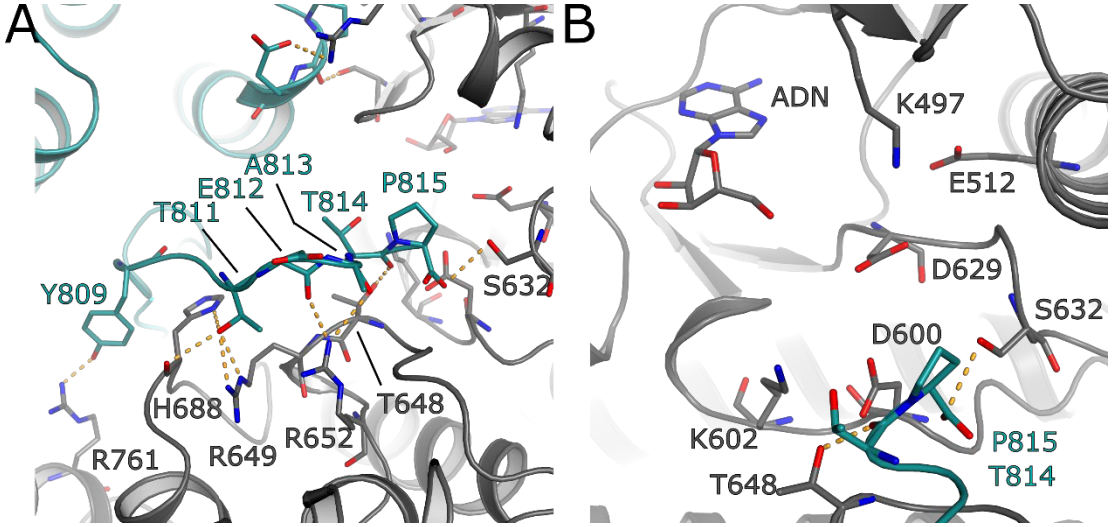

Figure 6-4 Low confidence modeling of CmLIK-KD C-terminal tail for auto phosphorylation. CmLIK-KD WT structure at 2.69 Å resolution from Figure 4-8 depicted as cartoon. Chain A is colored in grey and chain B in deep teal. **A** Low confidence modeling (B-factors of 50-100 at an occupancy of 0.44) of chain B C-terminal tail (residues 808-815). Interacting residues are depicted as sticks and labeled. H-bonds (distance cut-off = 3.2 Å) are depicted as dashed lines in bright orange. **B** Catalytic center of chain A. Conserved catalytically relevant residues depicted as sticks and labeled in addition to residues interacting with chain B C-terminal tail. H-bonds (distance cut-off = 3.2 Å) are depicted as dashed lines in bright orange.

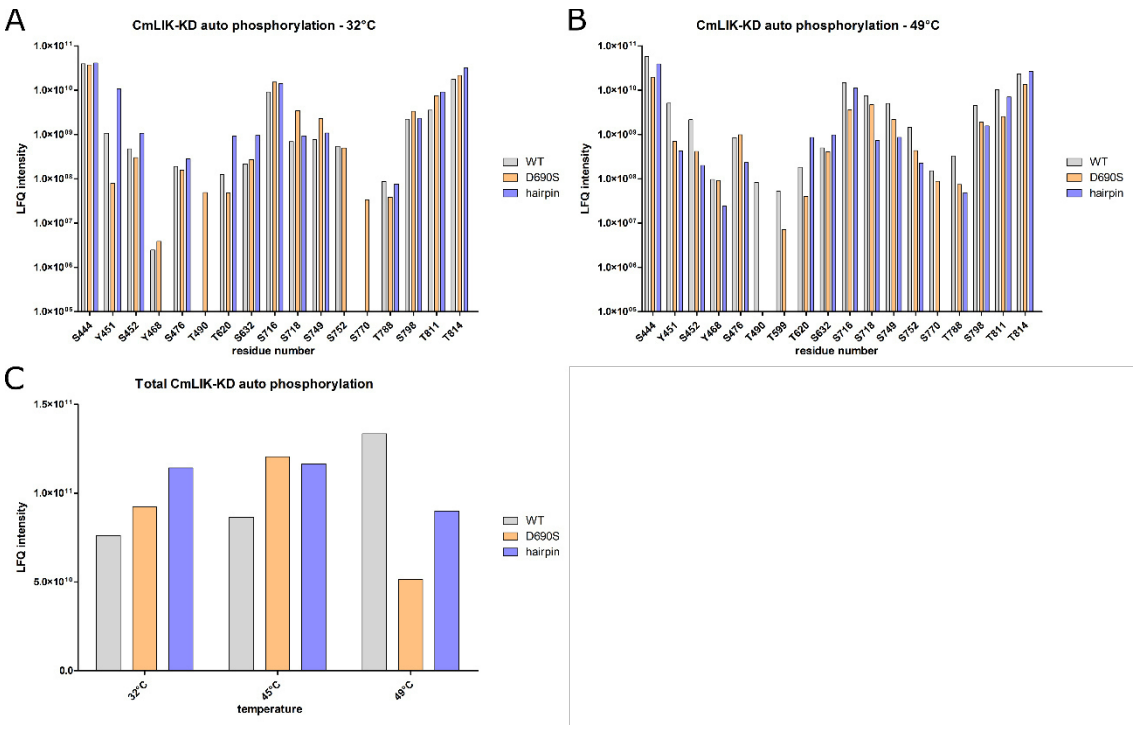

Figure 6-5 Extended analysis of CmLIK-KD auto phosphorylation sites. A Label-free quantification (LFQ) of phosphopeptide intensities of CmLIK-KD. Indicated CmLIK-KD variants were incubated with CmSC35 in the presence of ATP at 32°C for 30 min, proteins separated via SDS-PAGE, in gel digested with trypsin, peptides extracted and subjected to LC-ESI-MS/MS. Data was analyzed and spectra quantified using the FragPipe LFQ-phospho workflow. Intensities are displayed on a logarithmic scale. Residue numbering corresponds to CmLIK-KD WT. **B** As in A, but reaction was

carried out at 49°C. **C** Sum of all LFQ intensities of CmLIK-KD peptides containing phosphorylated residues. Experimental setup as in A, but reaction was carried out at 32°C, 45°C and 49°C.

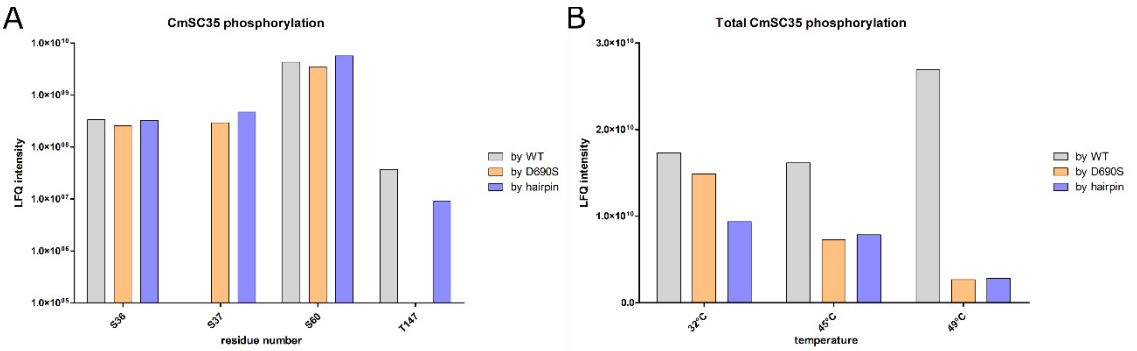

Figure 6-6 Extended analysis of CmSC35 phosphorylation sites. A Label-free quantification (LFQ) of phosphopeptide intensities of CmSC35. Indicated CmLIK-KD variants were incubated with CmSC35 in the presence of ATP at 32°C for 30 min, proteins separated via SDS-PAGE, in gel digested with elastase, peptides extracted and subjected to LC-ESI-MS/MS. Data was analyzed and spectra quantified using the FragPipe LFQ-phospho workflow. Intensities are displayed on a logarithmic scale. **B** Sum of all LFQ intensities of CmSC35 peptides containing phosphorylated residues. Experimental setup as in A, but reaction was carried out at 32°C, 45°C and 49°C and proteins were digested with trypsin.

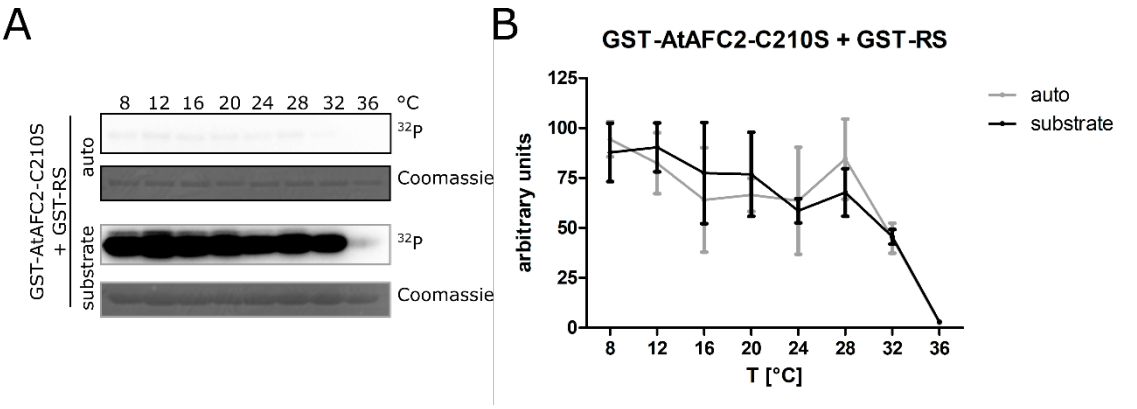

Figure 6-7 Temperature activity profile of AtAFC2 C210S mutant in the presence of DTT. A Representative SDS-PAGE gel of on-bead *in vitro* kinase assays of GST-AtAFC2 f.l. C210S with synthetic GST-RS substrate. Sample temperature is indicated on top. Protein loading detected by Coomassie staining and phosphorylation detected by autoradiography are shown for the kinase (auto) and substrate. **B** Quantification of auto and substrate phosphorylation from the on-bead *in vitro* kinase assays in A. Radioactive signal was normalized to highest signal in assay. Shown are mean and standard deviation. n = 3.

Table 2 CmLIK-KD hairpin crystallization conditions

Nucleotide	Screen	Well	condition	crystal shape
apo	PEG I	G4	0.2 M Ca acetate, 20 % (w/v) PEG-3350	cube
apo	PEG II	H10	0.2 M Mg acetate, 10 % (w/v) PEG-8000	rod
apo	Classics	B1	0.1 M Tris-HCl pH 8.5, 20 % (v/v) ethanol	rod
apo	FS#1	A2	0.25 M Ca acetate, 14 % (w/v) PEG-3350	rod / envelope
apo	FS#1	A6	0.25 M Ca acetate, 4 % (w/v) PEG-8000	rod / envelope
apo	FS#1	B6	0.25 M Ca acetate, 6 % (w/v) PEG-8000	rod / envelope
AMPPNP	FS#2	1A-D	0.25 M Ca acetate, 4 % (w/v) PEG-8000	bipyramidal
AMPPNP	FS#2	3A-D	0.2 M Ca acetate, 4 % (w/v) PEG-8000	bipyramidal
AMPPNP	FS#2	4A-D	0.2 M Ca acetate, 6 % (w/v) PEG-8000	bipyramidal
AMPPNP	FS#2	5A-D	0.5 M Ca acetate, 8 % (w/v) PEG-8000	bipyramidal
AMPPNP	FS#2	6A-D	0.1 M Tris-HCl pH 8.5, 20 % (v/v) ethanol	rods
AMPPNP	FS#3	1A-D	0.25 M Ca acetate, 4 % (w/v) PEG-8000	bipyramidal

Table 3 Crystallographic data

Data set	CmLIK-KD WT (Haltenhof, 2020)	CmLIK-KD WT with bound adenosine	CmLIK-KD hairpin
PDB entry	9FMO	9FMP	9FMQ
Data collection			
Wavelength (Å)	0.9184	0.9184	0.9762
Temperature (K)	100	100	100
Space group	$P2_12_12_1$	$P2_12_12_1$	$P2_12_12_1$
a, *b*, *c* (Å)	65.5, 70.4, 88.2	71.1, 100.9, 109.7	64.7, 68.7, 84.7
α, β, γ (°)	90, 90, 90	90, 90, 90	90, 90, 90
Resolution (Å)	50.00–2.49 (2.64–2.49)	50.00–2.70 (2.85–2.69)	50.00–1.77 (1.88–1.77)
Reflections			
Unique	14748 (2323)	22375 (3593)	37481 (5958)
Completeness (%)	99.0 (98.7)	99.2 (95.4)	100.0 (99.9)
Multiplicity	7.4 (7.6)	13.2 (13.0)	13.3 (13.8)
Data quality			
Intensity $\langle I/\sigma(I)\rangle$	9.39 (0.95)	5.24 (1.06)	19.94 (1.06)
Rmeas[†] (%)	19.2 (221.9)	55.4 (234.2)	6.4 (244.9)
CC1/2[‡]	99.6 (32.7)	97.6 (47.6)	100.0 (54.4)
Wilson *B* value (Å^2)	57.2	39.4	48.7
Refinement			
Resolution (Å)	37.38–2.49 (2.68–2.49)	48.18–2.69 (2.81–2.69)	42.36–1.77 (1.82–1.77)

Reflections			
Number	14723 (2895)	22370 (2496)	37478 (2842)
Test set (%)	5.01	5.00	5.00
R_{work} (%)	22.99 (32.11)	20.32 (26.50)	19.19 (31.23)
R_{free} (%)	26.68 (35.86)	26.78 (33.60)	22.98 (33.39)
Asymmetric unit			
Protein residues	357	717	355
Ethylene glycols	1	27	8
Waters	13	92	85
Mean temperature factors (Å^2)			
All atoms	57.60	43.13	54.38
Macromolecules	57.61	43.12	54.45
Ligands	62.85	47.67	58.68
Water molecules	52.60	36.70	49.57
R.m.s.d. from target geometry			
Bond lengths (Å)	0.003	0.003	0.011
Bond angles (°)	0.57	0.57	1.12
Validation statistics			
Ramachandran plot, residues in			
Allowed regions (%)	3.7	4.1	3.1
Favoured regions (%)	96.0	95.6	96.9
Ramachandran plot *Z*-score (r.m.s.d.)			
Whole	-	-1.12 (0.29)	-0.81 (0.39)
Helix	-	-0.59 (0.28)	-0.32 (0.39)
Sheet	-	-1.09 (0.50)	-0.73 (0.88)
Loop	-	-0.66 (0.32)	-0.57 (0.39)
MolProbity clashscore[¶ ††]	3.77	4.69	5.57
MolProbity score[¶]	1.43	1.92	1.93
Poor rotamers (%)	0	3.13	3.75
C^{β} deviations (%)	0	0	0

Values in parentheses correspond to highest resolution shell.

[†] $R_{meas}(I) = \sum_{hkl}\{N(hkl)/[N(hkl)-1]\}^{1/2}\sum_i |I_i(hkl) - \langle I(hkl)\rangle|/\sum_{hkl}\sum_i I_i(hkl)$, where $\langle I(hkl)\rangle$ is the mean intensity of symmetry-equivalent reflections *hkl*, $I_i(hkl)$ is the intensity of a particular observation of *hkl* and $N(hkl)$ is the number of redundant observations of reflection *hkl* (Diederichs and Karplus, 1997).

‡$CC_{1/2} = (\langle I^2 \rangle - \langle I \rangle^2)/(\langle I^2 \rangle - \langle I \rangle^2 + \sigma_\varepsilon^2$, where $\sigma_\varepsilon^2$is the mean error within a half data set (Karplus and Diederichs, 2012).

¶Calculated with *MolProbity* (Williams et al., 2018).

††Clashscore is the number of serious steric overlaps (>0.4) per 1000 atoms (Williams et al., 2018).

Table 4 Sequence coverage of trypsin digested CmLIK-KD samples

Protein		CmLIK-KD		
Variant		WT	D690S	Hairpin
Sequence coverage [%]	32°C	68.88	72.87	76.04
	45°C	75.53	76.60	63.02
	49°C	72.87	63.83	77.08

Table 5 Sequence coverage of trypsin and elastase digested CmSC35 32°C samples

Protein		CmSC35		
Sample		WT, 32°C	D690S, 32°C	Hairpin, 32°C
Sequence coverage [%]	trypsin	55.86	55.86	55.86
	elastase	62.16	66.67	87.84

$$T_{50} = -\left(\ln\left(\frac{Top - Bottom}{50 - Bottom} - 1\right) * Slope - V50\right) \tag{1}$$

$$dT_{50} = sqrt\left(\left(dTop * \left(-\left(\frac{\frac{1}{50 - Bottom}}{\frac{Top - Bottom}{50 - Bottom} - 1} * Slope\right)\right)\right)^2 + \left(dBottom * \left(\frac{\frac{1}{50 - Bottom} - \frac{Top - Bottom}{(50 - Bottom)^2}}{\frac{Top - Bottom}{50 - Bottom} - 1} * Slope\right)\right)^2 + \left(\left(dSlope * \left(-\ln\left(\frac{Top - Bottom}{50 - Bottom} - 1\right)\right)\right)^2 + \left(dV50 * (1)\right)^2\right)\right) \tag{2}$$

References

Afonine, P.V., Grosse-Kunstleve, R.W., Echols, N., Headd, J.J., Moriarty, N.W., Mustyakimov, M., Terwilliger, T.C., Urzhumtsev, A., Zwart, P.H., and Adams, P.D. (2012). Towards automated crystallographic structure refinement with phenix.refine. Acta crystallographica. Section D, Biological crystallography *68*, 352-367. https://doi.org/10.1107/S0907444912001308.

Aitken, A., and Learmonth, M. (2009). Estimation of Disulfide Bonds Using Ellman's Reagent. In The protein protocols handbook, J.M. Walker, ed. (New York, NY: Humana Press), pp. 1053–1055.

Altschul, S.F., Gish, W., Miller, W., Myers, E.W., and Lipman, D.J. (1990). Basic local alignment search tool. Journal of molecular biology *215*, 403-410. https://doi.org/10.1016/S0022-2836(05)80360-2.

Arnesano, F., Banci, L., Bertini, I., Mangani, S., and Thompsett, A.R. (2003). A redox switch in CopC: an intriguing copper trafficking protein that binds copper(I) and copper(II) at different sites. Proceedings of the National Academy of Sciences of the United States of America *100*, 3814-3819. https://doi.org/10.1073/pnas.0636904100.

Artarini, A., Meyer, M., Shin, Y.J., Huber, K., Hilz, N., Bracher, F., Eros, D., Orfi, L., Keri, G., and Goedert, S., et al. (2019). Regulation of influenza A virus mRNA splicing by CLK1. Antiviral research *168*, 187-196. https://doi.org/10.1016/j.antiviral.2019.06.003.

Ashkenazy, H., Penn, O., Doron-Faigenboim, A., Cohen, O., Cannarozzi, G., Zomer, O., and Pupko, T. (2012). FastML: a web server for probabilistic reconstruction of ancestral sequences. Nucleic acids research *40*, W580-4. https://doi.org/10.1093/nar/gks498.

Aubol, B.E., Keshwani, M.M., Fattet, L., and Adams, J.A. (2018). Mobilization of a splicing factor through a nuclear kinase-kinase complex. The Biochemical journal *475*, 677-690. https://doi.org/10.1042/BCJ20170672.

Aubol, B.E., Plocinik, R.M., Keshwani, M.M., McGlone, M.L., Hagopian, J.C., Ghosh, G., Fu, X.-D., and Adams, J.A. (2014). N-terminus of the protein kinase CLK1 induces SR protein

hyperphosphorylation. The Biochemical journal *462*, 143-152. https://doi.org/10.1042/BJ20140494.

Aubol, B.E., Wu, G., Keshwani, M.M., Movassat, M., Fattet, L., Hertel, K.J., Fu, X.-D., and Adams, J.A. (2016). Release of SR Proteins from CLK1 by SRPK1: A Symbiotic Kinase System for Phosphorylation Control of Pre-mRNA Splicing. Molecular cell *63*, 218-228. https://doi.org/10.1016/j.molcel.2016.05.034.

Barbosa-Morais, N.L., Irimia, M., Pan, Q., Xiong, H.Y., Gueroussov, S., Lee, L.J., Slobodeniuc, V., Kutter, C., Watt, S., and Colak, R., et al. (2012). The evolutionary landscape of alternative splicing in vertebrate species. Science (New York, N.Y.) *338*, 1587-1593. https://doi.org/10.1126/science.1230612.

Bell-Pedersen, D., Shinohara, M.L., Loros, J.J., and Dunlap, J.C. (1996). Circadian clock-controlled genes isolated from Neurospora crassa are late night- to early morning-specific. Proceedings of the National Academy of Sciences of the United States of America *93*, 13096-13101. https://doi.org/10.1073/pnas.93.23.13096.

Bender, J., and Fink, G.R. (1994). AFC1, a LAMMER kinase from Arabidopsis thaliana, activates STE12-dependent processes in yeast. Proceedings of the National Academy of Sciences of the United States of America *91*, 12105-12109. https://doi.org/10.1073/pnas.91.25.12105.

Bennett, L., Melchers, B., and Proppe, B. (2020). Curta: A General-purpose High-Performance Computer at ZEDAT, Freie Universität Berlin (Freie Universität Berlin).

Bernardo-García, S., Lucas, M. de, Martínez, C., Espinosa-Ruiz, A., Davière, J.-M., and Prat, S. (2014). BR-dependent phosphorylation modulates PIF4 transcriptional activity and shapes diurnal hypocotyl growth. Genes & development *28*, 1681-1694. https://doi.org/10.1101/gad.243675.114.

Bingham, J., and Sudarsanam, S. (2000). Visualizing large hierarchical clusters in hyperbolic space. Bioinformatics (Oxford, England) *16*, 660-661. https://doi.org/10.1093/bioinformatics/16.7.660.

Bino, G., Kingsford, R.T., Archer, M., Connolly, J.H., Day, J., Dias, K., Goldney, D., Gongora, J., Grant, T., and Griffiths, J., et al. (2019). The platypus: evolutionary history, biology, and

an uncertain future. Journal of Mammalogy *100*, 308-327. https://doi.org/10.1093/jmammal/gyz058.

Black, C.S., Garside, E.L., MacMillan, A.M., and Rader, S.D. (2016). Conserved structure of Snu13 from the highly reduced spliceosome of Cyanidioschyzon merolae. Protein science : a publication of the Protein Society *25*, 911-916. https://doi.org/10.1002/pro.2894.

Black, D.L. (2003). Mechanisms of alternative pre-messenger RNA splicing. Annual review of biochemistry *72*, 291-336. https://doi.org/10.1146/annurev.biochem.72.121801.161720.

Blackie, A.C., and Foley, D.J. (2022). Exploring the roles of the Cdc2-like kinases in cancers. Bioorganic & medicinal chemistry *70*, 116914. https://doi.org/10.1016/j.bmc.2022.116914.

Borjigin, J., Payne, A.S., Deng, J., Li, X., Wang, M.M., Ovodenko, B., Gitlin, J.D., and Snyder, S.H. (1999). A novel pineal night-specific ATPase encoded by the Wilson disease gene. The Journal of neuroscience : the official journal of the Society for Neuroscience *19*, 1018-1026. https://doi.org/10.1523/JNEUROSCI.19-03-01018.1999.

Boucher, L., Ouzounis, C.A., Enright, A.J., and Blencowe, B.J. (2001). A genome-wide survey of RS domain proteins. RNA *7*, 1693-1701.

Buhr, E.D., Yoo, S.-H., and Takahashi, J.S. (2010). Temperature as a universal resetting cue for mammalian circadian oscillators. Science (New York, N.Y.) *330*, 379-385. https://doi.org/10.1126/science.1195262.

Buljan, M., Chalancon, G., Eustermann, S., Wagner, G.P., Fuxreiter, M., Bateman, A., and Babu, M.M. (2012). Tissue-specific splicing of disordered segments that embed binding motifs rewires protein interaction networks. Molecular cell *46*, 871-883. https://doi.org/10.1016/j.molcel.2012.05.039.

Bullock, A.N., Das, S., Debreczeni, J.E., Rellos, P., Fedorov, O., Niesen, F.H., Guo, K., Papagrigoriou, E., Amos, A.L., and Cho, S., et al. (2009). Kinase domain insertions define distinct roles of CLK kinases in SR protein phosphorylation. Structure (London, England : 1993) *17*, 352-362. https://doi.org/10.1016/j.str.2008.12.023.

Busch, A., Nield, J., and Hippler, M. (2010). The composition and structure of photosystem I-associated antenna from Cyanidioschyzon merolae. The Plant journal : for cell and molecular biology *62*, 886-897. https://doi.org/10.1111/j.1365-313X.2010.04202.x.

Cáceres, J.F., Misteli, T., Screaton, G.R., Spector, D.L., and Krainer, A.R. (1997). Role of the modular domains of SR proteins in subnuclear localization and alternative splicing specificity. The Journal of cell biology *138*, 225-238. https://doi.org/10.1083/jcb.138.2.225.

Cao, W., Jamison, S.F., and Garcia-Blanco, M.A. (1997). Both phosphorylation and dephosphorylation of ASF/SF2 are required for pre-mRNA splicing in vitro. RNA *3*, 1456-1467.

Capel, B. (2017). Vertebrate sex determination: evolutionary plasticity of a fundamental switch. Nature reviews. Genetics *18*, 675-689. https://doi.org/10.1038/nrg.2017.60.

Chae, K., Isaacs, C.G., Reeves, P.H., Maloney, G.S., Muday, G.K., Nagpal, P., and Reed, J.W. (2012). Arabidopsis SMALL AUXIN UP RNA63 promotes hypocotyl and stamen filament elongation. The Plant journal : for cell and molecular biology *71*, 684-697. https://doi.org/10.1111/j.1365-313X.2012.05024.x.

Chambers, M.C., Maclean, B., Burke, R., Amodei, D., Ruderman, D.L., Neumann, S., Gatto, L., Fischer, B., Pratt, B., and Egertson, J., et al. (2012). A cross-platform toolkit for mass spectrometry and proteomics. Nature biotechnology *30*, 918-920. https://doi.org/10.1038/nbt.2377.

Cohen-Eliav, M., Golan-Gerstl, R., Siegfried, Z., Andersen, C.L., Thorsen, K., Ørntoft, T.F., Mu, D., and Karni, R. (2013). The splicing factor SRSF6 is amplified and is an oncoprotein in lung and colon cancers. The Journal of pathology *229*, 630-639. https://doi.org/10.1002/path.4129.

Cohu, C.M., and Pilon, M. (2007). Regulation of superoxide dismutase expression by copper availability. Physiologia plantarum *129*, 747-755. https://doi.org/10.1111/j.1399-3054.2007.00879.x.

Colgan, D.F., and Manley, J.L. (1997). Mechanism and regulation of mRNA polyadenylation. Genes & development *11*, 2755-2766. https://doi.org/10.1101/gad.11.21.2755.

Colwill, K., Feng, L.L., Yeakley, J.M., Gish, G.D., Cáceres, J.F., Pawson, T., and Fu, X.D. (1996a). SRPK1 and Clk/Sty protein kinases show distinct substrate specificities for serine/arginine-rich splicing factors. The Journal of biological chemistry *271*, 24569-24575. https://doi.org/10.1074/jbc.271.40.24569.

Colwill, K., Pawson, T., Andrews, B., Prasad, J., Manley, J.L., Bell, J.C., and Duncan, P.I. (1996b). The Clk/Sty protein kinase phosphorylates SR splicing factors and regulates their intranuclear distribution. The EMBO Journal *15*, 265-275.

Crawford, A.J., McLachlan, D.H., Hetherington, A.M., and Franklin, K.A. (2012). High temperature exposure increases plant cooling capacity. Current biology : CB *22*, R396-7. https://doi.org/10.1016/j.cub.2012.03.044.

Crawshaw, L.I., Johnston, M.H., and Lemons, D.E. (1980). Acclimation, temperature selection, and heat exchange in the turtle, Chrysemys scripta. The American journal of physiology *238*, R443-6. https://doi.org/10.1152/ajpregu.1980.238.5.R443.

Crezee, J., Franken, N.A.P., and Oei, A.L. (2021). Hyperthermia-Based Anti-Cancer Treatments. Cancers *13*. https://doi.org/10.3390/cancers13061240.

David, C.J., and Manley, J.L. (2010). Alternative pre-mRNA splicing regulation in cancer: pathways and programs unhinged. Genes & development *24*, 2343-2364. https://doi.org/10.1101/gad.1973010.

Derman, A.I., Prinz, W.A., Belin, D., and Beckwith, J. (1993). Mutations that allow disulfide bond formation in the cytoplasm of Escherichia coli. Science (New York, N.Y.) *262*, 1744-1747. https://doi.org/10.1126/science.8259521.

Deshmukh, V., O'Green, A.L., Bossard, C., Seo, T., Lamangan, L., Ibanez, M., Ghias, A., Lai, C., Do, L., and Cho, S., et al. (2019). Modulation of the Wnt pathway through inhibition of CLK2 and DYRK1A by lorecivivint as a novel, potentially disease-modifying approach for knee osteoarthritis treatment. Osteoarthritis and cartilage *27*, 1347-1360. https://doi.org/10.1016/j.joca.2019.05.006.

Deveson, I.W., Holleley, C.E., Blackburn, J., Marshall Graves, J.A., Mattick, J.S., Waters, P.D., and Georges, A. (2017). Differential intron retention in Jumonji chromatin modifier genes is implicated in reptile temperature-dependent sex determination. Science advances *3*, e1700731. https://doi.org/10.1126/sciadv.1700731.

Diederichs, K., and Karplus, P.A. (1997). Improved R-factors for diffraction data analysis in macromolecular crystallography. Nature structural biology *4*, 269-275. https://doi.org/10.1038/nsb0497-269.

Ding, J.-H., Xu, X., Yang, D., Chu, P.-H., Dalton, N.D., Ye, Z., Yeakley, J.M., Cheng, H., Xiao, R.-P., and Ross, J., et al. (2004). Dilated cardiomyopathy caused by tissue-specific ablation of SC35 in the heart. The EMBO Journal *23*, 885-896. https://doi.org/10.1038/sj.emboj.7600054.

Ding, J.-H., Zhong, X.-Y., Hagopian, J.C., Cruz, M.M., Ghosh, G., Feramisco, J., Adams, J.A., and Fu, X.-D. (2006). Regulated cellular partitioning of SR protein-specific kinases in mammalian cells. Molecular biology of the cell *17*, 876-885. https://doi.org/10.1091/mbc.e05-10-0963.

Duncan, P.I., Stojdl, D.F., Marius, R.M., Scheit, K.H., and Bell, J.C. (1998). The Clk2 and Clk3 dual-specificity protein kinases regulate the intranuclear distribution of SR proteins and influence pre-mRNA splicing. Experimental cell research *241*, 300-308. https://doi.org/10.1006/excr.1998.4083.

Edmond, V., Moysan, E., Khochbin, S., Matthias, P., Brambilla, C., Brambilla, E., Gazzeri, S., and Eymin, B. (2011). Acetylation and phosphorylation of SRSF2 control cell fate decision in response to cisplatin. The EMBO Journal *30*, 510-523. https://doi.org/10.1038/emboj.2010.333.

Emsley, P., Lohkamp, B., Scott, W.G., and Cowtan, K. (2010). Features and development of Coot. Acta crystallographica. Section D, Biological crystallography *66*, 486-501. https://doi.org/10.1107/S0907444910007493.

Eperon, L.P., Graham, I.R., Griffiths, A.D., and Eperon, I.C. (1988). Effects of RNA secondary structure on alternative splicing of pre-mRNA: is folding limited to a region behind the transcribing RNA polymerase? Cell *54*, 393-401. https://doi.org/10.1016/0092-8674(88)90202-4.

Erwin, J.E., Heins, R.D., and Karlsson, M.G. (1989). THERMOMORPHOGENESIS IN LILIUM LONGIFLORUM. American J of Botany *76*, 47-52. https://doi.org/10.1002/j.1537-2197.1989.tb11283.x.

Farner, D.S., Chivers, N., and Riney, T. (1956). The Body Temperatures of the North Island Kiwis. Emu - Austral Ornithology *56*, 199-206. https://doi.org/10.1071/MU956199.

Fedorov, O., Huber, K., Eisenreich, A., Filippakopoulos, P., King, O., Bullock, A.N., Szklarczyk, D., Jensen, L.J., Fabbro, D., and Trappe, J., et al. (2011). Specific CLK inhibitors from a novel chemotype for regulation of alternative splicing. Chemistry & biology *18*, 67-76. https://doi.org/10.1016/j.chembiol.2010.11.009.

Ferguson, M.W., and Joanen, T. (1982). Temperature of egg incubation determines sex in Alligator mississippiensis. Nature *296*, 850-853. https://doi.org/10.1038/296850a0.

Foreman, J., Johansson, H., Hornitschek, P., Josse, E.-M., Fankhauser, C., and Halliday, K.J. (2011). Light receptor action is critical for maintaining plant biomass at warm ambient temperatures. The Plant journal : for cell and molecular biology *65*, 441-452. https://doi.org/10.1111/j.1365-313X.2010.04434.x.

Franklin, K.A., Lee, S.H., Patel, D., Kumar, S.V., Spartz, A.K., Gu, C., Ye, S., Yu, P., Breen, G., and Cohen, J.D., et al. (2011). Phytochrome-interacting factor 4 (PIF4) regulates auxin biosynthesis at high temperature. Proceedings of the National Academy of Sciences of the United States of America *108*, 20231-20235. https://doi.org/10.1073/pnas.1110682108.

Fu, X.D., and Maniatis, T. (1992). Isolation of a complementary DNA that encodes the mammalian splicing factor SC35. Science (New York, N.Y.) *256*, 535-538. https://doi.org/10.1126/science.1373910.

Fu, X.-D., and Ares, M. (2014). Context-dependent control of alternative splicing by RNA-binding proteins. Nature reviews. Genetics *15*, 689-701. https://doi.org/10.1038/nrg3778.

Gallo, R., Rai, A.K., McIntyre, A.B.R., Meyer, K., and Pelkmans, L. (2023). DYRK3 enables secretory trafficking by maintaining the liquid-like state of ER exit sites. Developmental cell *58*, 1880-1897.e11. https://doi.org/10.1016/j.devcel.2023.08.005.

Gao, K., Masuda, A., Matsuura, T., and Ohno, K. (2008). Human branch point consensus sequence is yUnAy. Nucleic acids research *36*, 2257-2267. https://doi.org/10.1093/nar/gkn073.

García-Blanco, M.A., Jamison, S.F., and Sharp, P.A. (1989). Identification and purification of a 62,000-dalton protein that binds specifically to the polypyrimidine tract of introns. Genes & development *3*, 1874-1886. https://doi.org/10.1101/gad.3.12a.1874.

García-Sacristán, A., Fernández-Nestosa, M.J., Hernández, P., Schvartzman, J.B., and Krimer, D.B. (2005). Protein kinase clk/STY is differentially regulated during erythroleukemia cell differentiation: a bias toward the skipped splice variant characterizes postcommitment stages. Cell research *15*, 495-503. https://doi.org/10.1038/sj.cr.7290319.

Gautrey, H.L., and Tyson-Capper, A.J. (2012). Regulation of Mcl-1 by SRSF1 and SRSF5 in cancer cells. PloS one *7*, e51497. https://doi.org/10.1371/journal.pone.0051497.

George, A., Aubol, B.E., Fattet, L., and Adams, J.A. (2019). Disordered protein interactions for an ordered cellular transition: Cdc2-like kinase 1 is transported to the nucleus via its Ser-Arg protein substrate. The Journal of biological chemistry *294*, 9631-9641. https://doi.org/10.1074/jbc.RA119.008463.

Giannakouros, T., Nikolakaki, E., Mylonis, I., and Georgatsou, E. (2011). Serine-arginine protein kinases: a small protein kinase family with a large cellular presence. The FEBS journal *278*, 570-586. https://doi.org/10.1111/j.1742-4658.2010.07987.x.

Glatz, D.C., Rujescu, D., Tang, Y., Berendt, F.J., Hartmann, A.M., Faltraco, F., Rosenberg, C., Hulette, C., Jellinger, K., and Hampel, H., et al. (2006). The alternative splicing of tau exon 10 and its regulatory proteins CLK2 and TRA2-BETA1 changes in sporadic Alzheimer's disease. Journal of neurochemistry *96*, 635-644. https://doi.org/10.1111/j.1471-4159.2005.03552.x.

Golovanov, A.P., Hautbergue, G.M., Wilson, S.A., and Lian, L.-Y. (2004). A simple method for improving protein solubility and long-term stability. Journal of the American Chemical Society *126*, 8933-8939. https://doi.org/10.1021/ja049297h.

Golovkin, M., and Reddy, A.S. (1999). An SC35-like protein and a novel serine/arginine-rich protein interact with Arabidopsis U1-70K protein. The Journal of biological chemistry *274*, 36428-36438. https://doi.org/10.1074/jbc.274.51.36428.

Gout, S., Brambilla, E., Boudria, A., Drissi, R., Lantuejoul, S., Gazzeri, S., and Eymin, B. (2012). Abnormal expression of the pre-mRNA splicing regulators SRSF1, SRSF2, SRPK1 and SRPK2 in non small cell lung carcinoma. PloS one *7*, e46539. https://doi.org/10.1371/journal.pone.0046539.

Grant, T.R. (1983). Body Temperatures of Free-Ranging Platypuses, Ornithorhynchus anatinus (Monotremata), with Observations on their Use of Burrows. Aust. J. Zool. *31*, 117. https://doi.org/10.1071/zo9830117.

Graveley, B.R. (2001). Alternative splicing: increasing diversity in the proteomic world. Trends in genetics : TIG *17*, 100-107. https://doi.org/10.1016/S0168-9525(00)02176-4.

Gray, W.M., Ostin, A., Sandberg, G., Romano, C.P., and Estelle, M. (1998). High temperature promotes auxin-mediated hypocotyl elongation in Arabidopsis. Proceedings of the National Academy of Sciences of the United States of America *95*, 7197-7202. https://doi.org/10.1073/pnas.95.12.7197.

Gui, J.F., Lane, W.S., and Fu, X.D. (1994a). A serine kinase regulates intracellular localization of splicing factors in the cell cycle. Nature *369*, 678-682. https://doi.org/10.1038/369678a0.

Gui, J.F., Tronchère, H., Chandler, S.D., and Fu, X.D. (1994b). Purification and characterization of a kinase specific for the serine- and arginine-rich pre-mRNA splicing factors. Proceedings of the National Academy of Sciences of the United States of America *91*, 10824-10828. https://doi.org/10.1073/pnas.91.23.10824.

Haltenhof, T. (2020). Cdc2-like kinases represent evolutionarily adapted temperature-sensors, which globally control alternative splicing and gene expression.

Haltenhof, T., Kotte, A., Bortoli, F. de, Schiefer, S., Meinke, S., Emmerichs, A.-K., Petermann, K.K., Timmermann, B., Imhof, P., and Franz, A., et al. (2020). A Conserved Kinase-Based Body-Temperature Sensor Globally Controls Alternative Splicing and Gene Expression. Molecular cell *78*, 57-69.e4. https://doi.org/10.1016/j.molcel.2020.01.028.

Hayes, G.M., Carrigan, P.E., and Miller, L.J. (2007). Serine-arginine protein kinase 1 overexpression is associated with tumorigenic imbalance in mitogen-activated protein kinase pathways in breast, colonic, and pancreatic carcinomas. Cancer research *67*, 2072-2080. https://doi.org/10.1158/0008-5472.CAN-06-2969.

Hiller, M., Zhang, Z., Backofen, R., and Stamm, S. (2007). Pre-mRNA secondary structures influence exon recognition. PLOS Genetics *3*, e204. https://doi.org/10.1371/journal.pgen.0030204.

Hollingsworth, S.A., and Dror, R.O. (2018). Molecular Dynamics Simulation for All. Neuron *99*, 1129-1143. https://doi.org/10.1016/j.neuron.2018.08.011.

Howard, C.J., Hanson-Smith, V., Kennedy, K.J., Miller, C.J., Lou, H.J., Johnson, A.D., Turk, B.E., and Holt, L.J. (2014). Ancestral resurrection reveals evolutionary mechanisms of kinase plasticity. eLife *3*. https://doi.org/10.7554/eLife.04126.

Huang, J., Wang, L., Shen, Y., Zhang, S., Zhou, Y., Du, J., Ma, X., Liu, Y., Liang, D., and Shi, D., et al. (2022). CDC-like kinase 4 deficiency contributes to pathological cardiac hypertrophy by modulating NEXN phosphorylation. Nature communications *13*, 4433. https://doi.org/10.1038/s41467-022-31996-9.

Huang, Y., and Steitz, J.A. (2005). SRprises along a messenger's journey. Molecular cell *17*, 613-615. https://doi.org/10.1016/j.molcel.2005.02.020.

Huang, Y., Yario, T.A., and Steitz, J.A. (2004). A molecular link between SR protein dephosphorylation and mRNA export. Proceedings of the National Academy of Sciences of the United States of America *101*, 9666-9670. https://doi.org/10.1073/pnas.0403533101.

Jain, P., Karthikeyan, C., Moorthy, N.S.H.N., Waiker, D.K., Jain, A.K., and Trivedi, P. (2014). Human CDC2-like kinase 1 (CLK1): a novel target for Alzheimer's disease. Current drug targets *15*, 539-550. https://doi.org/10.2174/1389450115666140226112321.

Jang, S.-W., Yang, S.-J., Ehlén, A., Dong, S., Khoury, H., Chen, J., Persson, J.L., and Ye, K. (2008). Serine/arginine protein-specific kinase 2 promotes leukemia cell proliferation by phosphorylating acinus and regulating cyclin A1. Cancer research *68*, 4559-4570. https://doi.org/10.1158/0008-5472.CAN-08-0021.

Janni, M., Maestri, E., Gullì, M., Marmiroli, M., and Marmiroli, N. (2023). Plant responses to climate change, how global warming may impact on food security: a critical review. Frontiers in plant science *14*, 1297569. https://doi.org/10.3389/fpls.2023.1297569.

Jia, R., Li, C., McCoy, J.P., Deng, C.-X., and Zheng, Z.-M. (2010). SRp20 is a proto-oncogene critical for cell proliferation and tumor induction and maintenance. International journal of biological sciences *6*, 806-826. https://doi.org/10.7150/ijbs.6.806.

Jiang, K., Patel, N.A., Watson, J.E., Apostolatos, H., Kleiman, E., Hanson, O., Hagiwara, M., and Cooper, D.R. (2009). Akt2 regulation of Cdc2-like kinases (Clk/Sty), serine/arginine-rich (SR) protein phosphorylation, and insulin-induced alternative splicing of PKCbetaII messenger ribonucleic acid. Endocrinology *150*, 2087-2097. https://doi.org/10.1210/en.2008-0818.

Johnson, L.N., Noble, M.E., and Owen, D.J. (1996). Active and inactive protein kinases: structural basis for regulation. Cell *85*, 149-158. https://doi.org/10.1016/S0092-8674(00)81092-2.

Jumaa, H., Wei, G., and Nielsen, P.J. (1999). Blastocyst formation is blocked in mouse embryos lacking the splicing factor SRp20. Current biology : CB *9*, 899-902. https://doi.org/10.1016/s0960-9822(99)80394-7.

Jumper, J., Evans, R., Pritzel, A., Green, T., Figurnov, M., Ronneberger, O., Tunyasuvunakool, K., Bates, R., Žídek, A., and Potapenko, A., et al. (2021). Highly accurate protein structure prediction with AlphaFold. Nature *596*, 583-589. https://doi.org/10.1038/s41586-021-03819-2.

Kang, W.-H., Park, Y.-H., and Park, H.-M. (2010). The LAMMER kinase homolog, Lkh1, regulates Tup transcriptional repressors through phosphorylation in Schizosaccharomyces pombe. The Journal of biological chemistry *285*, 13797-13806. https://doi.org/10.1074/jbc.M110.113555.

Karni, R., Stanchina, E. de, Lowe, S.W., Sinha, R., Mu, D., and Krainer, A.R. (2007). The gene encoding the splicing factor SF2/ASF is a proto-oncogene. Nature structural & molecular biology *14*, 185-193. https://doi.org/10.1038/nsmb1209.

Karplus, P.A., and Diederichs, K. (2012). Linking crystallographic model and data quality. Science (New York, N.Y.) *336*, 1030-1033. https://doi.org/10.1126/science.1218231.

Keil, B. (1992). Specificity of Proteolysis (Berlin, Heidelberg: Springer Berlin Heidelberg).

Keil, G., Cummings, E., and Magalhães, J.P. de (2015). Being cool: how body temperature influences ageing and longevity. Biogerontology *16*, 383-397. https://doi.org/10.1007/s10522-015-9571-2.

Keshwani, M.M., Hailey, K.L., Aubol, B.E., Fattet, L., McGlone, M.L., Jennings, P.A., and Adams, J.A. (2015). Nuclear protein kinase CLK1 uses a non-traditional docking mechanism to select physiological substrates. The Biochemical journal *472*, 329-338. https://doi.org/10.1042/BJ20150903.

Knape, M.J., and Herberg, F.W. (2017). Metal coordination in kinases and pseudokinases. Biochemical Society transactions *45*, 653-663. https://doi.org/10.1042/BST20160327.

Kohtz, J.D., Jamison, S.F., Will, C.L., Zuo, P., Lührmann, R., Garcia-Blanco, M.A., and Manley, J.L. (1994). Protein-protein interactions and 5'-splice-site recognition in mammalian mRNA precursors. Nature *368*, 119-124. https://doi.org/10.1038/368119a0.

Koini, M.A., Alvey, L., Allen, T., Tilley, C.A., Harberd, N.P., Whitelam, G.C., and Franklin, K.A. (2009). High temperature-mediated adaptations in plant architecture require the bHLH transcription factor PIF4. Current biology : CB *19*, 408-413. https://doi.org/10.1016/j.cub.2009.01.046.

Kong, A.T., Leprevost, F.V., Avtonomov, D.M., Mellacheruvu, D., and Nesvizhskii, A.I. (2017). MSFragger: ultrafast and comprehensive peptide identification in mass spectrometry-based proteomics. Nature methods *14*, 513-520. https://doi.org/10.1038/nmeth.4256.

Kornev, A.P., Haste, N.M., Taylor, S.S., and Eyck, L.F. ten (2006). Surface comparison of active and inactive protein kinases identifies a conserved activation mechanism. Proceedings of the National Academy of Sciences of the United States of America *103*, 17783-17788. https://doi.org/10.1073/pnas.0607656103.

Kropat, J., Tottey, S., Birkenbihl, R.P., Depège, N., Huijser, P., and Merchant, S. (2005). A regulator of nutritional copper signaling in Chlamydomonas is an SBP domain protein

that recognizes the GTAC core of copper response element. Proceedings of the National Academy of Sciences of the United States of America *102*, 18730-18735. https://doi.org/10.1073/pnas.0507693102.

Krug, M., Weiss, M.S., Heinemann, U., and Mueller, U. (2012). XDSAPP : a graphical user interface for the convenient processing of diffraction data using XDS. Journal of applied crystallography *45*, 568-572. https://doi.org/10.1107/S0021889812011715.

Kuroiwa, T. (1998). The primitive red algae Cyanidium caldarium and Cyanidioschyzon merolae as model system for investigating the dividing apparatus of mitochondria and plastids. Bioessays *20*, 344-354. https://doi.org/10.1002/(SICI)1521-1878(199804)20:4<344::AID-BIES11>3.0.CO;2-2.

Kuroyanagi, H., Kimura, T., Wada, K., Hisamoto, N., Matsumoto, K., and Hagiwara, M. (2000). SPK-1, a C. elegans SR protein kinase homologue, is essential for embryogenesis and required for germline development. Mechanisms of development *99*, 51-64. https://doi.org/10.1016/s0925-4773(00)00477-9.

La Mata, M. de, Alonso, C.R., Kadener, S., Fededa, J.P., Blaustein, M., Pelisch, F., Cramer, P., Bentley, D., and Kornblihtt, A.R. (2003). A slow RNA polymerase II affects alternative splicing in vivo. Molecular cell *12*, 525-532. https://doi.org/10.1016/j.molcel.2003.08.001.

Lakbub, J.C., Shipman, J.T., and Desaire, H. (2018). Recent mass spectrometry-based techniques and considerations for disulfide bond characterization in proteins. Analytical and bioanalytical chemistry *410*, 2467-2484. https://doi.org/10.1007/s00216-017-0772-1.

Lander, E.S., Linton, L.M., Birren, B., Nusbaum, C., Zody, M.C., Baldwin, J., Devon, K., Dewar, K., Doyle, M., and FitzHugh, W., et al. (2001). Initial sequencing and analysis of the human genome. Nature *409*, 860-921. https://doi.org/10.1038/35057062.

Lasho, T.L., Jimma, T., Finke, C.M., Patnaik, M., Hanson, C.A., Ketterling, R.P., Pardanani, A., and Tefferi, A. (2012). SRSF2 mutations in primary myelofibrosis: significant clustering with IDH mutations and independent association with inferior overall and leukemia-free survival. Blood *120*, 4168-4171. https://doi.org/10.1182/blood-2012-05-429696.

LaVallie, E.R., DiBlasio, E.A., Kovacic, S., Grant, K.L., Schendel, P.F., and McCoy, J.M. (1993). A thioredoxin gene fusion expression system that circumvents inclusion body formation in the E. coli cytoplasm. Bio/technology (Nature Publishing Company) *11*, 187-193. https://doi.org/10.1038/nbt0293-187.

Lee, J.Y., Yun, J.-S., Kim, W.-K., Chun, H.-S., Jin, H., Cho, S., and Chang, J.H. (2019). Structural Basis for the Selective Inhibition of Cdc2-Like Kinases by CX-4945. BioMed research international *2019*, 6125068. https://doi.org/10.1155/2019/6125068.

Léger, J., Kempf, M., Lee, G., and Brandt, R. (1997). Conversion of serine to aspartate imitates phosphorylation-induced changes in the structure and function of microtubule-associated protein tau. The Journal of biological chemistry *272*, 8441-8446. https://doi.org/10.1074/jbc.272.13.8441.

Li, A., Sowder, R.C., Henderson, L.E., Moore, S.P., Garfinkel, D.J., and Fisher, R.J. (2001). Chemical cleavage at aspartyl residues for protein identification. Analytical chemistry *73*, 5395-5402. https://doi.org/10.1021/ac010619z.

Li, P., Carter, G., Romero, J., Gower, K.M., Watson, J., Patel, N.A., and Cooper, D.R. (2013). Clk/STY (cdc2-like kinase 1) and Akt regulate alternative splicing and adipogenesis in 3T3-L1 pre-adipocytes. PloS one *8*, e53268. https://doi.org/10.1371/journal.pone.0053268.

Li, Z., Jaroszewski, L., Iyer, M., Sedova, M., and Godzik, A. (2020). FATCAT 2.0: towards a better understanding of the structural diversity of proteins. Nucleic acids research *48*, W60-W64. https://doi.org/10.1093/nar/gkaa443.

Liebschner, D., Afonine, P.V., Baker, M.L., Bunkóczi, G., Chen, V.B., Croll, T.I., Hintze, B., Hung, L.W., Jain, S., and McCoy, A.J., et al. (2019). Macromolecular structure determination using X-rays, neutrons and electrons: recent developments in Phenix. Acta crystallographica. Section D, Structural biology *75*, 861-877. https://doi.org/10.1107/S2059798319011471.

Liebschner, D., Afonine, P.V., Moriarty, N.W., Poon, B.K., Sobolev, O.V., Terwilliger, T.C., and Adams, P.D. (2017). Polder maps: improving OMIT maps by excluding bulk solvent. Acta crystallographica. Section D, Structural biology *73*, 148-157. https://doi.org/10.1107/S2059798316018210.

Lin, J., Shi, J., Zhang, Z., Zhong, B., and Zhu, Z. (2022). Plant AFC2 kinase desensitizes thermomorphogenesis through modulation of alternative splicing. iScience *25*, 104051. https://doi.org/10.1016/j.isci.2022.104051.

Lin, S., Coutinho-Mansfield, G., Wang, D., Pandit, S., and Fu, X.-D. (2008). The splicing factor SC35 has an active role in transcriptional elongation. Nature structural & molecular biology *15*, 819-826. https://doi.org/10.1038/nsmb.1461.

Loh, B.J., Cullen, C.F., Vogt, N., and Ohkura, H. (2012). The conserved kinase SRPK regulates karyosome formation and spindle microtubule assembly in Drosophila oocytes. Journal of cell science *125*, 4457-4462. https://doi.org/10.1242/jcs.107979.

Long, J.C., and Caceres, J.F. (2009). The SR protein family of splicing factors: master regulators of gene expression. The Biochemical journal *417*, 15-27. https://doi.org/10.1042/BJ20081501.

Long, Y., Sou, W.H., Yung, K.W.Y., Liu, H., Wan, S.W.C., Li, Q., Zeng, C., Law, C.O.K., Chan, G.H.C., and Lau, T.C.K., et al. (2019). Distinct mechanisms govern the phosphorylation of different SR protein splicing factors. The Journal of biological chemistry *294*, 1312-1327. https://doi.org/10.1074/jbc.RA118.003392.

Loomis, R.J., Naoe, Y., Parker, J.B., Savic, V., Bozovsky, M.R., Macfarlan, T., Manley, J.L., and Chakravarti, D. (2009). Chromatin binding of SRp20 and ASF/SF2 and dissociation from mitotic chromosomes is modulated by histone H3 serine 10 phosphorylation. Molecular cell *33*, 450-461. https://doi.org/10.1016/j.molcel.2009.02.003.

Lorrain, S., Allen, T., Duek, P.D., Whitelam, G.C., and Fankhauser, C. (2008). Phytochrome-mediated inhibition of shade avoidance involves degradation of growth-promoting bHLH transcription factors. The Plant journal : for cell and molecular biology *53*, 312-323. https://doi.org/10.1111/j.1365-313X.2007.03341.x.

Los, B., Preußner, M., Eschke, K., Vidal, R.M., Abdelgawad, A., Olofsson, D., Keiper, S., Paulo-Pedro, M., Grindel, A., and Meinke, S., et al. (2022). Body temperature variation controls pre-mRNA processing and transcription of antiviral genes and SARS-CoV-2 replication. Nucleic acids research *50*, 6769-6785. https://doi.org/10.1093/nar/gkac513.

Luca, P. de, Taddei, R., and Varano, L. (1978). « Cyanidioschyzon merolae »: a new alga of thermal acidic environments. Webbia *33*, 37-44. https://doi.org/10.1080/00837792.1978.10670110.

Madeira, F., Pearce, M., Tivey, A.R.N., Basutkar, P., Lee, J., Edbali, O., Madhusoodanan, N., Kolesnikov, A., and Lopez, R. (2022). Search and sequence analysis tools services from EMBL-EBI in 2022. Nucleic acids research *50*, W276-W279. https://doi.org/10.1093/nar/gkac240.

Madhusudan, Trafny, E.A., Xuong, N.H., Adams, J.A., Eyck, L.F. ten, Taylor, S.S., and Sowadski, J.M. (1994). cAMP-dependent protein kinase: crystallographic insights into substrate recognition and phosphotransfer. Protein science : a publication of the Protein Society *3*, 176-187. https://doi.org/10.1002/pro.5560030203.

Manley, J.L., and Krainer, A.R. (2010). A rational nomenclature for serine/arginine-rich protein splicing factors (SR proteins). Genes & development *24*, 1073-1074. https://doi.org/10.1101/gad.1934910.

Manning, G., Whyte, D.B., Martinez, R., Hunter, T., and Sudarsanam, S. (2002). The protein kinase complement of the human genome. Science (New York, N.Y.) *298*, 1912-1934. https://doi.org/10.1126/science.1075762.

Martín Moyano, P., Němec, V., and Paruch, K. (2020). Cdc-Like Kinases (CLKs): Biology, Chemical Probes, and Therapeutic Potential. International Journal of Molecular Sciences *21*. https://doi.org/10.3390/ijms21207549.

Martinez, N.M., and Lynch, K.W. (2013). Control of alternative splicing in immune responses: many regulators, many predictions, much still to learn. Immunological reviews *253*, 216-236. https://doi.org/10.1111/imr.12047.

Marty, M.T., Baldwin, A.J., Marklund, E.G., Hochberg, G.K.A., Benesch, J.L.P., and Robinson, C.V. (2015). Bayesian deconvolution of mass and ion mobility spectra: from binary interactions to polydisperse ensembles. Analytical chemistry *87*, 4370-4376. https://doi.org/10.1021/acs.analchem.5b00140.

Matlin, A.J., Clark, F., and Smith, C.W.J. (2005). Understanding alternative splicing: towards a cellular code. Nature reviews. Molecular cell biology *6*, 386-398. https://doi.org/10.1038/nrm1645.

Matsuzaki, M., Misumi, O., Shin-I, T., Maruyama, S., Takahara, M., Miyagishima, S.-Y., Mori, T., Nishida, K., Yagisawa, F., and Nishida, K., et al. (2004). Genome sequence of the ultrasmall unicellular red alga Cyanidioschyzon merolae 10D. Nature *428*, 653-657. https://doi.org/10.1038/nature02398.

Mayeda, A., and Krainer, A.R. (1992). Regulation of alternative pre-mRNA splicing by hnRNP A1 and splicing factor SF2. Cell *68*, 365-375. https://doi.org/10.1016/0092-8674(92)90477-t.

McCoy, A.J., Grosse-Kunstleve, R.W., Adams, P.D., Winn, M.D., Storoni, L.C., and Read, R.J. (2007). Phaser crystallographic software. Journal of applied crystallography *40*, 658-674. https://doi.org/10.1107/S0021889807021206.

McFadden, G.I., and Ralph, S.A. (2003). Dynamin: the endosymbiosis ring of power? Proceedings of the National Academy of Sciences of the United States of America *100*, 3557-3559. https://doi.org/10.1073/pnas.0831049100.

Meggendorfer, M., Roller, A., Haferlach, T., Eder, C., Dicker, F., Grossmann, V., Kohlmann, A., Alpermann, T., Yoshida, K., and Ogawa, S., et al. (2012). SRSF2 mutations in 275 cases with chronic myelomonocytic leukemia (CMML). Blood *120*, 3080-3088. https://doi.org/10.1182/blood-2012-01-404863.

Mermoud, J.E., Cohen, P.T., and Lamond, A.I. (1994). Regulation of mammalian spliceosome assembly by a protein phosphorylation mechanism. The EMBO Journal *13*, 5679-5688. https://doi.org/10.1002/j.1460-2075.1994.tb06906.x.

Michlewski, G., Sanford, J.R., and Cáceres, J.F. (2008). The splicing factor SF2/ASF regulates translation initiation by enhancing phosphorylation of 4E-BP1. Molecular cell *30*, 179-189. https://doi.org/10.1016/j.molcel.2008.03.013.

Minoda, A., Sakagami, R., Yagisawa, F., Kuroiwa, T., and Tanaka, K. (2004). Improvement of culture conditions and evidence for nuclear transformation by homologous

recombination in a red alga, Cyanidioschyzon merolae 10D. Plant & cell physiology *45*, 667-671. https://doi.org/10.1093/pcp/pch087.

Miyagishima, S.-Y., and Tanaka, K. (2021). The Unicellular Red Alga Cyanidioschyzon merolae-The Simplest Model of a Photosynthetic Eukaryote. Plant & cell physiology *62*, 926-941. https://doi.org/10.1093/pcp/pcab052.

Modi, V., and Dunbrack, R.L. (2019). A Structurally-Validated Multiple Sequence Alignment of 497 Human Protein Kinase Domains. Scientific reports *9*, 19790. https://doi.org/10.1038/s41598-019-56499-4.

Movassat, M., Forouzmand, E., Reese, F., and Hertel, K.J. (2019). Exon size and sequence conservation improves identification of splice-altering nucleotides. RNA (New York, N.Y.) *25*, 1793-1805. https://doi.org/10.1261/rna.070987.119.

Muraki, M., Ohkawara, B., Hosoya, T., Onogi, H., Koizumi, J., Koizumi, T., Sumi, K., Yomoda, J., Murray, M.V., and Kimura, H., et al. (2004). Manipulation of alternative splicing by a newly developed inhibitor of Clks. The Journal of biological chemistry *279*, 24246-24254. https://doi.org/10.1074/jbc.M314298200.

Nam, S.Y., Seo, H.H., Park, H.S., An, S., Kim, J.-Y., Yang, K.H., Kim, C.S., Jeong, M., and Jin, Y.-W. (2010). Phosphorylation of CLK2 at serine 34 and threonine 127 by AKT controls cell survival after ionizing radiation. The Journal of biological chemistry *285*, 31157-31163. https://doi.org/10.1074/jbc.M110.122044.

Naro, C., and Sette, C. (2013). Phosphorylation-mediated regulation of alternative splicing in cancer. International journal of cell biology *2013*, 151839. https://doi.org/10.1155/2013/151839.

Nayler, O., Stamm, S., and Ullrich, A. (1997). Characterization and comparison of four serine- and arginine-rich (SR) protein kinases. The Biochemical journal *326 (Pt 3)*, 693-700. https://doi.org/10.1042/bj3260693.

Němec, V., Hylsová, M., Maier, L., Flegel, J., Sievers, S., Ziegler, S., Schröder, M., Berger, B.-T., Chaikuad, A., and Valčíková, B., et al. (2019). Furo3,2-bpyridine: A Privileged Scaffold for Highly Selective Kinase Inhibitors and Effective Modulators of the Hedgehog

Pathway. Angewandte Chemie (International ed. in English) *58*, 1062-1066. https://doi.org/10.1002/anie.201810312.

Ner-Gaon, H., Halachmi, R., Savaldi-Goldstein, S., Rubin, E., Ophir, R., and Fluhr, R. (2004). Intron retention is a major phenomenon in alternative splicing in Arabidopsis. The Plant journal : for cell and molecular biology *39*, 877-885. https://doi.org/10.1111/j.1365-313X.2004.02172.x.

Neumann, A., Meinke, S., Goldammer, G., Strauch, M., Schubert, D., Timmermann, B., Heyd, F., and Preußner, M. (2020). Alternative splicing coupled mRNA decay shapes the temperature-dependent transcriptome. EMBO reports *21*, e51369. https://doi.org/10.15252/embr.202051369.

Ngo, J.C.K., Chakrabarti, S., Ding, J.-H., Velazquez-Dones, A., Nolen, B., Aubol, B.E., Adams, J.A., Fu, X.-D., and Ghosh, G. (2005). Interplay between SRPK and Clk/Sty kinases in phosphorylation of the splicing factor ASF/SF2 is regulated by a docking motif in ASF/SF2. Molecular cell *20*, 77-89. https://doi.org/10.1016/j.molcel.2005.08.025.

Ngo, J.C.K., Giang, K., Chakrabarti, S., Ma, C.-T., Huynh, N., Hagopian, J.C., Dorrestein, P.C., Fu, X.-D., Adams, J.A., and Ghosh, G. (2008). A sliding docking interaction is essential for sequential and processive phosphorylation of an SR protein by SRPK1. Molecular cell *29*, 563-576. https://doi.org/10.1016/j.molcel.2007.12.017.

Nicolardi, S., Kilgour, D.P.A., van der Burgt, Y.E.M., and Wuhrer, M. (2020). Improved N- and C-Terminal Sequencing of Proteins by Combining Positive and Negative Ion MALDI In-Source Decay Mass Spectrometry. Analytical chemistry *92*, 12429-12436. https://doi.org/10.1021/acs.analchem.0c02198.

Nikolova, D., Weber, D., Scholz, M., Bald, T., Scharsack, J.P., and Hippler, M. (2017). Temperature-Induced Remodeling of the Photosynthetic Machinery Tunes Photosynthesis in the Thermophilic Alga Cyanidioschyzon merolae. Plant physiology *174*, 35-46. https://doi.org/10.1104/pp.17.00110.

Nishikura, K. (2016). A-to-I editing of coding and non-coding RNAs by ADARs. Nature reviews. Molecular cell biology *17*, 83-96. https://doi.org/10.1038/nrm.2015.4.

Niwa, Y., Yamashino, T., and Mizuno, T. (2009). The circadian clock regulates the photoperiodic response of hypocotyl elongation through a coincidence mechanism in Arabidopsis thaliana. Plant & cell physiology *50*, 838-854. https://doi.org/10.1093/pcp/pcp028.

Nolen, B., Taylor, S., and Ghosh, G. (2004). Regulation of protein kinases; controlling activity through activation segment conformation. Molecular cell *15*, 661-675. https://doi.org/10.1016/j.molcel.2004.08.024.

Nozaki, H., Takano, H., Misumi, O., Terasawa, K., Matsuzaki, M., Maruyama, S., Nishida, K., Yagisawa, F., Yoshida, Y., and Fujiwara, T., et al. (2007). A 100%-complete sequence reveals unusually simple genomic features in the hot-spring red alga Cyanidioschyzon merolae. BMC biology *5*, 28. https://doi.org/10.1186/1741-7007-5-28.

Nusinow, D.A., Helfer, A., Hamilton, E.E., King, J.J., Imaizumi, T., Schultz, T.F., Farré, E.M., and Kay, S.A. (2011). The ELF4-ELF3-LUX complex links the circadian clock to diurnal control of hypocotyl growth. Nature *475*, 398-402. https://doi.org/10.1038/nature10182.

Ohnuma, M., Yokoyama, T., Inouye, T., Sekine, Y., and Tanaka, K. (2008). Polyethylene glycol (PEG)-mediated transient gene expression in a red alga, Cyanidioschyzon merolae 10D. Plant & cell physiology *49*, 117-120. https://doi.org/10.1093/pcp/pcm157.

Ohta, N., Sato, N., and Kuroiwa, T. (1998). Structure and organization of the mitochondrial genome of the unicellular red alga Cyanidioschyzon merolae deduced from the complete nucleotide sequence. Nucleic acids research *26*, 5190-5198. https://doi.org/10.1093/nar/26.22.5190.

Owens, A., Godbole, M., Dabydeen, D., Medeiros, L., Phatak, P., and Kandlikar, S. (2020). A Comparative Analysis of the Tumor Pathology and the Metabolic Heat Generation of Growing Malignant Tumors. In Proceedings of the ASME 18th International Conference on Nanochannels, Microchannels, and Minichannels - 2020. ICNMM 2020 : presented at ASME 2020 18th International Conference on Nanochannels, Microchannels, and Minichannels, July 13-15, 2020, online (New York, N.Y.: The American Society of Mechanical Engineers).

Pan, Q., Shai, O., Lee, L.J., Frey, B.J., and Blencowe, B.J. (2008). Deep surveying of alternative splicing complexity in the human transcriptome by high-throughput sequencing. Nature genetics *40*, 1413-1415. https://doi.org/10.1038/ng.259.

Pancha, I., Shima, H., Higashitani, N., Igarashi, K., Higashitani, A., Tanaka, K., and Imamura, S. (2019). Target of rapamycin-signaling modulates starch accumulation via glycogenin phosphorylation status in the unicellular red alga Cyanidioschyzon merolae. The Plant journal : for cell and molecular biology *97*, 485-499. https://doi.org/10.1111/tpj.14136.

Pancha, I., Takaya, K., Tanaka, K., and Imamura, S. (2021). The Unicellular Red Alga Cyanidioschyzon merolae, an Excellent Model Organism for Elucidating Fundamental Molecular Mechanisms and Their Applications in Biofuel Production. Plants (Basel, Switzerland) *10*. https://doi.org/10.3390/plants10061218.

Patnaik, M.M., Lasho, T.L., Finke, C.M., Hanson, C.A., Hodnefield, J.M., Knudson, R.A., Ketterling, R.P., Pardanani, A., and Tefferi, A. (2013). Spliceosome mutations involving SRSF2, SF3B1, and U2AF35 in chronic myelomonocytic leukemia: prevalence, clinical correlates, and prognostic relevance. American journal of hematology *88*, 201-206. https://doi.org/10.1002/ajh.23373.

Peñarrubia, L., Andrés-Colás, N., Moreno, J., and Puig, S. (2010). Regulation of copper transport in Arabidopsis thaliana: a biochemical oscillator? Journal of biological inorganic chemistry : JBIC : a publication of the Society of Biological Inorganic Chemistry *15*, 29-36. https://doi.org/10.1007/s00775-009-0591-8.

Perea-García, A., Andrés-Bordería, A., Mayo de Andrés, S., Sanz, A., Davis, A.M., Davis, S.J., Huijser, P., and Peñarrubia, L. (2016). Modulation of copper deficiency responses by diurnal and circadian rhythms in Arabidopsis thaliana. Journal of experimental botany *67*, 391-403. https://doi.org/10.1093/jxb/erv474.

Perrière, G., and Gouy, M. (1996). WWW-query: an on-line retrieval system for biological sequence banks. Biochimie *78*, 364-369. https://doi.org/10.1016/0300-9084(96)84768-7.

Plaschka, C., Newman, A.J., and Nagai, K. (2019). Structural Basis of Nuclear pre-mRNA Splicing: Lessons from Yeast. Cold Spring Harbor perspectives in biology *11*. https://doi.org/10.1101/cshperspect.a032391.

Prasad, J., and Manley, J.L. (2003). Regulation and substrate specificity of the SR protein kinase Clk/Sty. Molecular and cellular biology *23*, 4139-4149. https://doi.org/10.1128/MCB.23.12.4139-4149.2003.

Preußner, M., Goldammer, G., Neumann, A., Haltenhof, T., Rautenstrauch, P., Müller-McNicoll, M., and Heyd, F. (2017). Body Temperature Cycles Control Rhythmic Alternative Splicing in Mammals. Molecular cell *67*, 433-446.e4. https://doi.org/10.1016/j.molcel.2017.06.006.

Prinz, W.A., Aslund, F., Holmgren, A., and Beckwith, J. (1997). The role of the thioredoxin and glutaredoxin pathways in reducing protein disulfide bonds in the Escherichia coli cytoplasm. The Journal of biological chemistry *272*, 15661-15667. https://doi.org/10.1074/jbc.272.25.15661.

Prinzinger, R., Preßmar, A., and Schleucher, E. (1991). Body temperature in birds. Comparative Biochemistry and Physiology Part A: Physiology *99*, 499-506. https://doi.org/10.1016/0300-9629(91)90122-S.

Proveniers, M.C.G., and van Zanten, M. (2013). High temperature acclimation through PIF4 signaling. Trends in plant science *18*, 59-64. https://doi.org/10.1016/j.tplants.2012.09.002.

Pryor, K.D., and Leiting, B. (1997). High-level expression of soluble protein in Escherichia coli using a His6-tag and maltose-binding-protein double-affinity fusion system. Protein expression and purification *10*, 309-319. https://doi.org/10.1006/prep.1997.0759.

Quint, M., Delker, C., Franklin, K.A., Wigge, P.A., Halliday, K.J., and van Zanten, M. (2016). Molecular and genetic control of plant thermomorphogenesis. Nature plants *2*, 15190. https://doi.org/10.1038/nplants.2015.190.

Reed, R., and Cheng, H. (2005). TREX, SR proteins and export of mRNA. Current opinion in cell biology *17*, 269-273. https://doi.org/10.1016/j.ceb.2005.04.011.

Refinetti, R., and Menaker, M. (1992). The circadian rhythm of body temperature. Physiology & behavior *51*, 613-637. https://doi.org/10.1016/0031-9384(92)90188-8.

Reimer, K.A., Stark, M.R., Aguilar, L.-C., Stark, S.R., Burke, R.D., Moore, J., Fahlman, R.P., Yip, C.K., Kuroiwa, H., and Oeffinger, M., et al. (2017). The sole LSm complex in Cyanidioschyzon merolae associates with pre-mRNA splicing and mRNA degradation factors. RNA *23*, 952-967. https://doi.org/10.1261/rna.058487.116.

Riese, M., Zobell, O., Saedler, H., and Huijser, P. (2008). SBP-domain transcription factors as possible effectors of cryptochrome-mediated blue light signalling in the moss Physcomitrella patens. Planta *227*, 505-515. https://doi.org/10.1007/s00425-007-0661-5.

Rietschel, B., Arrey, T.N., Meyer, B., Bornemann, S., Schuerken, M., Karas, M., and Poetsch, A. (2009). Elastase digests: new ammunition for shotgun membrane proteomics. Molecular & cellular proteomics : MCP *8*, 1029-1043. https://doi.org/10.1074/mcp.M800223-MCP200.

Robinson, K.W. (1954). Heat tolerances of Australian monotremes and marsupials. Australian journal of biological sciences *7*, 348-360. https://doi.org/10.1071/bi9540348.

Rodgers, J.T., Haas, W., Gygi, S.P., and Puigserver, P. (2010). Cdc2-like kinase 2 is an insulin-regulated suppressor of hepatic gluconeogenesis. Cell metabolism *11*, 23-34. https://doi.org/10.1016/j.cmet.2009.11.006.

Rodriguez Gallo, M.C., Li, Q., Mehta, D., and Uhrig, R.G. (2022). Genome-scale analysis of Arabidopsis splicing-related protein kinase families reveals roles in abiotic stress adaptation. BMC plant biology *22*, 496. https://doi.org/10.1186/s12870-022-03870-9.

Rubino, J.T., and Franz, K.J. (2012). Coordination chemistry of copper proteins: how nature handles a toxic cargo for essential function. Journal of inorganic biochemistry *107*, 129-143. https://doi.org/10.1016/j.jinorgbio.2011.11.024.

Saini, C., Morf, J., Stratmann, M., Gos, P., and Schibler, U. (2012). Simulated body temperature rhythms reveal the phase-shifting behavior and plasticity of mammalian circadian oscillators. Genes & development *26*, 567-580. https://doi.org/10.1101/gad.183251.111.

Saitoh, N., Spahr, C.S., Patterson, S.D., Bubulya, P., Neuwald, A.F., and Spector, D.L. (2004). Proteomic analysis of interchromatin granule clusters. Molecular biology of the cell *15*, 3876-3890. https://doi.org/10.1091/mbc.e04-03-0253.

Sako, Y., Ninomiya, K., Okuno, Y., Toyomoto, M., Nishida, A., Koike, Y., Ohe, K., Kii, I., Yoshida, S., and Hashimoto, N., et al. (2017). Development of an orally available inhibitor of CLK1 for skipping a mutated dystrophin exon in Duchenne muscular dystrophy. Scientific reports *7*, 46126. https://doi.org/10.1038/srep46126.

Sancenón, V., Puig, S., Mira, H., Thiele, D.J., and Peñarrubia, L. (2003). Identification of a copper transporter family in Arabidopsis thaliana. Plant molecular biology *51*, 577-587. https://doi.org/10.1023/a:1022345507112.

Sanford, J.R., Gray, N.K., Beckmann, K., and Cáceres, J.F. (2004). A novel role for shuttling SR proteins in mRNA translation. Genes & development *18*, 755-768. https://doi.org/10.1101/gad.286404.

Saraste, M., Sibbald, P.R., and Wittinghofer, A. (1990). The P-loop--a common motif in ATP- and GTP-binding proteins. Trends in biochemical sciences *15*, 430-434. https://doi.org/10.1016/0968-0004(90)90281-f.

Schröder, M., Bullock, A.N., Fedorov, O., Bracher, F., Chaikuad, A., and Knapp, S. (2020). DFG-1 Residue Controls Inhibitor Binding Mode and Affinity, Providing a Basis for Rational Design of Kinase Inhibitor Selectivity. Journal of medicinal chemistry *63*, 10224-10234. https://doi.org/10.1021/acs.jmedchem.0c00898.

Schrödinger, L., and DeLano, W. (2020). PyMOL.

Sen, S., Jumaa, H., and Webster, N.J.G. (2013). Splicing factor SRSF3 is crucial for hepatocyte differentiation and metabolic function. Nature communications *4*, 1336. https://doi.org/10.1038/ncomms2342.

Shatkin, A.J. (1976). Capping of eucaryotic mRNAs. Cell *9*, 645-653. https://doi.org/10.1016/0092-8674(76)90128-8.

Shen, H., Kan, J.L.C., and Green, M.R. (2004). Arginine-serine-rich domains bound at splicing enhancers contact the branchpoint to promote prespliceosome assembly. Molecular cell *13*, 367-376. https://doi.org/10.1016/s1097-2765(04)00025-5.

Singh, G., Kucukural, A., Cenik, C., Leszyk, J.D., Shaffer, S.A., Weng, Z., and Moore, M.J. (2012). The cellular EJC interactome reveals higher-order mRNP structure and an EJC-SR protein nexus. Cell *151*, 750-764. https://doi.org/10.1016/j.cell.2012.10.007.

Sinha, R., Allemand, E., Zhang, Z., Karni, R., Myers, M.P., and Krainer, A.R. (2010). Arginine methylation controls the subcellular localization and functions of the oncoprotein splicing factor SF2/ASF. Molecular and cellular biology *30*, 2762-2774. https://doi.org/10.1128/MCB.01270-09.

Song, M., Pang, L., Zhang, M., Qu, Y., Laster, K.V., and Dong, Z. (2023). Cdc2-like kinases: structure, biological function, and therapeutic targets for diseases. Signal transduction and targeted therapy *8*, 148. https://doi.org/10.1038/s41392-023-01409-4.

Spartz, A.K., Lee, S.H., Wenger, J.P., Gonzalez, N., Itoh, H., Inzé, D., Peer, W.A., Murphy, A.S., Overvoorde, P.J., and Gray, W.M. (2012). The SAUR19 subfamily of SMALL AUXIN UP RNA genes promote cell expansion. The Plant journal : for cell and molecular biology *70*, 978-990. https://doi.org/10.1111/j.1365-313X.2012.04946.x.

Spartz, A.K., Ren, H., Park, M.Y., Grandt, K.N., Lee, S.H., Murphy, A.S., Sussman, M.R., Overvoorde, P.J., and Gray, W.M. (2014). SAUR Inhibition of PP2C-D Phosphatases Activates Plasma Membrane H+-ATPases to Promote Cell Expansion in Arabidopsis. The Plant Cell *26*, 2129-2142. https://doi.org/10.1105/tpc.114.126037.

Stark, M.R., Dunn, E.A., Dunn, W.S.C., Grisdale, C.J., Daniele, A.R., Halstead, M.R.G., Fast, N.M., and Rader, S.D. (2015). Dramatically reduced spliceosome in Cyanidioschyzon merolae. Proceedings of the National Academy of Sciences of the United States of America *112*, E1191-200. https://doi.org/10.1073/pnas.1416879112.

Stavang, J.A., Gallego-Bartolomé, J., Gómez, M.D., Yoshida, S., Asami, T., Olsen, J.E., García-Martínez, J.L., Alabadí, D., and Blázquez, M.A. (2009). Hormonal regulation of temperature-induced growth in Arabidopsis. The Plant journal : for cell and molecular biology *60*, 589-601. https://doi.org/10.1111/j.1365-313X.2009.03983.x.

Stickeler, E., Kittrell, F., Medina, D., and Berget, S.M. (1999). Stage-specific changes in SR splicing factors and alternative splicing in mammary tumorigenesis. Oncogene *18*, 3574-3582. https://doi.org/10.1038/sj.onc.1202671.

Straub, K., and Merkl, R. (2019). Ancestral Sequence Reconstruction as a Tool for the Elucidation of a Stepwise Evolutionary Adaptation. Methods in molecular biology (Clifton, N.J.) *1851*, 171-182. https://doi.org/10.1007/978-1-4939-8736-8_9.

Sun, J., Qi, L., Li, Y., Chu, J., and Li, C. (2012). PIF4-mediated activation of YUCCA8 expression integrates temperature into the auxin pathway in regulating arabidopsis hypocotyl growth. PLOS Genetics *8*, e1002594. https://doi.org/10.1371/journal.pgen.1002594.

Takahashi, S., Okubo, R., Kanesaki, Y., Zhou, B., Takaya, K., Watanabe, S., Tanaka, K., and Imamura, S. (2021). Identification of Transcription Factors and the Regulatory Genes Involved in Triacylglycerol Accumulation in the Unicellular Red Alga Cyanidioschyzon merolae. Plants (Basel, Switzerland) *10*. https://doi.org/10.3390/plants10050971.

Takemura, T., Imamura, S., Kobayashi, Y., and Tanaka, K. (2018). Construction of a Selectable Marker Recycling System and the Use in Epitope Tagging of Multiple Nuclear Genes in the Unicellular Red Alga Cyanidioschyzon merolae. Plant & cell physiology *59*, 2308-2316. https://doi.org/10.1093/pcp/pcy156.

Tang, Y., Horikawa, I., Ajiro, M., Robles, A.I., Fujita, K., Mondal, A.M., Stauffer, J.K., Zheng, Z.-M., and Harris, C.C. (2013). Downregulation of splicing factor SRSF3 induces p53β, an alternatively spliced isoform of p53 that promotes cellular senescence. Oncogene *32*, 2792-2798. https://doi.org/10.1038/onc.2012.288.

Tazi, J., Kornstädt, U., Rossi, F., Jeanteur, P., Cathala, G., Brunel, C., and Lührmann, R. (1993). Thiophosphorylation of U1-70K protein inhibits pre-mRNA splicing. Nature *363*, 283-286. https://doi.org/10.1038/363283a0.

Toledo-Ortiz, G., Johansson, H., Lee, K.P., Bou-Torrent, J., Stewart, K., Steel, G., Rodríguez-Concepción, M., and Halliday, K.J. (2014). The HY5-PIF regulatory module coordinates light and temperature control of photosynthetic gene transcription. PLOS Genetics *10*, e1004416. https://doi.org/10.1371/journal.pgen.1004416.

Ule, J., and Blencowe, B.J. (2019). Alternative Splicing Regulatory Networks: Functions, Mechanisms, and Evolution. Molecular cell *76*, 329-345. https://doi.org/10.1016/j.molcel.2019.09.017.

Ule, J., Stefani, G., Mele, A., Ruggiu, M., Wang, X., Taneri, B., Gaasterland, T., Blencowe, B.J., and Darnell, R.B. (2006). An RNA map predicting Nova-dependent splicing regulation. Nature *444*, 580-586. https://doi.org/10.1038/nature05304.

Uzor, S., Porazinski, S.R., Li, L., Clark, B., Ajiro, M., Iida, K., Hagiwara, M., Alqasem, A.A., Perks, C.M., and Wilson, I.D., et al. (2021). CDC2-like (CLK) protein kinase inhibition as a novel targeted therapeutic strategy in prostate cancer. Scientific reports *11*, 7963. https://doi.org/10.1038/s41598-021-86908-6.

Valenzuela, N., Literman, R., Neuwald, J.L., Mizoguchi, B., Iverson, J.B., Riley, J.L., and Litzgus, J.D. (2019). Extreme thermal fluctuations from climate change unexpectedly accelerate demographic collapse of vertebrates with temperature-dependent sex determination. Scientific reports *9*, 4254. https://doi.org/10.1038/s41598-019-40597-4.

van Zanten, M., Pons, T.L., Janssen, J.A.M., Voesenek, L.A.C.J., and Peeters, A.J.M. (2010). On the Relevance and Control of Leaf Angle. Critical Reviews in Plant Sciences *29*, 300-316. https://doi.org/10.1080/07352689.2010.502086.

Varadi, M., Anyango, S., Deshpande, M., Nair, S., Natassia, C., Yordanova, G., Yuan, D., Stroe, O., Wood, G., and Laydon, A., et al. (2022). AlphaFold Protein Structure Database: massively expanding the structural coverage of protein-sequence space with high-accuracy models. Nucleic acids research *50*, D439-D444. https://doi.org/10.1093/nar/gkab1061.

Varjosalo, M., Keskitalo, S., van Drogen, A., Nurkkala, H., Vichalkovski, A., Aebersold, R., and Gstaiger, M. (2013). The protein interaction landscape of the human CMGC kinase group. Cell reports *3*, 1306-1320. https://doi.org/10.1016/j.celrep.2013.03.027.

Velazquez-Dones, A., Hagopian, J.C., Ma, C.-T., Zhong, X.-Y., Zhou, H., Ghosh, G., Fu, X.-D., and Adams, J.A. (2005). Mass spectrometric and kinetic analysis of ASF/SF2 phosphorylation by SRPK1 and Clk/Sty. The Journal of biological chemistry *280*, 41761-41768. https://doi.org/10.1074/jbc.M504156200.

Vile, D., Pervent, M., Belluau, M., Vasseur, F., Bresson, J., Muller, B., Granier, C., and Simonneau, T. (2012). Arabidopsis growth under prolonged high temperature and water deficit: independent or interactive effects? Plant, cell & environment *35*, 702-718. https://doi.org/10.1111/j.1365-3040.2011.02445.x.

Wahl, M.C., Will, C.L., and Lührmann, R. (2009). The spliceosome: design principles of a dynamic RNP machine. Cell *136*, 701-718. https://doi.org/10.1016/j.cell.2009.02.009.

Wang, E.T., Sandberg, R., Luo, S., Khrebtukova, I., Zhang, L., Mayr, C., Kingsmore, S.F., Schroth, G.P., and Burge, C.B. (2008). Alternative isoform regulation in human tissue transcriptomes. Nature *456*, 470-476. https://doi.org/10.1038/nature07509.

Wang, H.Y., Xu, X., Ding, J.H., Bermingham, J.R., and Fu, X.D. (2001). SC35 plays a role in T cell development and alternative splicing of CD45. Molecular cell *7*, 331-342. https://doi.org/10.1016/s1097-2765(01)00181-2.

Wang, Z., Kayikci, M., Briese, M., Zarnack, K., Luscombe, N.M., Rot, G., Zupan, B., Curk, T., and Ule, J. (2010). iCLIP predicts the dual splicing effects of TIA-RNA interactions. PLoS biology *8*, e1000530. https://doi.org/10.1371/journal.pbio.1000530.

Watanabe, S., Sato, J., Imamura, S., Ohnuma, M., Ohoba, Y., Chibazakura, T., Tanaka, K., and Yoshikawa, H. (2014). Stable expression of a GFP-reporter gene in the red alga Cyanidioschyzon merolae. Bioscience, biotechnology, and biochemistry *78*, 175-177. https://doi.org/10.1080/09168451.2014.877823.

Waterhouse, A.M., Procter, J.B., Martin, D.M.A., Clamp, M., and Barton, G.J. (2009). Jalview Version 2--a multiple sequence alignment editor and analysis workbench. Bioinformatics (Oxford, England) *25*, 1189-1191. https://doi.org/10.1093/bioinformatics/btp033.

Wilkinson-White, L.E., and Easterbrook-Smith, S.B. (2008). A dye-binding assay for measurement of the binding of Cu(II) to proteins. Journal of inorganic biochemistry *102*, 1831-1838. https://doi.org/10.1016/j.jinorgbio.2008.06.008.

Williams, C.J., Headd, J.J., Moriarty, N.W., Prisant, M.G., Videau, L.L., Deis, L.N., Verma, V., Keedy, D.A., Hintze, B.J., and Chen, V.B., et al. (2018). MolProbity: More and better reference data for improved all-atom structure validation. Protein science : a publication of the Protein Society *27*, 293-315. https://doi.org/10.1002/pro.3330.

Wit, M. de, Lorrain, S., and Fankhauser, C. (2014). Auxin-mediated plant architectural changes in response to shade and high temperature. Physiologia plantarum *151*, 13-24. https://doi.org/10.1111/ppl.12099.

Wong, D.K., Grisdale, C.J., Slat, V.A., Rader, S.D., and Fast, N.M. (2023). The evolution of pre-mRNA splicing and its machinery revealed by reduced extremophilic red algae. The Journal of eukaryotic microbiology *70*, e12927. https://doi.org/10.1111/jeu.12927.

Wong, R., Balachandran, A., Mao, A.Y., Dobson, W., Gray-Owen, S., and Cochrane, A. (2011). Differential effect of CLK SR Kinases on HIV-1 gene expression: potential novel targets for therapy. Retrovirology *8*, 47. https://doi.org/10.1186/1742-4690-8-47.

Wong, R.W., Balachandran, A., Ostrowski, M.A., and Cochrane, A. (2013). Digoxin suppresses HIV-1 replication by altering viral RNA processing. PLoS pathogens *9*, e1003241. https://doi.org/10.1371/journal.ppat.1003241.

Woodward, A.W., and Bartel, B. (2018). Biology in Bloom: A Primer on the Arabidopsis thaliana Model System. Genetics *208*, 1337-1349. https://doi.org/10.1534/genetics.118.300755.

Wu, J.Y., and Maniatis, T. (1993). Specific interactions between proteins implicated in splice site selection and regulated alternative splicing. Cell *75*, 1061-1070. https://doi.org/10.1016/0092-8674(93)90316-I.

www.snapgene.com. SnapGene Viewer 7.1.1 (www.snapgene.com).

Xiao, S.H., and Manley, J.L. (1997). Phosphorylation of the ASF/SF2 RS domain affects both protein-protein and protein-RNA interactions and is necessary for splicing. Genes & development *11*, 334-344. https://doi.org/10.1101/gad.11.3.334.

Xu, Z., and Weiss, A. (2002). Negative regulation of CD45 by differential homodimerization of the alternatively spliced isoforms. Nature immunology *3*, 764-771. https://doi.org/10.1038/ni822.

Yamasaki, H., Hayashi, M., Fukazawa, M., Kobayashi, Y., and Shikanai, T. (2009). SQUAMOSA Promoter Binding Protein-Like7 Is a Central Regulator for Copper Homeostasis in Arabidopsis. The Plant Cell *21*, 347-361. https://doi.org/10.1105/tpc.108.060137.

Yang, W., and Li, Q.-Z. (2008). One parameter to describe the mechanism of splice sites competition. Biochemical and biophysical research communications *368*, 379-381. https://doi.org/10.1016/j.bbrc.2008.01.089.

Ye, Y., and Godzik, A. (2003). Flexible structure alignment by chaining aligned fragment pairs allowing twists. Bioinformatics (Oxford, England) *19 Suppl 2*, ii246-55. https://doi.org/10.1093/bioinformatics/btg1086.

Yeo, G., and Burge, C.B. (2004). Maximum entropy modeling of short sequence motifs with applications to RNA splicing signals. Journal of computational biology : a journal of computational molecular cell biology *11*, 377-394. https://doi.org/10.1089/1066527041410418.

Yoon, H.S., Hackett, J.D., Ciniglia, C., Pinto, G., and Bhattacharya, D. (2004). A molecular timeline for the origin of photosynthetic eukaryotes. Molecular biology and evolution *21*, 809-818. https://doi.org/10.1093/molbev/msh075.

Yoon, H.S., Müller, K.M., Sheath, R.G., Ott, F.D., and Bhattacharya, D. (2006). DEFINING THE MAJOR LINEAGES OF RED ALGAE (RHODOPHYTA) 1. Journal of Phycology *42*, 482-492. https://doi.org/10.1111/j.1529-8817.2006.00210.x.

Yoshida, K., Sanada, M., Shiraishi, Y., Nowak, D., Nagata, Y., Yamamoto, R., Sato, Y., Sato-Otsubo, A., Kon, A., and Nagasaki, M., et al. (2011). Frequent pathway mutations of splicing machinery in myelodysplasia. Nature *478*, 64-69. https://doi.org/10.1038/nature10496.

Yun, B., Farkas, R., Lee, K., and Rabinow, L. (1994). The Doa locus encodes a member of a new protein kinase family and is essential for eye and embryonic development in Drosophila melanogaster. Genes & development *8*, 1160-1173. https://doi.org/10.1101/gad.8.10.1160.

Yun, C.Y., Velazquez-Dones, A.L., Lyman, S.K., and Fu, X.-D. (2003). Phosphorylation-dependent and -independent nuclear import of RS domain-containing splicing factors and regulators. The Journal of biological chemistry *278*, 18050-18055. https://doi.org/10.1074/jbc.M211714200.

Zahler, A.M., Lane, W.S., Stolk, J.A., and Roth, M.B. (1992). SR proteins: a conserved family of pre-mRNA splicing factors. Genes & development *6*, 837-847. https://doi.org/10.1101/gad.6.5.837.

Zhang, X., Chen, M.H., Wu, X., Kodani, A., Fan, J., Doan, R., Ozawa, M., Ma, J., Yoshida, N., and Reiter, J.F., et al. (2016). Cell-Type-Specific Alternative Splicing Governs Cell Fate in the Developing Cerebral Cortex. Cell *166*, 1147-1162.e15. https://doi.org/10.1016/j.cell.2016.07.025.

Zhang, Z., and Krainer, A.R. (2004). Involvement of SR proteins in mRNA surveillance. Molecular cell *16*, 597-607. https://doi.org/10.1016/j.molcel.2004.10.031.

Zhou, Z., and Fu, X.-D. (2013). Regulation of splicing by SR proteins and SR protein-specific kinases. Chromosoma *122*, 191-207. https://doi.org/10.1007/s00412-013-0407-z.

Zhou, Z., Qiu, J., Liu, W., Zhou, Y., Plocinik, R.M., Li, H., Hu, Q., Ghosh, G., Adams, J.A., and Rosenfeld, M.G., et al. (2012). The Akt-SRPK-SR axis constitutes a major pathway in transducing EGF signaling to regulate alternative splicing in the nucleus. Molecular cell *47*, 422-433. https://doi.org/10.1016/j.molcel.2012.05.014.

Zhu, J., Mayeda, A., and Krainer, A.R. (2001). Exon identity established through differential antagonism between exonic splicing silencer-bound hnRNP A1 and enhancer-bound SR proteins. Molecular cell *8*, 1351-1361. https://doi.org/10.1016/s1097-2765(01)00409-9.

Contributions

The following experiments were done in part or entirely by other researchers. Dr. Tom Haltenhof performed initial characterization of CmLIK-KD WT (Figure 1-3) and cloned the CmLIK-KD WT/D690S/hairpin, mCLK4-KD, AmCLK4-KD and TsCLK1-KD constructs which were used for expression in this thesis, as well as the CmSC35 construct which was the basis for the re-cloning we performed. Ana Kotte expressed and purified the CmLIK-KD WT protein that was used for the assays in this thesis. Paul Wulf expressed and purified the GST-RS synthetic substrate that was used for the assays in this thesis. Miriam Strauch cloned the AtAFC constructs which were used as templates for re-cloning and mutation in this thesis. Initial *in vitro* kinase assays for AtAFCs (Figure 1-4) were performed by Miriam Strauch and Paul Wulf. Dr. Rainer Merkl and Dr. Kristina Straub (AG Merkl, University of Regensburg) reconstructed ancestral CLK sequences. Dr. Daniel Maag (AG Maag, University of Würzburg) generated *A. thaliana afc1/2/3* triple knock-out plants and supplied extracted RNA from these plants for gene expression analysis. Dr. Bernhard Loll (AG Wahl, FU Berlin) performed all X-ray diffraction experiments and diffraction data processing and assisted with analysis of crystallographic data and model refinement. Dr. Benno Kuropka (BioSupraMol, FU Berlin) supervised all MS experiments, performed the LC-ESI-MS/MS measurements and assisted with data analysis.

Abbreviations

°C	degrees Celsius
Å	Ångström
ACN	acetonitrile
A. thaliana	*Arabidopsis thaliana*
AMPPNP	adenylyl-imidodiphosphate
AtAFC	A. thaliana AFC
ATP	adenosine tri-phosphate
C. merolae	*Cyanidioschyzon merolae*
CD	circular dichroism
CDK	cyclin-dependent kinase
cDNA	complementary DNA
CLK	Cdc2-like kinase
CMGC	CDK, MAPK, GSK3, CLK
CmLIK	*C. merolae* LIK
CV	column volume
DESY	Deutsches Elektronen-Synchrotron
DTT	dithiothreitol
DYRK	dual-specificity tyrosine-regulated kinases
E. coli	*Escherichia coli*
EDTA	ethylenediaminetetraacetic acid
EGF	epidermal growth factor
EGFR	EGF receptor
ESE	exonic splicing enhancer
ESS	exonic splicing silencer
f.l.	full-length
FA	formic acid
FT	flow-through
FU Berlin	Freie Universität Berlin
GSK3	glycogen synthase kinase
GST	Glutathione S-transferase
hCLK1	human CLK1
HEPES	4-(2-hydroxyethyl)-1-piperazineethanesulfonic acid
hnRNP	heterogenous nuclear ribonucleoproteins
HZB	Helmholtz-Zentrum Berlin
IAA	indole-3-acetic acid
IPTG	isopropyl β-d-1-thiogalactopyranoside
IVKA	in vitro kinase assay
kb	kilobases
KD	kinase domain
kDa	kilo Dalton
KO	knock-out
LC-ESI-MS	liquid chromatography electron spray ionization MS
LC-ESI-MS/MS	LC-ESI tandem MS

LFQ	label free quantification
LIK	LAMMER-like dual-specificity kinase
MALDI-ISD MS	matrix-assisted laser desorption/ionization combined with in-source decay MS
MAPK	mitogen-activated protein kinase
Mbp	Mega base pairs
MBP	maltose binding protein
mCLK4	mouse CLK4
MES	2-(N-morpholino)ethanesulfonic acid
mRNA	messenger RNA
MS	mass spectrometry
MSA	multiple sequence alignment
MWCO	molecular weight cut-off
NLS	nuclear localization sequence
NMD	nonsense-mediated decay
nt	nucleotides
OD_{600}	optical density at 600 nm
ON	overnight
PCR	polymerase chain reaction
PEG	poly ethylene glycol
PI3K	phosphatidylinositol 3-kinase
PIF4	phytochrome-interacting factor 4
PKCβII	protein kinase C βII
Pol II	RNA polymerase II
pre-mRNA	precursor mRNA
PTM	post translational modification
qPCR	quantitative PCR
r.m.s.d.	root-mean-square deviation
RBD	RNA binding domain
RS domain	arginine-serine rich domain
RT	room temperature
SAUR	small auxin up RNA
SDS	sodium dodecyl sulfate
SDS-PAGE	SDS-polyacrylamide gel electrophoresis
SEC	size exclusion chromatography
snRNP	small nuclear ribonucleoprotein particle
SRPK	SR-protein specific kinase
SRSF	serine-arginine rich splicing factor
TFA	trifluoroacetic acid
TKO	triple knock-out
T_m	melting temperature
Tris	tris(hydroxymethyl)aminomethane
Trx	thioredoxin
TSA	thermal shift assay
TSD	temperature dependent sex determination
WT	wildtype

Table of Figures